AD-A046 055 NORTH CAROLINA STATE UNIV RALEIGH ENGINEERING DESIGN--ETC F/G 13/7
EFFECT OF INLET DISTORTION ON PERFORMANCE OF A COMPRESSOR STAGE--ETC(U)
APR 77 L W HARDIN, W C GRIFFITH, J N PERKINS F44620-76-C-0055

UNCLASSIFIED NCSU/EDC-77-1 AFOSR-TR-77-1238 NL

1 OF 2
ADA
046055

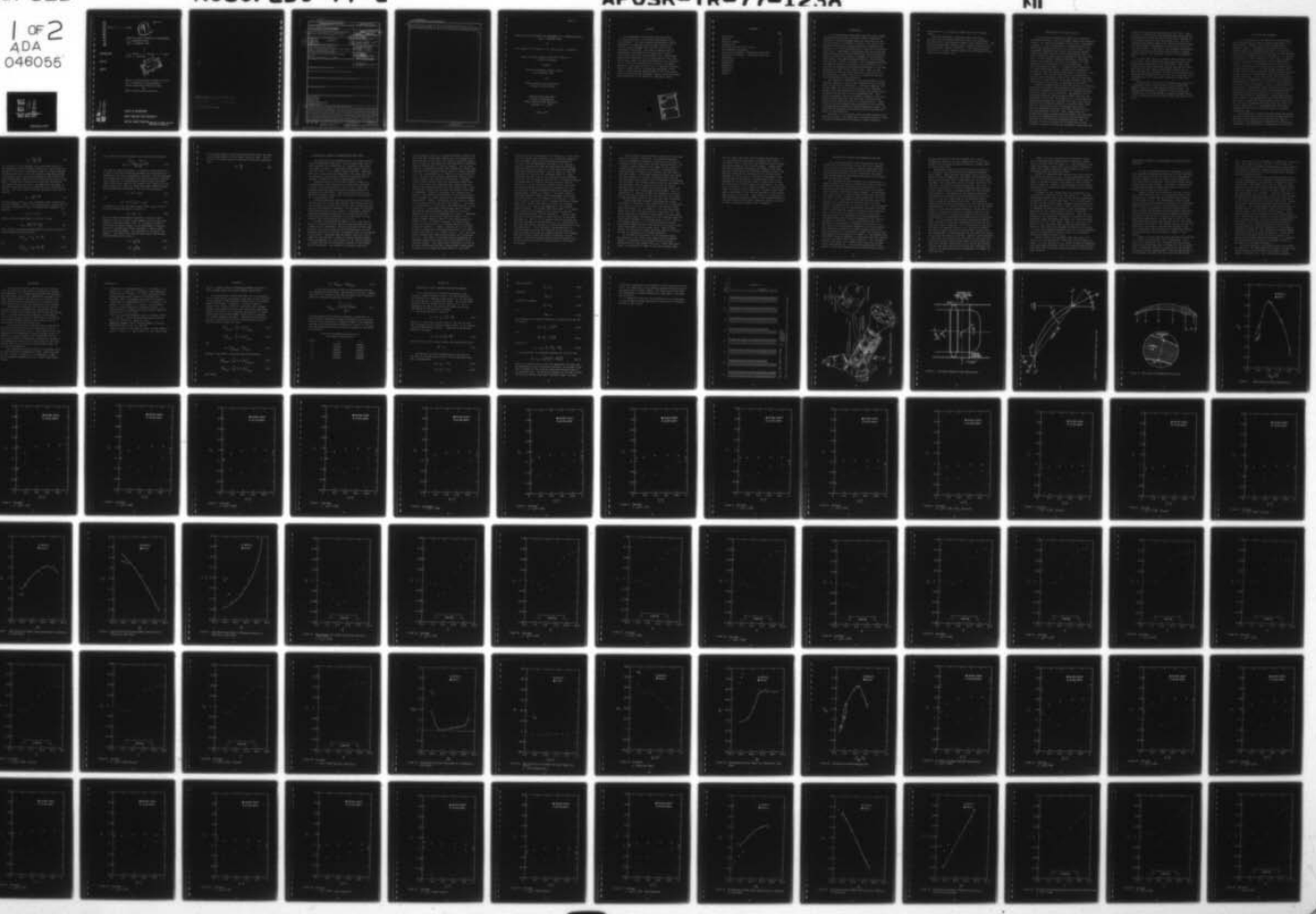

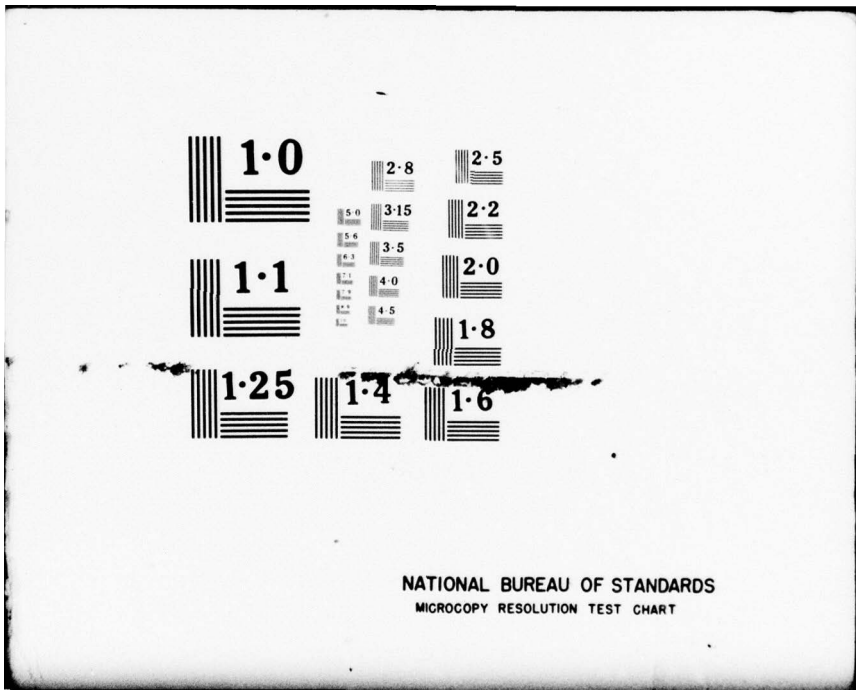
1·0
1·1
1·25
1·4
1·6
1·8
2·0
2·2
2·5
2·8
3·15
3·5
4·0
4·5
5·0
5·6
NATIONAL BUREAU OF STANDARDS
MICROCOPY RESOLUTION TEST CHART

AFOSR-TR- 77 - 1238

EDC-77-1

(9)

EFFECT OF INLET DISTORTION ON PERFORMANCE OF A COMPRESSOR STAGE: PART I, PNEUMATIC DATA

by

L. W. Hardin, J. N. Perkins, F. O. Carta and W. C. Griffith

ENGINEERING

DESIGN

CENTER

Report on AFOSR Contract F44620-76-C-0055
for a cooperative program between
United Technologies Research Center
and
North Carolina State University

SCHOOL OF ENGINEERING

NORTH CAROLINA STATE UNIVERSITY

RALEIGH, NORTH CAROLINA

AIR FORCE OFFICE OF SCIENTIFIC RESEARCH (AFSC)
NOTICE OF TRANSMITTAL TO DDC
This technical report has been reviewed and is approved for public release IAW AFR 190-12 (7b).
Distribution is unlimited.
A. D. BLOSE
Technical Information Officer

UNCLASSIFIED

SECURITY CLASSIFICATION OF THIS PAGE (When Data Entered)

REPORT DOCUMENTATION PAGE

READ INSTRUCTIONS BEFORE COMPLETING FORM

1. REPORT NUMBER (18) AFOSR-TR-77-1238 (19)
2. GOVT ACCESSION NO.
3. RECIPIENT'S CATALOG NUMBER

4. TITLE (and Subtitle) (6)
EFFECT OF INLET DISTORTION ON PERFORMANCE OF A COMPRESSOR STAGE: PART I. PNEUMATIC DATA

5. TYPE OF REPORT & PERIOD COVERED (9) Rept. for
INTERIM
Jul 1976 - Apr 1977,

6. PERFORMING ORG. REPORT NUMBER (14)
NCSU/EDC-77-1

7. AUTHOR(s) (10)
L. W. HARDIN, F. O. CARTA
W. C. GRIFFITH,
J. N. PERKINS

8. CONTRACT OR GRANT NUMBER(s) (15)
F44620-76-C-0055 New

9. PERFORMING ORGANIZATION NAME AND ADDRESS
NORTH CAROLINA STATE UNIVERSITY
SCHOOL OF ENGINEERING, ENGINEERING DESIGN CENTER
RALEIGH, NORTH CAROLINE, 27607

10. PROGRAM ELEMENT, PROJECT, TASK AREA & WORK UNIT NUMBERS (16) (17)
2307A4 A4
61102F

11. CONTROLLING OFFICE NAME AND ADDRESS
AIR FORCE OFFICE OF SCIENTIFIC RESEARCH/NA
BLDG 410
BOLLING AIR FORCE BASE, D C 20332

12. REPORT DATE (11)
April 1977

13. NUMBER OF PAGES
~~143~~ (12) 115p.

14. MONITORING AGENCY NAME & ADDRESS (if different from Controlling Office)

15. SECURITY CLASS. (of this report)
UNCLASSIFIED

15a. DECLASSIFICATION/DOWNGRADING SCHEDULE

16. DISTRIBUTION STATEMENT (of this Report)

Approved for public release; distribution unlimited.

17. DISTRIBUTION STATEMENT (of the abstract entered in Block 20, if different from Report)

18. SUPPLEMENTARY NOTES

19. KEY WORDS (Continue on reverse side if necessary and identify by block number)
DYNAMIC STALL
DISTORTED FLOW
UNSTEADY FLOW
UNSTEADY BOUNDARY LAYER
TURBOCOMPRESSOR

20. ABSTRACT (Continue on reverse side if necessary and identify by block number)

An experimental investigation into the effects of inlet distortion on an isolated turbomachine rotor was conducted. The data obtained from pneumatic instrumentation was analyzed to gain insight into both the overall stage performance and the flow field of an individual rotor blade. The results indicate that the unsteadiness introduced by the distortion increases blade normal force and stage pressure rise. While undergoing inlet distortion, it was found that the rotor does not locally follow the undistorted pressure loss characteristic. Entry into rotating stall results in an abrupt decrease in the stage pressure rise. A definite

next page

DD FORM 1 JAN 73 1473 EDITION OF 1 NOV 65 IS OBSOLETE

UNCLASSIFIED

SECURITY CLASSIFICATION OF THIS PAGE (When Data Entered)

409 679

hysteresis loop is evident for the stalling and unstalling of the rotor. A more complete understanding of the inlet distortion and rotating stall phenomena requires unsteady measurements which will be discussed in a subsequent report.

EDC-77-1

EFFECT OF INLET DISTORTION ON PERFORMANCE OF A COMPRESSOR STAGE: PART I, PNEUMATIC DATA

by

*L.W. Hardin, *J.N. Perkins, F.O. Carta and *W.C. Griffith

Report on AFOSR Contract F44620-76-C-0055 for a cooperative program

between

United Technologies Research Center
East Hartford, Conn.

and

*North Carolina State University
Raleigh, North Carolina

Engineering Design Center
School of Engineering
North Carolina State University
Raleigh, N. C. 27607

April, 1977

ABSTRACT

An experimental investigation into the effects of inlet distortion on an isolated turbomachine rotor was conducted. The data obtained from pneumatic instrumentation was analyzed to gain insight into both the overall stage performance and the flow field of an individual rotor blade. The results indicate that the unsteadiness introduced by the distortion increases blade normal force and stage pressure rise. While undergoing inlet distortion, it was found that the rotor does not locally follow the undistorted pressure loss characteristic. Entry into rotating stall results in an abrupt decrease in the stage pressure rise. A definite hysteresis loop is evident for the stalling and unstalling of the rotor. A more complete understanding of the inlet distortion and rotating stall phenomena requires unsteady measurements which will be discussed in a subsequent report.

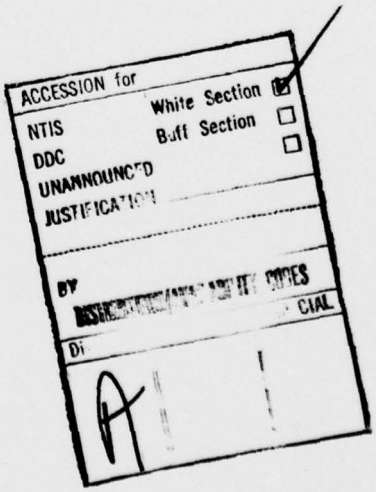

CONTENTS

INTRODUCTION

In 1975 the United Technologies Research Center (UTRC) and North Carolina State University (NCSU) established a cooperative research program under the sponsorship of the Air Force Office of Scientific Research. The goal of this program was to provide improved predictive techniques for design of axial flow turbocompressors subjected to distorted inlet flows. Experimental measurements and data processing would be carried out with the UTRC Large Scale Rotating Rig (LSRR) and associated computer equipment at East Hartford. Data analysis and computer-based theoretical flow modeling would be done at NCSU in Raleigh. The arrangement provided for graduate student participants from the university to take part in planning and conducting experiments in the UTRC facilities as part of their thesis work. While in East Hartford they would be supervised by Mr. Frank Carta, who was appointed an Adjunct Professor of Mechanical and Aerospace Engineering by the university.

The theoretical modelling of the flow through a single rotating compressor stage and the experimental plan for the LSRR are described in Reference 1. From the summer of 1975 to the summer of 1976 Mr. Larry Hardin, Ph.D. candidate, worked in the UTRC laboratories to design and prepare instrumentation and take part in the experimental runs. Both static and dynamic data were recorded on magnetic tape for a baseline undistorted flow and then with a distorted flow produced by an upstream screen of varying porosity. Significant to the experimental plan was provision for extensive instrumentation on board the rotating compressor stage. The onset and disappearance of rotating stall was detected for a range of flow conditions.

The rotor is 5' in diameter with 28 blades having an 0.8 hub-to-tip ratio. The blades have a constant chord of 6" with a section at midspan of 8% thickness, series 65 profile

superimposed on a circular arc camber line with 50 degree camber.

Typical experimental conditions were; rotor speed 600 RPM, axial flow speed 100 ft/sec with a 20% sinusoidal distortion for a blade Reynolds number in the range of 0.5×10^6. Some preliminary data reduction done by hand was given in an interim progress report, Reference 2. This report presents the results of a more complete computer-aided reduction of the steady state pneumatic data.

DESCRIPTION OF THE TEST FACILITY

The Large Scale Rotating Rig (LSRR) was designed for experimental studies of the flow within turbine and compressor blading. The overall arrangement of this rig is illustrated in figure 1. The rotating stage is cantilevered from two downstream bearings and driven by a hydraulic motor. This arrangement eliminates the need for any upstream support struts that might interfere with the approaching flow and permits control of rotor speed independent of the axial flow rate. For the present program no upstream or downstream stators were employed. The rotor tip diameter is 5 feet, the hub to tip ratio being 0.8 in this experiment. Air enters the tunnel through a 12' diameter inlet fitted with a 6" thick honeycomb section. Further flow smoothing is provided by three fine-mesh screens after a transition to the 5' diameter. For the distorted inlet flow experiments a special screen designed to yield a 20%, once-per-revolution variation in axial velocity was placed upstream of the rotor. Construction of this screen is described in Reference 1.

Normal instrumentation for the LSRR consists of stationary and relative reference frame pneumatic probes and taps connected to scanivalves to measure the time averaged pressures at various points in the flow field. Measurements in the stationary reference frame include pressures upstream and downstream of the rotor, flow angles, etc. At the time this experimental program was conducted, the LSRR casing instrumentation was configured primarily for uniform inlet flows. That is, casing static taps for determining the axial pressure variation across the rotor were available at only one circumferential location. Also, wedge probes for measuring upstream and downstream flow angles were available at only one circumferential location which was different from that for the previously mentioned pressure taps. At the time, it was not possible to instrument more circumferential locations nor would the scanivalve system have been

capable of accepting the additional pressure lines. Thus, it must be realized that the previously mentioned quanities represent local values for the distorted flow condition and not averaged values for the entire rotor face. The only pneumatic measurements made in the relative reference frame are static pressure measurements on the surface of one of the rotor blades. In addition to the pneumatic measurements, a great deal of data were taken using unsteady instrumentation; however, this report will cover only the penumatic data.

The tests were run at a constant corrected wheel speed of 600 rpm. Axial velocity was controlled by means of a vortex valve downstream of the test section. Tests were conducted over axial velocities ranging from those at which the rotor was very lightly loaded down to velocities at which rotating stall occurred. Two inlet flow conditions were investigated, uniform inlet flow and a flow which had a 20% amplitude, one-cycle sinusoidal variation in inlet axial velocity.

Transient data, which will be presented and analyzed in a subsequent report, was recorded on two 14-channel FM magnetic tapes by the UTRC Analog Recording System. The dynamic instrumentation included hot films and pressure transducers in one blade passage, a movable triaxial probe in the rotating frame, and triaxial probes downstream of the rotor.

DATA REDUCTION PROCEDURE

As an introduction to the reduction of the pneumatic data obtained from the inlet distortion experiment, it is appropriate to comment on some of the limitations of pneumatic probes. A pneumatic probe measures the time-averaged value of a fluctuating pressure. The effects of these pressure fluctuations on the accuracy of data obtained by means of a pneumatic system is reported by J. C. Bennett in reference 3. The conclusions of this report as applied to the inlet distortion experiment may be summarized as follows: first, in a fluctuating velocity field the velocity calculated from the average static pressure and the average total pressure is not the average velocity; and second, the flow angle calculated from the average pressures on the surfaces of a wedge probe is not necessarily the average flow angle. One is thus faced with the problem of placing the instrumentation close enough to the source of the disturbance, in this case a rotor, to measure the flow field due to this disturbance, yet not so close that the local velocity fluctuations cause significant errors in the measurements. Whenever possible, the non-dimensionalized quantities presented were defined so as to minimize the errors which could be introduced by a fluctuating velocity field; however, the fluctuations associated with rotating stall are so severe that one must have serious doubts as to the validity of pneumatic data taken under this flow condition. Therefore, it is recommended that the results presented for the case of rotating stall be considered qualitative only.

The maximum axial velocity attained during the experiment was on the order of 100 ft/sec and the wheel speed was 600 rpm giving a tangential tip speed on the order of 150 ft/sec. Considering these relatively low values, the treatment of the flow field as incompressible is certainly

justified; therefore, a value of density based on static properties upstream of the rotor will be used throughout the flow field.

$$\rho = \frac{P_{s_1}}{R\, T_{s_1}} \tag{1}$$

The upstream static and total pressures are made sufficiently far upstream of the rotor that velocity fluctuations due to the rotor may be neglected and the flow may be assumed to be purely axial.

$$C_x = \sqrt{\frac{2\left(P_{t_1} - P_{s_1}\right)}{\rho}} \tag{2}$$

The rotor was run at a constant corrected wheel speed of 600 rpm. From this value, the actual wheel speed may be found by:

$$N_{act} = N_{corr} \sqrt{\frac{T_{s_1}}{T_{ref}}} \tag{3}$$

Where T_{ref} is 518.7°R. The tangential velocity, U, may be determined by:

$$U = \frac{N_{act}\ \pi\ D}{60\ \text{sec/min}} \tag{4}$$

The diameter, D, used in the data reduction was 4.5 ft which is the diameter at the blade midspan where the blade instrumentation was located. A pressure coefficient is defined by:

$$C_p = \frac{P - P_{s_1}}{\frac{1}{2}\ \rho\ U^2} \tag{5}$$

In particular, the rotor pressure rise coefficient, C_{p_r}, is defined by:

$$C_{p_r} = \frac{P_{s_2} - P_{s_1}}{\frac{1}{2} \rho U^2} \tag{6}$$

The variation of this pressure rise coefficient with C_x/U is considered to be the primary indication of the overall performance of the rotor. Stationary frame flow angles upstream and downstream of the rotor were measured using wedge probes. As previously noted, the angles measured by these probes are questionable under conditions of fluctuating flow velocity and angle. In addition to being used to show the variation of flow angle with the C_x/U ratio, the downstream flow angle is employed to determine the total pressure loss coefficient as follows. The total relative velocity upstream of the rotor is given by:

$$W_1 = \sqrt{C_x^2 + U^2} \tag{7}$$

The downstream velocity in the stationary frame is made up of an axial component, equal to the upstream axial velocity by the continuity requirement, and a circumferential component, C_{θ_2}, given by:

$$C_{\theta_2} = C_x \tan \theta_2 \tag{8}$$

Relative velocity downstream of the rotor is thus

$$W_2 = \sqrt{C_x^2 + (U - C_{\theta_2})^2} \tag{9}$$

Total pressure upstream and downstream of the rotor in the relative frame may be calculated as

$$\left(P_{t_1}\right)_{rel} = P_{s_1} + \frac{1}{2} \rho W_1^2 \tag{10}$$

and

$$\left(P_{t_2}\right)_{rel} = P_{s_2} + \frac{1}{2} \rho W_2^2 \tag{11}$$

The steady state total pressure loss coefficient defined by:

$$X_{ss} = \frac{\left(P_{t_2}\right)_{rel} - \left(P_{t_1}\right)_{rel}}{\frac{1}{2}\rho W_1^2} \tag{12}$$

may then be easily calculated. It should be noted that due to a lack of flow angle measuring equipment the flow angles were measured at only one circumferential station. For the distorted flow condition, the flow angles and loss coefficients represent local values for a circumferential location where the local axial velocity was equal to the average axial velocity for the entire rotor face. Relative frame flow angles (UTRC notation) both upstream and downstream of the rotor are defined by:

$$\beta_1 = \tan^{-1}\left(C_x/U\right) \tag{13}$$

and

$$\beta_2 = \tan^{-1}\left[C_x/(U - C_{\theta_2})\right] \tag{14}$$

respectively. Given the blade stagger angle, α_{CH}, of 55° it is easy to define an angle of attack as

$$\alpha_R = \alpha_{CH} - \beta_1 \tag{15}$$

The flow angle relationships are shown in figures 2 and 3. Pneumatic taps are located at the midspan of one of the rotor blades in a Gaussian array, (Ref. 4), as shown in figure 4. This array was chosen because of the high degree of accuracy possible in integrating surface pressures to obtain normal force and pitching moment. The procedure is outlined in Appendix A. The normal force and pitching moment coefficients thus determined are defined by:

$$C_N = \frac{N}{\frac{1}{2}\rho U^2} \tag{16}$$

$$C_M = \frac{M}{\frac{1}{2}\rho U^2} \tag{17}$$

this pitching moment coefficient being defined about the leading edge and positive in the normal (nose up) sense. The location of the blade center of pressure (CP) may be calculated from:

$$CP = \frac{C_M}{C_N} \quad . \tag{18}$$

DISCUSSION OF RESULTS FOR UNDISTORTED INLET FLOW

The discussion of the pneumatic data will begin with the case of undistorted inlet flow. First consider the plot of rotor pressure rise coefficient as a function of the ratio C_x/U shown in figure 5. Beginning at the highest value of C_x/U the rotor is in a lightly loaded condition. Traversing the curve in the direction indicated by the arrows the flow rate decreases and pressure coefficient increases until a maximum is reached at a C_x/U of approximately 0.77.

Continued decrease of the axial velocity results in a dropping off of the pressure rise coefficient culminated by entry into rotating stall at $C_x/U = 0.55$. Entry into rotating stall was characterized by an abrupt decrease in pressure rise coefficient. The axial velocity was not reduced any further at this point as the test rig was already at its operational limit.

Increasing the axial velocity resulted in an increase in the pressure rise coefficient; however, the pressure rise for a given value of C_x/U was lower for the case of rotating stall than for the unstalled condition. For the range of C_x/U over which rotating stall exists, there is a relatively constant difference between the pressure rise coefficient for the stalled and unstalled conditions at the same value of C_x/U. Recovery from stall occurred at $C_x/U = 0.62$.

In order to understand the details of the flow, the behavior of the pressure distribution along the midspan of the blading will be considered. Data are available for the same points as were used to generate the preceding plot of rotor pressure rise and the pressure distributions will be considered in that order. Beginning with the highest value of C_x/U in figure 6a, one observes a region of locally negative normal force contribution (i.e. the pressure on the suction surface is higher than that on the pressure surface) at the leading edge of the blade. This behavior is entirely normal for

highly cambered airfoils in cascade and merely reflects the fact that the leading edge tangent line is at negative incidence relative to the flow. The region of negative normal force shrinks as C_x/U decreases (corresponding to increasing angle of attack) until it finally vanishes. As the axial velocity is further decreased, the leading edge suction peak associated with isolated airfoils begins to appear although it is not so pronounced as it would be for an isolated airfoil. The entry into rotating stall brings about an interesting change in the pressure distributions. Although several of the pressure taps were inoperative during this part of the testing the remaining ones indicate that the suction peak which has built up on the leading edge is lost but that the loading over the rear two-thirds of the blade is unchanged. Figure 6n illustrates this behavior most clearly. The pressure distributions in the preceding plots were integrated to obtain normal force and pitching moment coefficients. Figure 7 illustrates the variation of normal force coefficient with the inlet flow angle β_1. The reader is cautioned that β_1 is defined in the UTRC notation so that increasing β_1 corresponds to decreasing angle of attack. The precise relation between these angles is given by equation 15 and is shown graphically in figure 3. Beginning at the extreme right side of figure the rotor is in a lightly loaded condition, that is, the relative angle of attack is low. As would be expected, the normal force coefficient increases as β_1 is reduced causing the blade loading to increase. A peak is attained at $\beta_1 = 45°$ after which the normal force coefficient decreases. At a sufficiently low value of β_1, in this case $\beta_1 = 28.6°$, the rotor enters rotating stall which persists until β_1 is increased to 32.0°. The reader is cautioned against attempting an immediate comparison of this curve to the behavior of an isolated airfoil. The normal force coefficient, as well as pressure coefficients and the pitching moment coefficients, are based on the tangential wheel speed, U. The total

relative velocity experienced by the blade, W_1, is the vector sum of U and the axial velocity, C_x, as given by equation 7. Since the wheel speed was held constant and changes in (or C_x/U) were accomplished by varying C_x, the relative velocity sensed by the blade decreased with decreasing β_1 while the velocity by which the coefficients were nondimensionalized remained constant. The net result is that the peak value of C_N occurs at a different value of β_1 than would have been the case if the coefficients were nondimensionalized by the relative velocity, W_1. In order to convert the coefficients as defined into ones based on relative velocity, as is the case with isolated airfoil data, these coefficients whould be multiplied by the quantity $\cos^2 \beta_1$. The variation of pitching moment coefficient (about the leading edge) is shown in figure 8. The trend toward increasingly negative values of pitching moment coefficient with increasing β_1 is attributable to two factors. First, as the value of β_1 (hence C_x/U) increases, the blade loading shifts aft. Second, increasing β_1 results in increased relative velocity; hence, the magnitude of the pitching moment increases. To separate these two trends it is convenient to observe the movement of the center of pressure as defined by equation 18 with varying β_1. Figure 9 shows that the center of pressure is rather far aft on the blade for high β_1. This is to be expected from the pressure distribution encountered at high values of β_1. Recall that in this case the leading edge gave a negative contribution to the net normal force. As β_1 decreases, corresponding to increasing angle of attack, the reduction of the region of negative normal force and the eventual growth of the leading edge suction peak causes the center of pressure to move forward. Entry into rotating stall with the resultant loss of the suction peak causes a rearward shift in the center of pressure.

The variation of casing pressure coefficient with axial position is shown in figure 10. As should be expected, there are important similarities between the pressure distribution on the rotor blades and the casing pressures. For a lightly loaded condition as in figure 10a the region of rapid increase in pressure coefficient is displaced aft. Referring back to figure 6a one observes that the blade is also aft-loaded. As the blade loading increases the region of rapid increase in pressure coefficient moves forward. The same behavior was observed for the pressure distributions on the blades. For example, compare figure 6j and figure 10j. One phenomenon which is apparent in all of the casing pressure plots is the region of decreasing pressure as the flow approaches the leading edge of the blading. This is explained by E. Grietzer of UTRC (see Appendix B) as being due to the velocity fluctuations caused by the flow fields of the individual blades as they pass the point in question.

Another important parameter describing the overall efficiency of the rotor is the steady state loss coefficient, X_{ss}, which is plotted as a function of the relative frame inlet flow angle, β_1, in figure 11. The rotor encounters heavy losses for flow angles above 50° and below 32°. The lower flow angles correspond to high angles of attach whereas the higher angles correspond to a flow condition where the blade may be thought of as working against itself. That is, the leading edge which is at locally negative incidence contributes negative normal force while the rear part of the blade contributes positive normal force. Both of these regions lie outside the normal operating range of the rotor but may be encountered in transient operation.

To conclude the discussion of the undistorted data the behavior of the various flow angles will be examined. Figure 12 illustrates the variation of the stationary entrance and exit flow angles with C_x/U. Recall that these angles are measured 0.5" ahead or the rotor leading edges

and 0.5" behind the rotor trailing edges respectively. It is significant that inception of rotating stall had no noticeable effect on the exit flow angle but caused a large and abrupt change in the inlet flow angle. Coupled with previous observations concerning the change in the blade pressure distributions at inception of rotating stall, this behavior would seem to indicate that the rotating stall phenomena for this rotor is primarily concentrated at the leading edge of the blading. Unsteady data which is not included in this report also tends to support this belief. The variation of relative frame exit flow angle, β_2, with inlet flow angle, β_1, is shown in figure 13. The exit flow angle of about 65° which results for a range of inlet flow angles corresponds to flow leaving parallel to the trailing edge tangent of the blade. Lower values of β_2 represent turning toward the suction surface of the blade which may be associated with trailing edge separation; however, there is no other indication to support this assumption.

DISCUSSION OF RESULTS FOR DISTORTED INLET FLOW

Since the significance of the various plots has been pointed out in the previous section, only brief comments will be made in this section to indicate significant deviations from the results obtained with uniform inlet flow. A more detailed discussion of the similarities and differences encountered with and without distortion will be undertaken in the next section.

The variation of rotor pressure rise coefficient as shown in figure 14 follows a trend quite similar to that for undistorted flow for the higher flow coefficients. As the rotor nears and finally enters the region of rotating stall, however, differences begin to appear. For distorted flow, the decrease in rotor pressure rise as the C_x/U ratio is reduced is not so severe as with uniform flow. In fact, for $C_x/U = 0.55$ (just before entry into rotating stall) the pressure rise coefficient for distorted flow is 0.595; whereas, for uniform flow it was only 0.532. This difference seems to indicate that the unsteadiness introduced into the flow by the distortion results in a gain in rotor effectiveness. The decrease in pressure rise due to entry into rotating stall is of approximately the same magnitude as with undistorted flow; however, performance in the stalled condition is different. For the undistorted case, the pressure rise coefficient in rotating stall appears to be the same as for the unstalled condition at the same value of C_x/U except for a relatively constant offset equal to the loss in pressure rise occasioned by entry into rotating stall. Such behavior is not apparent in figure 14. The pressure rise coefficient seems to approach its unstalled value more closely as C_x/U is increased after stall inception. Also, recovery seems to take place at a slightly lower value of C_x/U than in the undistorted case. One possible explanation of this effect is that the conditions in the region of high velocity

become such that the stall cell quenches as it passes through that region at a lower average value of C_x/U than would be the case when the axial velocity is uniform across the face of the rotor.

Proceeding to the plots of blade pressure coefficient as a function of chordwise position, further differences may be noted. Beginning with the highest value of C_x/U in figure 15a one is immediately aware that the distribution on the pressure surface shows a large jump very near the trailing edge. This jump did not exist in figure 6c which is the same value of C_x/U for the undistorted case. Also, the pressure coefficient at the most forward measuring station on the suction surface is somewhat higher for the distorted flow condition. The behavior at the leading edge may be attributed to the unsteady effects generated by the fluctuations of the local inlet angle as an individual blade passes through the distorted inlet flow. The anomalous behavior near the trailing edge does not have such an obvious interpretation. It persists, however, for all but the lowest values of C_x/U with one notable exception. Figure 15c represents a repeat point taken on a different day for essentially the same flow condition of figure 15b and shows no discontinuity in the pressure distribution near the trailing edge. As C_x/U decreases the pressure distributions behave quite similarly to those for undistorted flow with the two previously noted exceptions. It is interesting to note that the region of pressure reversal (i.e. the suction surface pressure is higher than that on the pressure surface) near the leading edge is larger and persists for much lower values of C_x/U when the flow is distorted. Finally, close inspection of the plots for distorted flow and those for the same C_x/U without distortion indicate that, while the differences between the pressure coefficients on the suction and pressure surfaces are quite similar for the two flow conditions, the value of the individual pressure coefficients is higher for distorted flow.

Figures 16 and 17 illustrate the variation of normal force coefficient and pitching moment coefficient, respectively, with the inlet flow angle β_1. The variation in the center of pressure location with β_1 is shown in figure 18. These three figures follow the same trends as do the corresponding plots for undistorted flow.

Figure 19 illustrates the pressure rise across the rotor for the various values of C_x/U. As with undistorted flow, there is a distinct correlation between the blade loading of figure 15 and the location of the region of rapid pressure rise in figure 19. Notably, the persistence of the pressure reversal on the leading edge tends to displace this pressure rise farther aft.

In figure 20, the steady state loss coefficient, X_{ss}, is plotted as a function of the inlet angle β_1. The most outstanding feature of this plot is that the loss coefficient is negative over a significant range. It is not physically possible for the rotor to have a negative total pressure loss so some explanation is in order. Recall that due to a lack of equipment to measure flow angles, these measurements were made only at one circumferential location at which the velocity was equal to the average velocity. Since the computation of X_{ss} (equations 7 through 12) involves use of the stationary frame downstream flow angle, the value thus determined can only be a local value. Thus it is only the local value of X_{ss} at the point where β_2 was measured which is negative. This means that somewhere on the rotor disc there is a region of relatively high loss and that by some mechanism energy is transported to the point where β_2 was measured causing the negative value of X_{ss}.

Figure 21 plots the stationary frame flow angles as a function of C_x/U and figure 22 plots the relative frame exit angle, β_2, as a function of β_1. Again, it must be emphasized that these angles represent only local values measured at the point where the local axial velocity was equal to the average axial velocity.

COMPARISON OF RESULTS FOR UNDISTORTED AND DISTORTED FLOW CONDITIONS

In order to highlight what are considered to be the more important differences between the two flow conditions, selected results from the two cases will be superimposed. To avoid confusion, only the curves fitted through the data points will be presented. Some of the curves exhibit a great deal of data scatter. The reader is referred back to the original plots to make a decision as to the confidence to be placed in these plots.

Figure 23 shows the variation of the rotor pressure rise coefficient with C_x/U. As pointed out before, the pressure rise is higher for the distorted flow condition at low values of C_x/U. The implication is that at high blade loading the unsteadiness introduced by the distortion enhances the ability of the rotor to generate a pressure rise. As the C_x/U parameter increases (decreasing the blade loading) the gain due to the unsteadiness diminishes so that finally the undistorted flow condition generates the greater pressure rise. Rotating stall seems to be entered at approximately the same value of C_x/U for both flow conditions with the same pressure rise in the stalled condition at that point. The stalled pressure rise for the undistorted case seems to parallel the unstalled curve at a consistently lower pressure rise coefficient, whereas the distorted case does not appear to behave in this manner.

Figures 24 and 25 show the blade pressure distributions for a $C_x/U = 1.01$ and $C_x/U = 0.55$, respectively. For $C_x/U = 1.01$ (figure 24) it is apparent that the pressure reversal on the leading edge is stronger for the distorted case. Furthermore, there is a rapid rise in the pressure coefficient at the trailing edge of the pressure surface in the distorted case which does not occur for undistorted

flow. The source of this phenomena is unknown but it persists over a wide range of C_x/U. For $C_x/U = 0.55$ (figure 25) the shape of the two pressure distributions is quite similar. For both flow conditions, however, the distorted pressure coefficient distribution is shifted upward when compared to that for undistorted flow.

The plots of normal force and pitching moment coefficient as functions of β_1 obtained by integrating the blade pressure distributions are presented in figures 26 and 27, respectively. The normal force curve of figure 26 shows that the distorted flow condition results in higher normal force at a given value of β_1 for the lower values of β_1. The curves merge as β_1 increases. Actually, two types of unsteady effects come into play. First, the relative angle of attack of an individual blade oscillates up and down as the blade transverses the distorted flow field. Second, at the same time the relative frame resultant velocity fluctuates. The average dynamic pressure based on this resultant velocity is consistently higher than the dynamic pressure based on the average relative velocity. An approach similar to that in Appendix B will illustrate this fact. Both factors can increase the normal force coefficient of an isolated airfoil, the first being more important at low values of β_1 and the second being more important at high values of β_1. These two effects in concert with cascade effects are probably responsible for the behavior exhibited in figure 26. The variation of pitching moment coefficient with β_1 is shown in figure 27. At the lowest values of β_1 for which the rotor was not stalled, the values are virtually identical but diverge as β_1 increases. The variation of the location of the blade's center of pressure is illustrated in figure 28.

The total pressure loss characteristic is presented in figure 29. The undistorted case is about what one would expect; however, the distorted case exhibits a large region of negative loss. As was previously explained,

this is only a local behavior at a circumferential station where the axial velocity is equal to the average axial velocity. If it were true that the rotor undergoing inlet distortion would locally follow the undistorted loss characteristic (a common assumption in theoretical inlet distortion work) the curves should be identical at this point. Since they obviously are not the same, one must conclude that this assumption is in error. Observing that the direction of rotation is such that a rotor blade has passed through the region of highest velocity one-quarter revolution before entering the region at which this loss coefficient is calculated, the possibility arises that energy is somehow being transported into this region from the high velocity region by the rotor. A detailed investigation of the local loss coefficient as a function of circumferential station will be required to resolve this question.

Finally, figure 30 compares the variation in exit flow angle for the two flow conditions. In the undistorted case, it is interesting to note that the exit angle approaches 65° for high β_1. This angle corresponds to flow leaving the blade parallel to the trailing edge tangent line. For distorted flow, there is no evidence of this behavior.

CONCLUSIONS

The results presented indicate that the rotating stall encountered in the LSRR was essentially a leading edge phenomena. The leading edge pressure distribution on the rotor blade and the flow immediately upstream of the rotor changed abruptly with the onset of rotating stall while the pressure distribution on the rear part of the blade and the rotor exit flow showed very little change.

Unsteadiness introduced into the flow by the distortion increased the normal force coefficient for conditions of high blade loading over that of the undistorted case. A similar increase was evident in the pressure rise across the rotor when the distortion was introduced. As the blade loading decreased, the pressure rise became greater for the undistorted case.

It was found that the rotor does not follow the undistorted total pressure loss characteristic locally while in a distorted flow field. There appears to be some mechanism for circumferential energy transport which resulted in a locally negative loss coefficient for the particular location at which this parameter was measured. A circumferential survey of the total pressure loss coefficient seems to be in order to clarify this aspect of the rotor's performance.

The conclusions presented here are considered valid for the particular configuration tested. While they may, in fact, be true in general, it is impossible to make such a sweeping statement based on a single experimental program.

References:

1. "Transients in Turbocompressors", J. N. Perkins, L. W. Hardin, F. O. Carta, W. C. Griffith. Final Report on AFOSR Grant No. 75-2808, N. C. State University, Engineering Design Center, Report No. NCSU/EDC-76-1. February, 1976. Government Accession No. ADA 024275.
2. "Transients in Turbocompressors", W. C. Griffith, L. W. Hardin, J. N. Perkins, F. O. Carta. First Interim Report on AFOSR Contract No. F44620-76-C-0055. N. C. State University, Engineering Design Center, Report No. NCSU/EDC-76-2. July, 1976.
3. "Use of a Five-Hole Pneumatic Probe in Unsteady Flows", J. C. Bennett. United Technologies Research Center, Report No. UTRC76-41. March 25, 1976.
4. Numerical Calculus, Milne, William Edmund, Princeton University Press, 1949, pp. 285-290.
5. "The Measurement of Unsteady Pressures in Wind Tunnels", Eugene L. Davis, Jr. Agard Report No. 169, March 1958.

Appendix A

USE OF A GAUSSIAN ARRAY OF PRESSURE MEASURING STATIONS TO OBTAIN NORMAL FORCE AND PITCHING MOMENT COEFFICIENTS.

If the positions at which pressures are to be measured on an airfoil may be prescribed, large gains may be realized in the accuracy of the integrated normal force and pitching moment coefficients. Reference 5 indicates that an accuracy of 2 percent should be realized by the 6-element Gaussian array employed in the inlet distortion experiment. Further, the process of integrating the pressures to obtain normal force and pitching moment coefficients is reduced to a simple summation procedure. Breaking the normal force up into a contribution from the pressure surface and one from the suction surface we find:

$$\left(C_N\right)_{press} = \sum_{i=1}^{6} w_i \left(C_{p_i}\right)_{press} \tag{A.1}$$

$$\left(C_N\right)_{suct} = \sum_{i=1}^{6} w_i \left(C_{p_i}\right)_{suct} \tag{A.2}$$

and

$$C_N = \left(C_N\right)_{press} - \left(C_N\right)_{suct} \tag{A.3}$$

Similarly, the moment coefficient may be obtained by:

$$\left(C_M\right)_{press} = \sum_{i=1}^{6} w_i x_i \left(C_{p_i}\right)_{press} \tag{A.4}$$

$$\left(C_M\right)_{suct} = \sum_{i=1}^{6} w_i x_i \left(C_{p_i}\right)_{suct} \tag{A.5}$$

and finally

$$C_M = \left(C_M\right)_{suct} - \left(C_M\right)_{press} \tag{A.6}$$

In the event that one or more of the measuring stations was inoperative the procedure was modified as follows. Suppose that the first station on the suction surface were inoperative. Equation A.2 would be modified as follows:

$$\left(C_N\right)_{suct} = \frac{\sum_{i=2}^{6} w_i \left(C_{p_i}\right)_{suct}}{\sum_{i=2}^{6} w_i} \tag{A.7}$$

A similar modification would be necessary in equation A.5. This procedure effectively allows the pressure at the missing station to be replaced by a weighted average of the remaining stations on the same surface (pressure or suction) of the airfoil while maintaining the same relative weights of the operative stations.

Positions and Weighting Factors for a Six-Element Gaussian Array

Station	X_i	W_i
1	.0337652	.0856622
2	.1693953	.1803808
3	.3806904	.2339570
4	.6193096	.2339570
5	.8306047	.1803808
6	.9662348	.0856622

Appendix B

BEHAVIOR OF STATIC PRESSURE NEAR ROTOR ENTRANCE

It is convenient to consider the problem in the relative (rotor) reference system. For the undistorted case the flow far upstream of the rotor, i.e. on the order of one blade gap, is uniform and steady. The far upstream quanities will be denoted by the subscript ∞. As it approaches the rotor, the flow will become locally non-uniform due to the presence of blades.

The total pressure is given by

$$P_t = P_s + \frac{1}{2} \rho \left(C_w^2 + W_\theta^2 \right) \tag{B.1}$$

where C_x is the axial velocity which is the same for both the stationary and the relative frames and W_θ is the relative frame circumferential velocity. Performing a gap average, denoted by overbars,

$$\overline{P_t} = \overline{P_s} + \frac{1}{2} \left(\overline{C_x^2} + \overline{W_\theta^2} \right) \tag{B.2}$$

Upstream of the rotor viscous effects are negligible; hence,

$$\overline{P_t} = P_{t_\infty} \tag{B.3}$$

Writing the axial and circumferential velocities as the sum of a constant part equal to the far upstream value plus a varying part:

$$C_x = C_{x_\infty} + \delta C_x \tag{B.4}$$

$$W_\theta = W_{\theta_\infty} + \delta W_\theta \tag{B.5}$$

From continuity

$$\overline{C_x} = C_{x_\infty} \tag{B.6}$$

therefore

$$\overline{\delta C_x} = 0 \quad . \tag{B.7}$$

By Kelvin's theorem

$$\overline{W_\theta} = W_{\theta_\infty} \quad . \tag{B.8}$$

So

$$\overline{\delta W_\theta} = 0 \quad . \tag{B.9}$$

The averages of the squared quanities in equation B.2 may now be written

$$C_x^2 = C_{x_\infty}^2 + \overline{(\delta C_x)^2} \tag{B.10}$$

and

$$\overline{W_\theta^2} = W_{\theta_\infty}^2 + \overline{(\delta C_x)^2} \quad . \tag{B.11}$$

Noting that

$$P_{t_\infty} = P_{s_\infty} + \frac{1}{2} \rho \left[C_{x_\infty}^2 + W_{\theta_\infty}^2 \right] \quad . \tag{B.12}$$

It is now possible to transform equation B.2 into the form

$$\overline{P_s} = P_{s_\infty} - \frac{1}{2} \left[\overline{(\delta C_x)^2} + \overline{(\delta W_\theta)^2} \right] \tag{B.13}$$

Thus, it is obvious that as the flow approaches the rotor and the magnitudes of the fluctuations increase, the average of the static pressure in the rotating frame must decrease from its far upstream value. As the static pressure is the same in both the relative and the stationary reference frames, the same

trend must be observed in the behavior of the casing static pressures. The magnitude of this pressure decrease should be directly proportional to blade loading. The length scale over which this phenomena is observed should be on the order of the blade gap divided by π.

It should be noted that this derivation is not applicable to flow through the blade passages as equation B.9 is certainly invalid in that region.

β_1	β_2	C_N	C_M	X_{ss}	C_{p_r}	C_x/U	C.P.	Flow Condition
61.231	40.662	1.017	-0.363	0.189	0.532	0.549	0.357	U
56.638	38.942	1.166	-0.451	0.011	0.701	0.658	0.387	U
53.606	34.498	1.268	-0.505	-0.057	0.830	0.737	0.399	U
50.671	25.286	1.329	-0.566	0.017	0.820	0.819	0.426	U
49.144	26.535	1.277	-0.576	0.031	0.758	0.865	0.451	U
46.268	25.185	1.425	-0.688	0.036	0.728	0.957	0.482	U
44.800	26.311	1.414	-0.717	0.036	0.679	1.007	0.507	U
41.846	26.733	1.430	-0.843	0.054	0.562	1.117	0.590	U
39.652	26.209	1.312	-0.906	0.129	0.331	1.207	0.691	U
61.031	34.977	1.022	-0.360	0.194	0.595	0.554	0.352	D
56.550	32.923	1.208	-0.522	0.067	0.720	0.661	0.432	D
53.226	34.551	1.254	-0.635	-0.033	0.785	0.747	0.506	D
49.795	31.305	1.393	-0.753	-0.053	0.826	0.845	0.540	D
47.976	30.970	1.413	-0.806	-0.020	0.743	0.901	0.570	D
46.293	30.017	1.434	-0.850	0.002	0.691	0.956	0.593	D
44.851	28.235	1.410	-0.889	0.043	0.622	1.005	0.630	D
61.301	23.259	0.830	-0.359	0.353	0.486	0.547	0.434	D,S
63.639	48.257	0.731	-0.332	0.242	0.390	0.496	0.455	D,S
59.165	48.884	0.915	-0.421	-0.030	0.573	0.597	0.460	D,S
61.383	22.032	0.866	-0.429	0.373	0.466	0.546	0.495	U,S
60.404	19.468	0.898	-0.439	0.364	0.478	0.568	0.489	U,S
59.543	17.700	0.870	-0.434	0.346	0.498	0.588	0.499	U
46.511	N/A	1.567	-0.811	N/A	0.711	0.949	0.518	D
61.887	N/A	1.076	-0.383	N/A	0.531	0.534	0.355	D,S
47.393	N/A	1.416	-0.700	N/A	0.748	0.920	0.494	U
58.438	N/A	1.069	-0.453	N/A	0.522	0.614	0.424	U,S
57.989	N/A	1.050	-0.442	N/A	0.628	0.625	0.421	U

Key to Flow Condition Column: U - Undistorted
D - Distorted
S - Stalled

Note: Data are presented in the chronological order in which they were taken

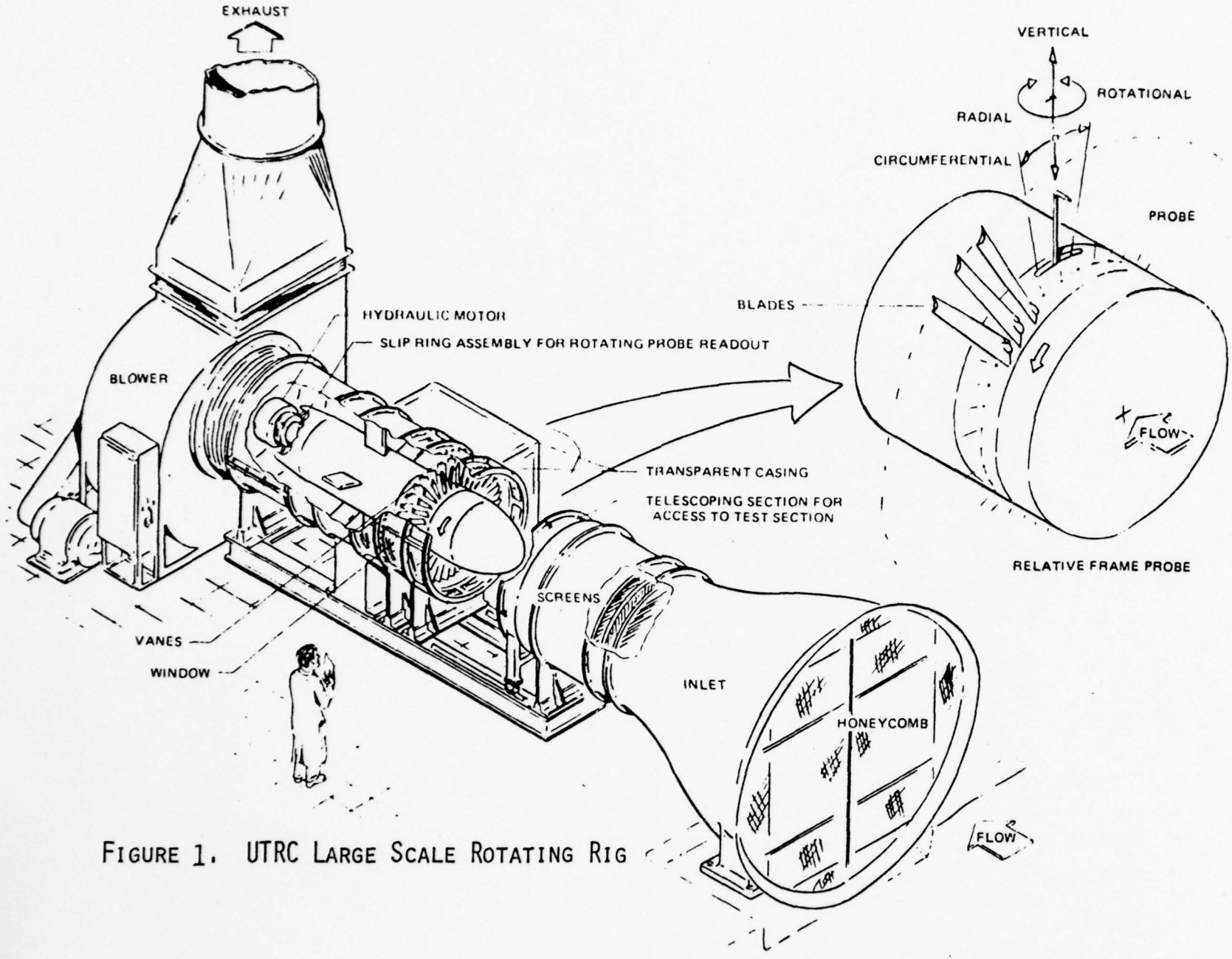

FIGURE 1. UTRC LARGE SCALE ROTATING RIG

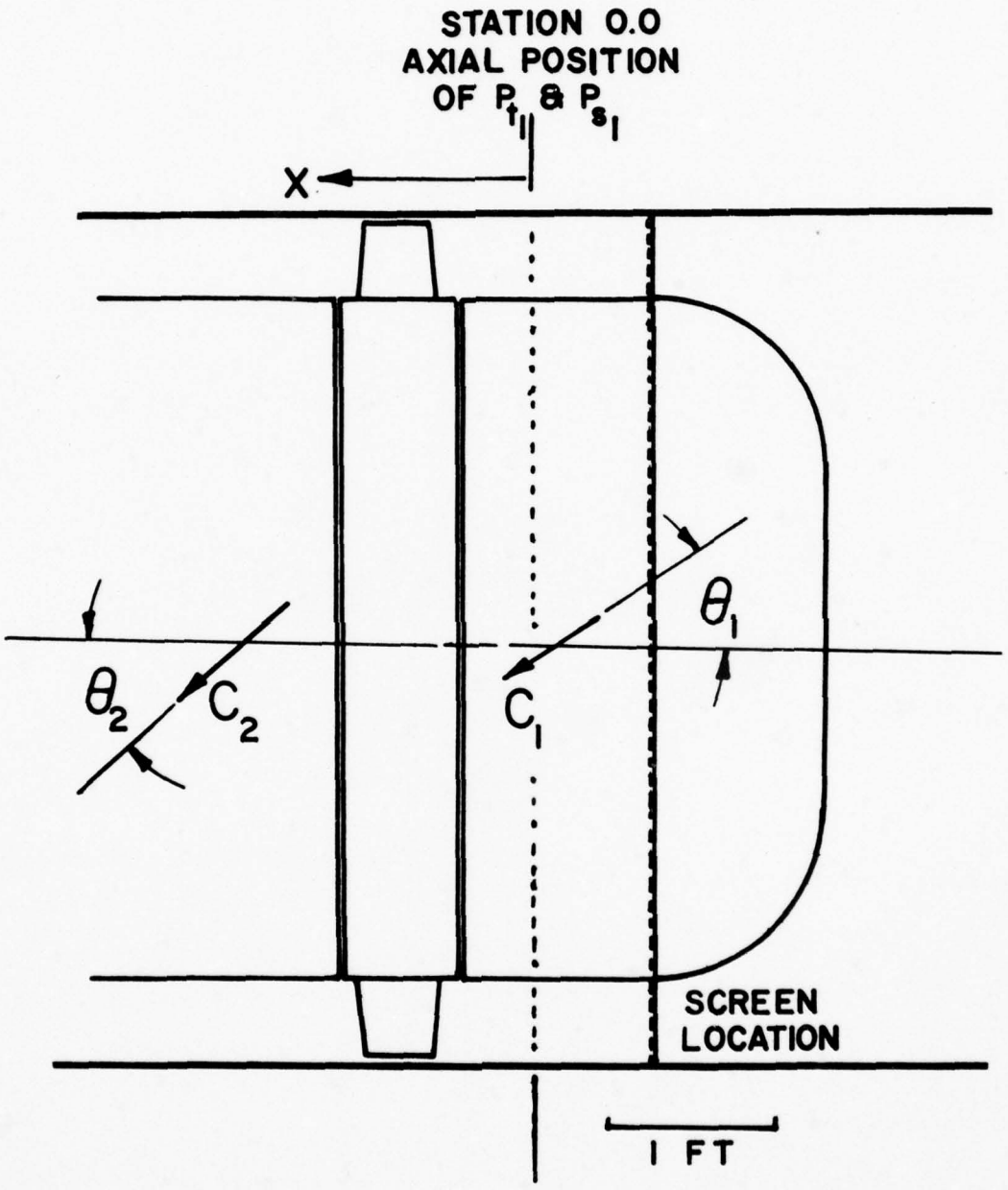

FIGURE 2. STATIONARY REFERENCE FRAME NOMENCLATURE

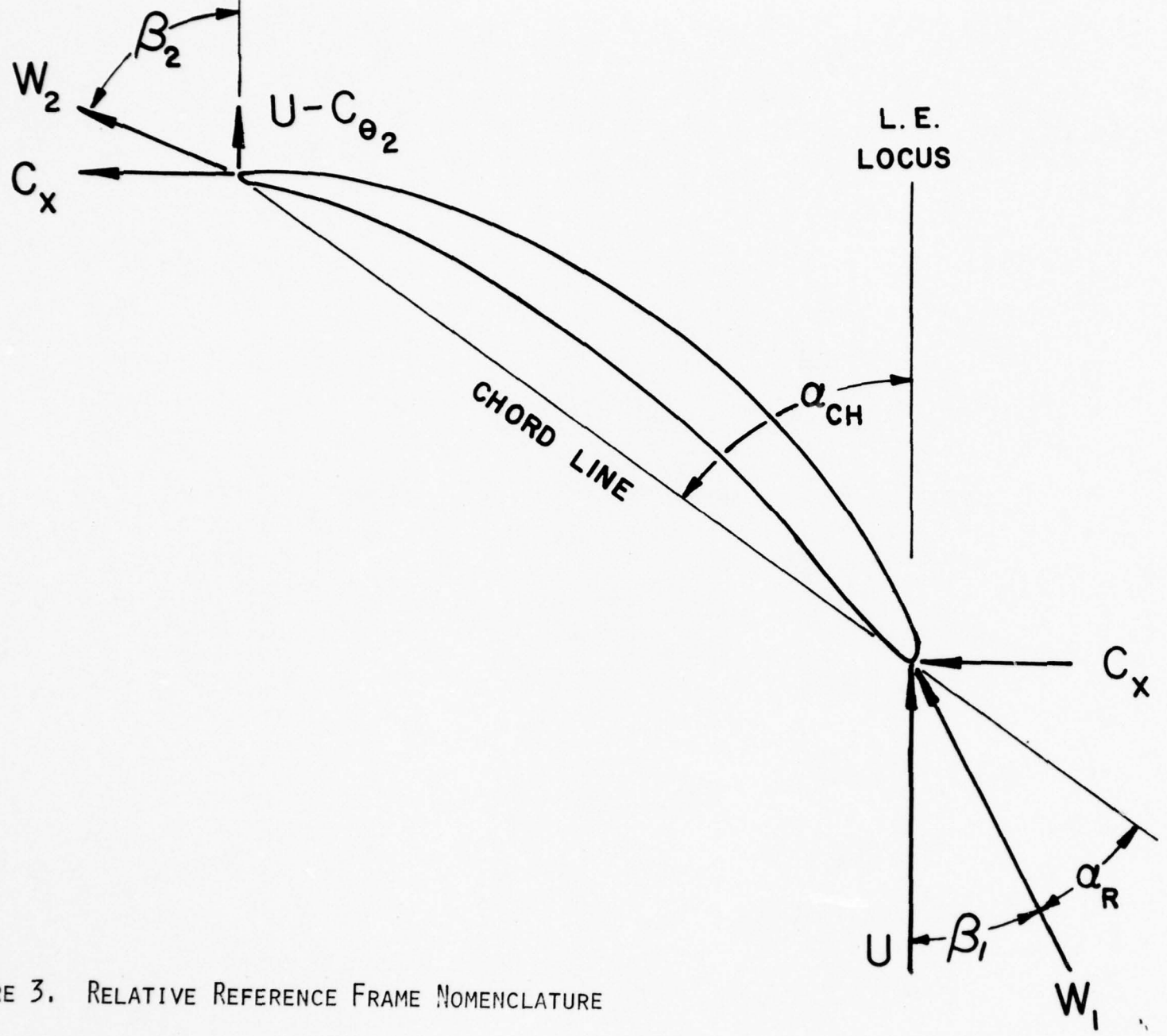

FIGURE 3. RELATIVE REFERENCE FRAME NOMENCLATURE

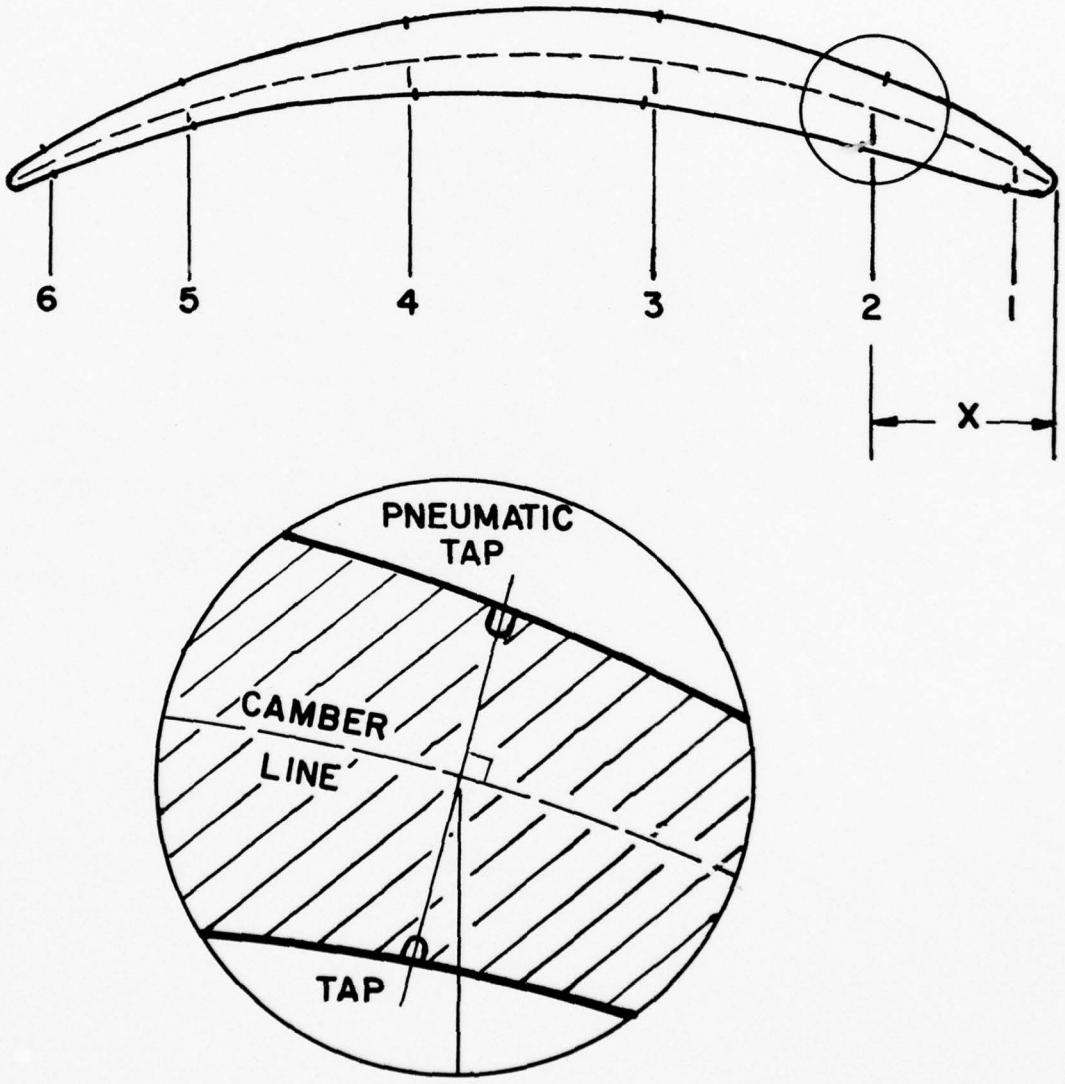

FIGURE 4. ROTOR BLADE INSTRUMENTATION LOCATIONS

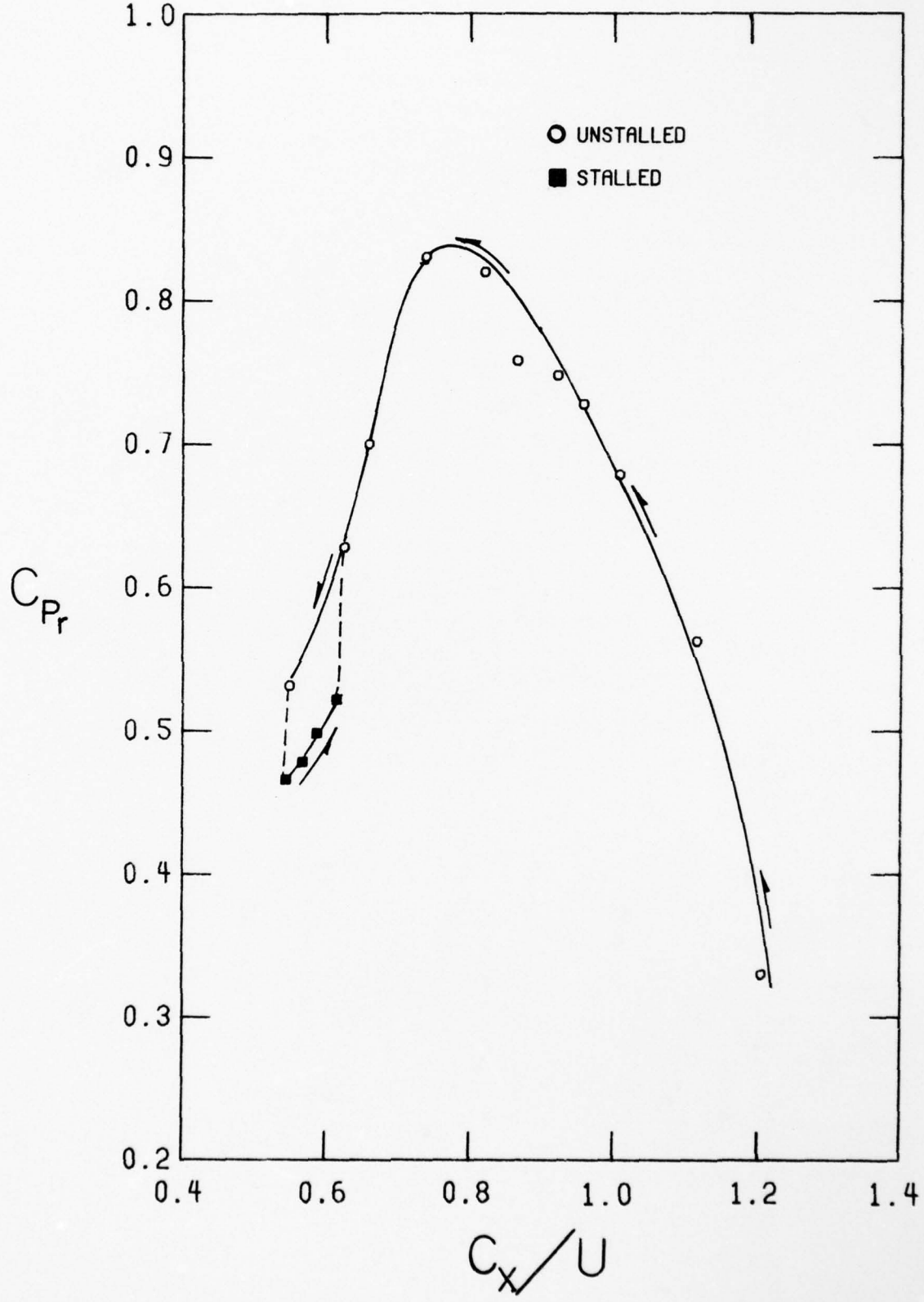

FIGURE 5 . UNDISTORTED FLOW ROTOR PRESSURE RISE

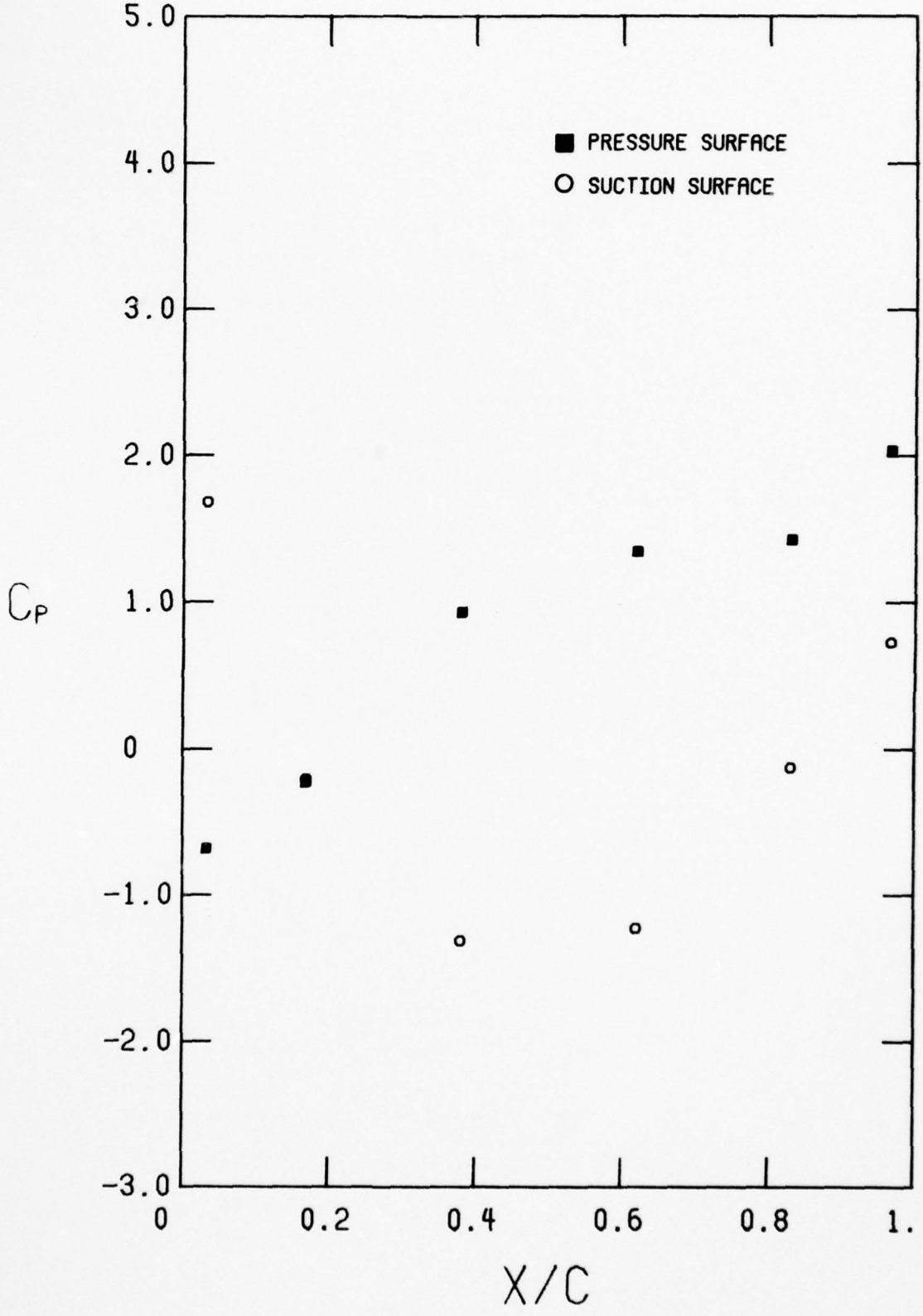

FIGURE 6. UNDISTORTED FLOW BLADE PRESSURE DISTRIBUTIONS
A. $C_X/U = 1.207$

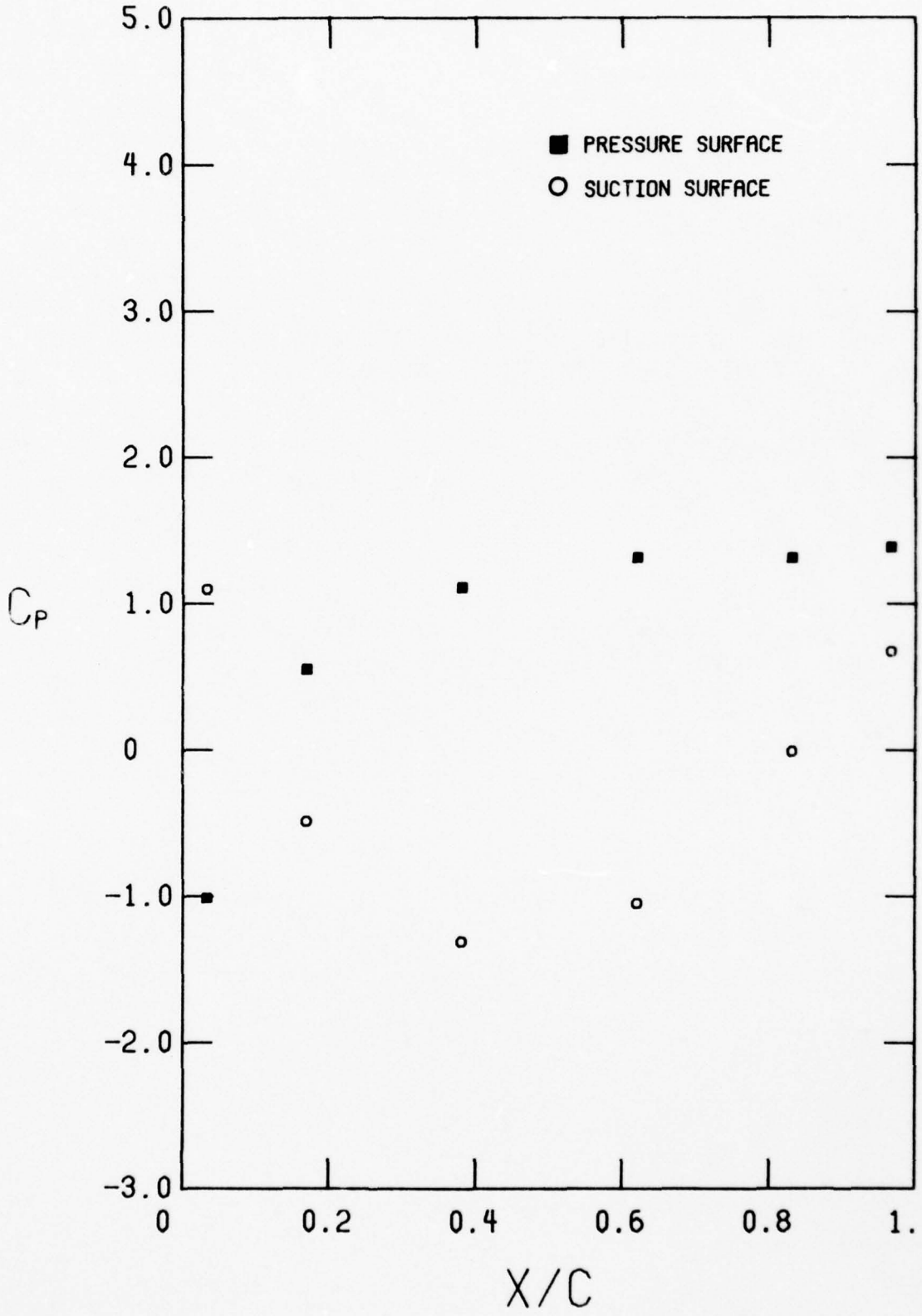

FIGURE 6. CONTINUED
B. $C_X/U = 1.117$

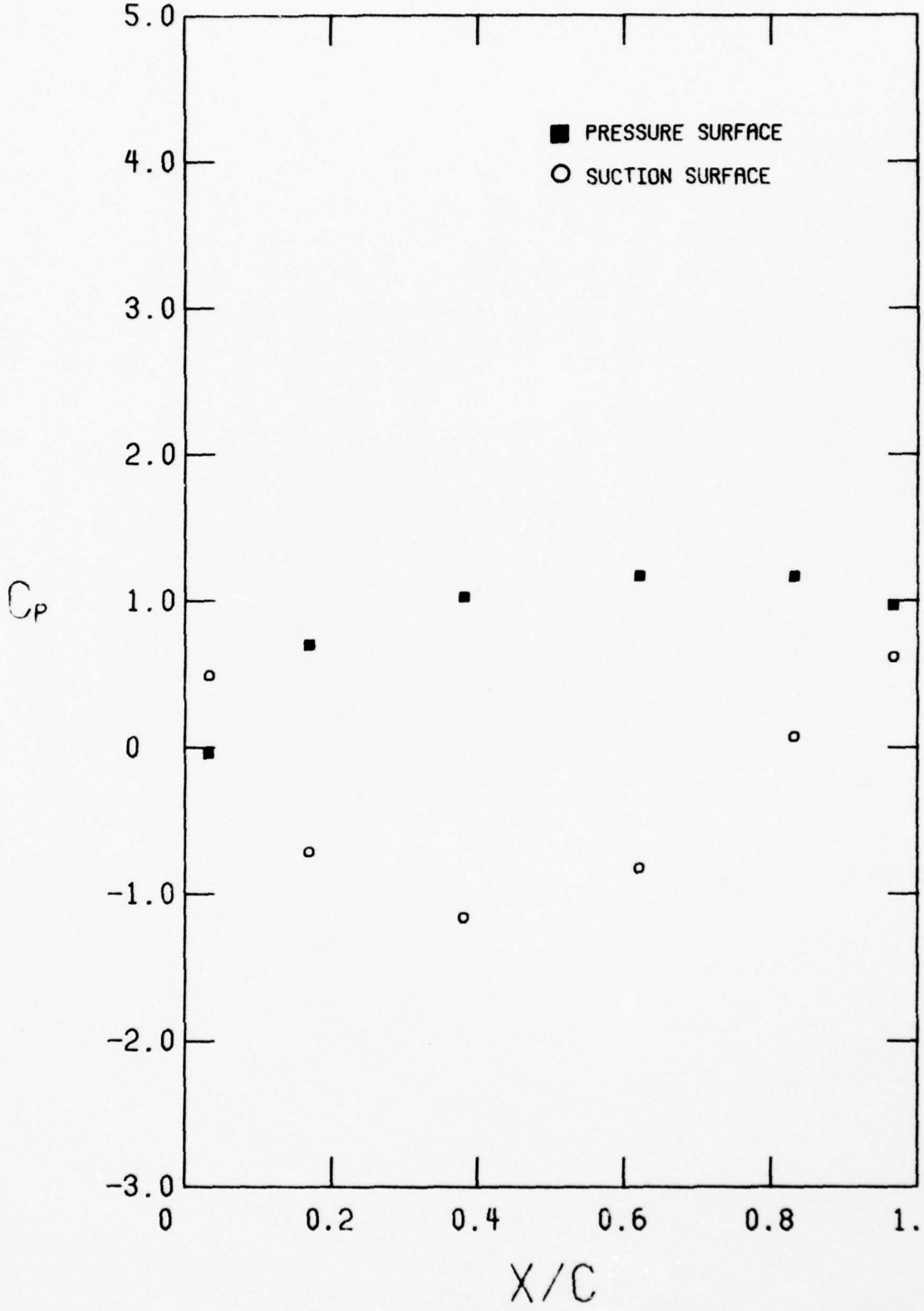

FIGURE 6. CONTINUED
c. $C_X/U = 1.007$

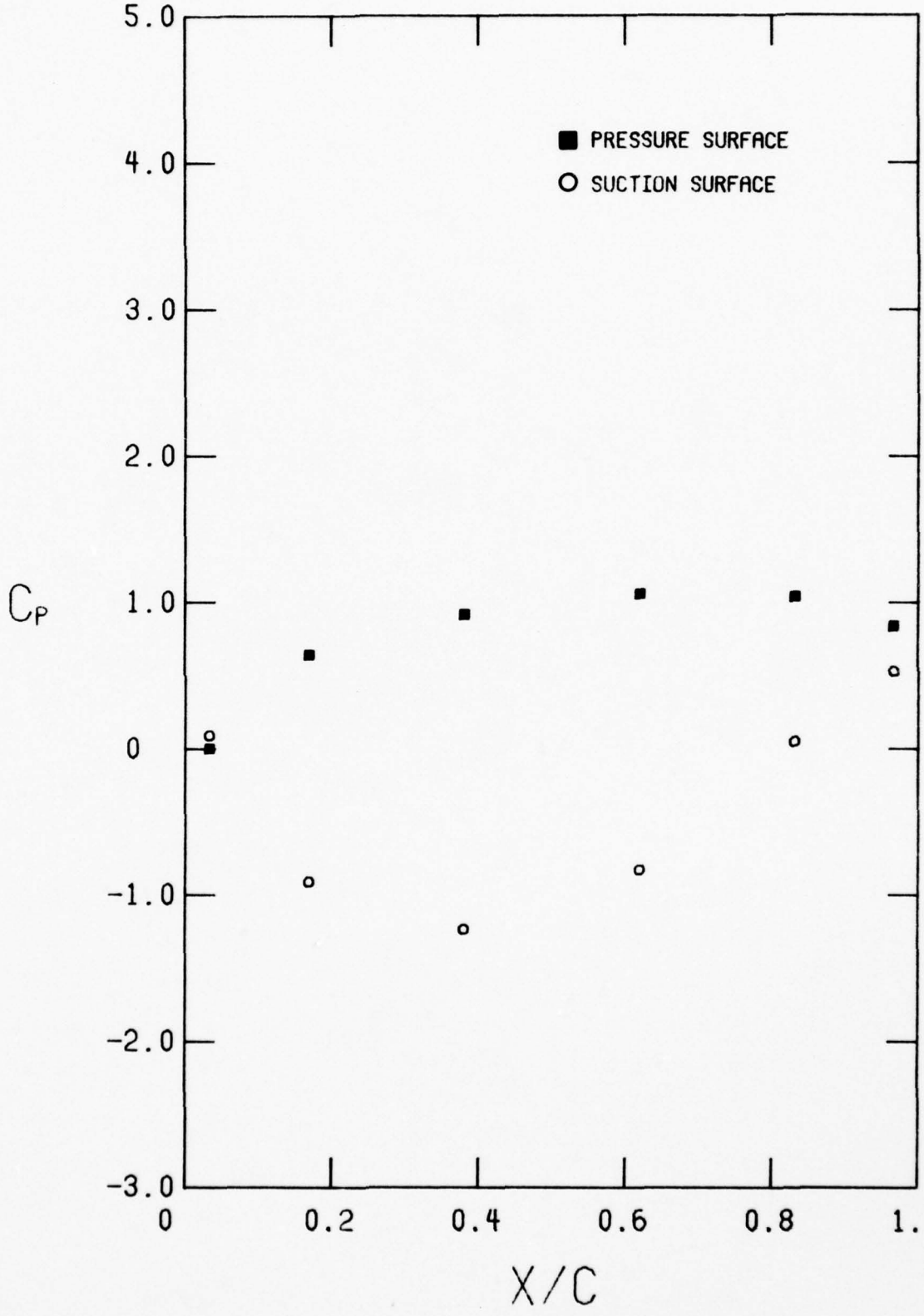

FIGURE 6. CONTINUED
D. $C_X/U = 0.957$

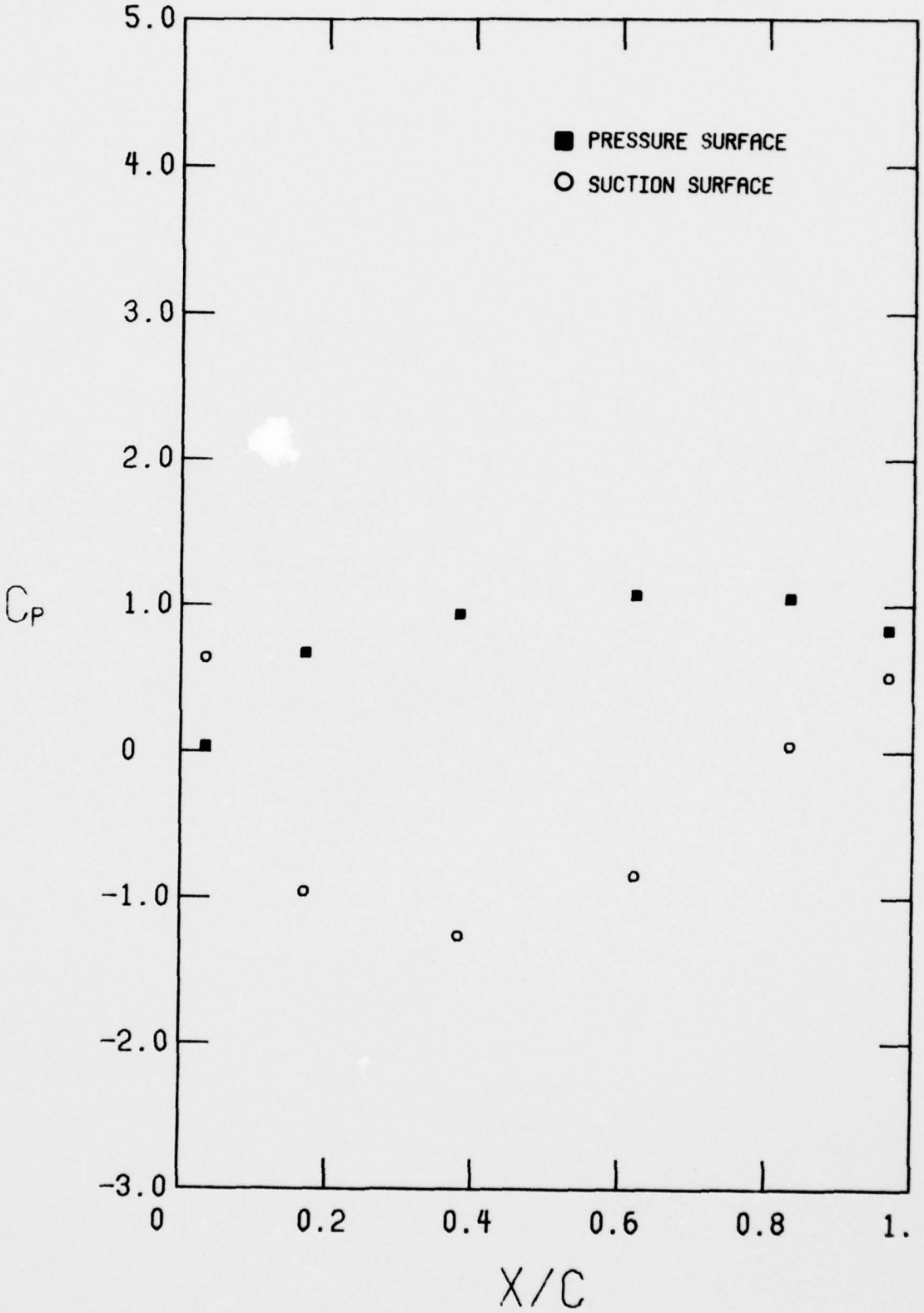

FIGURE 6. CONTINUED

E. $C_X/U = 0.920$

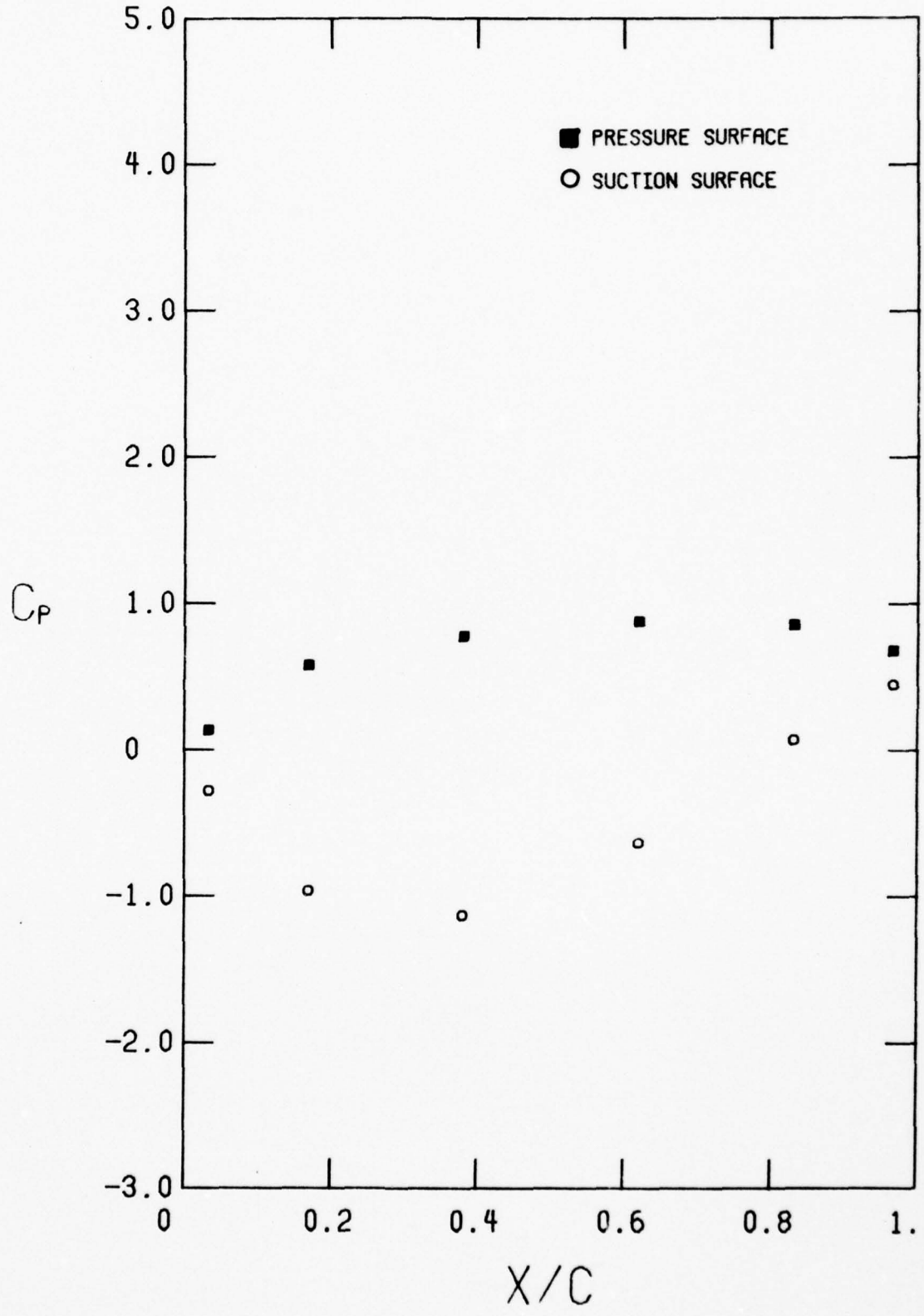

FIGURE 6. CONTINUED
F. $C_X/U = 0.865$

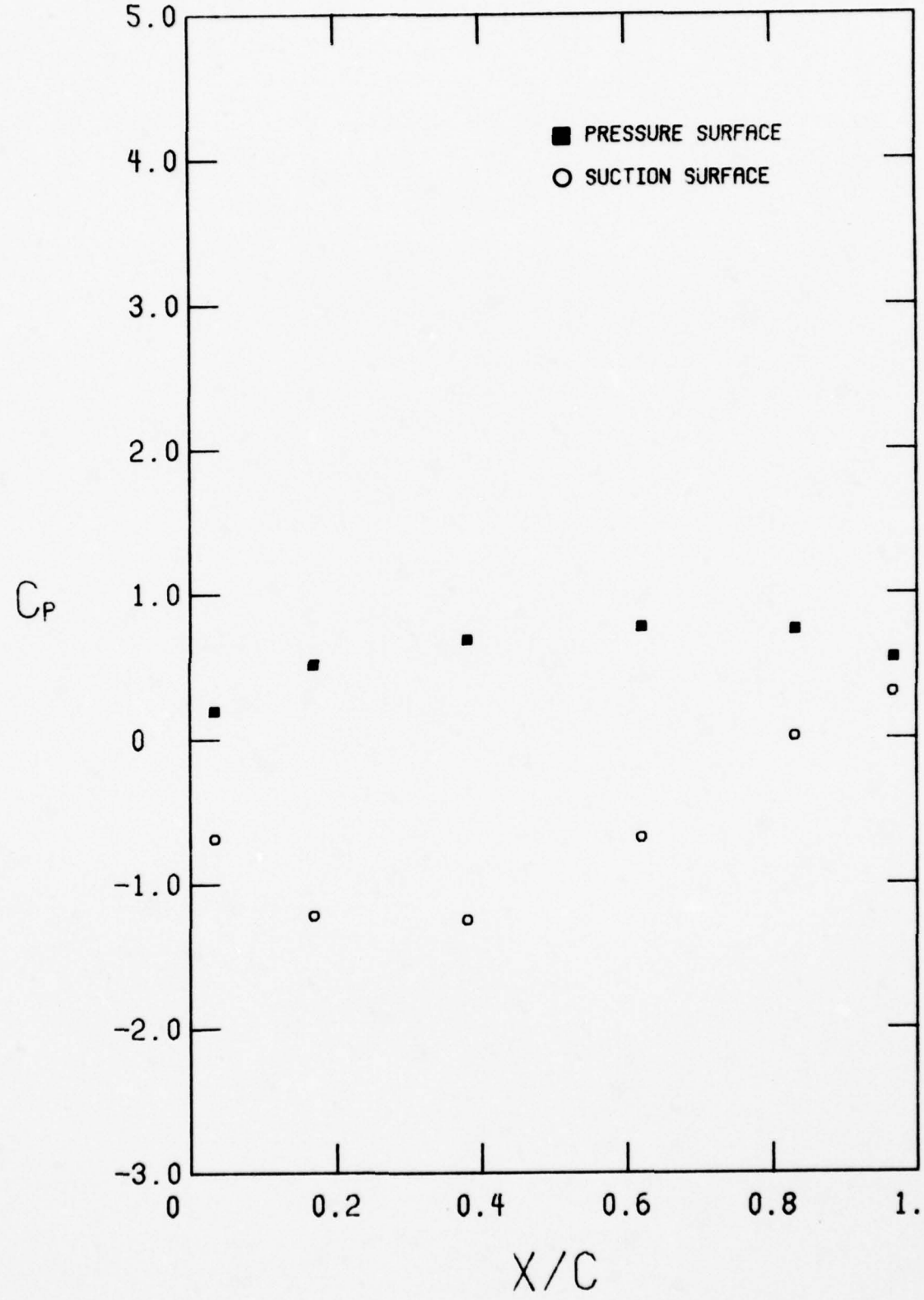

FIGURE 6. CONTINUED
G. $C_X/U = 0.819$

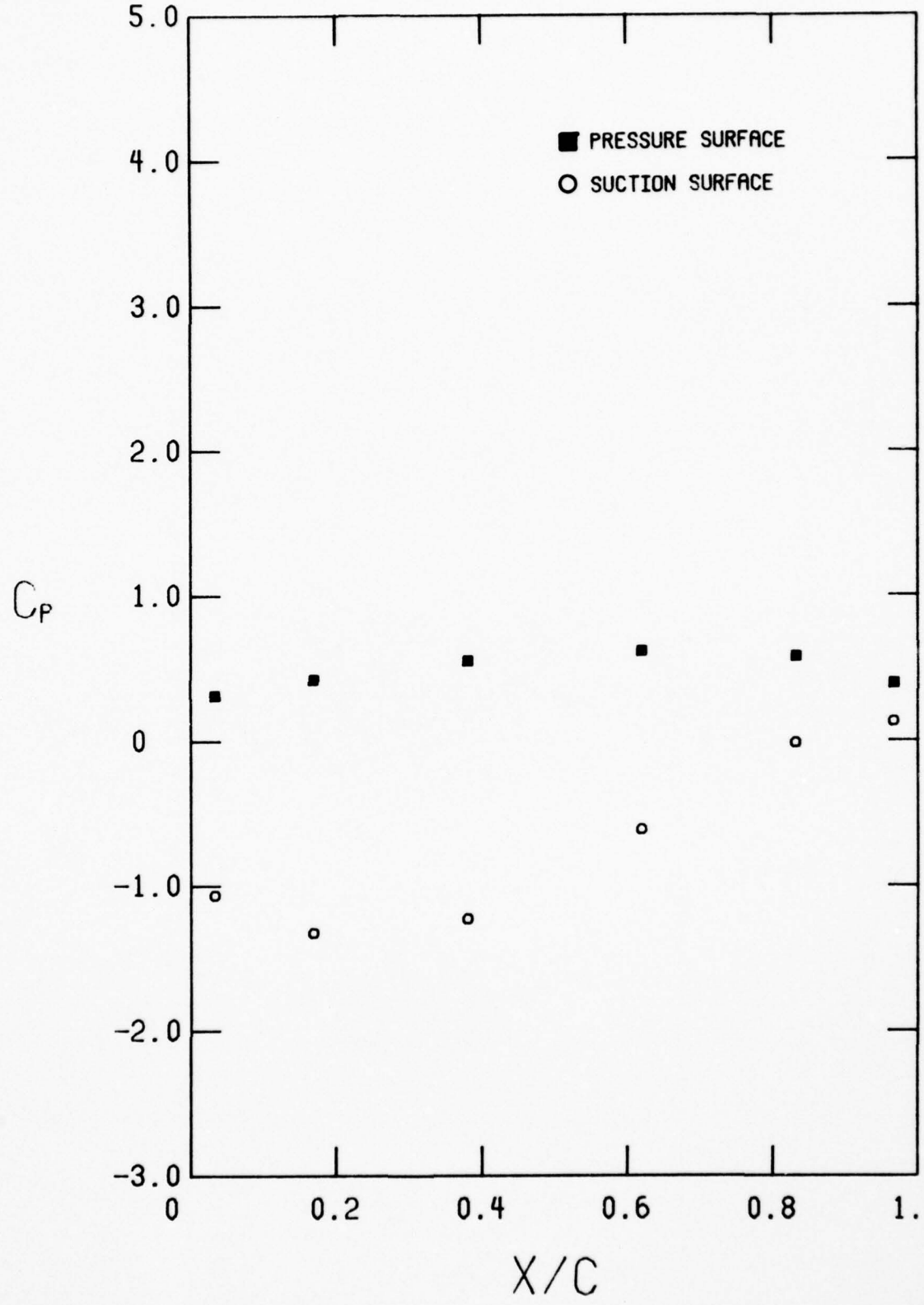

FIGURE 6. CONTINUED

H. $C_X/U = 0.737$

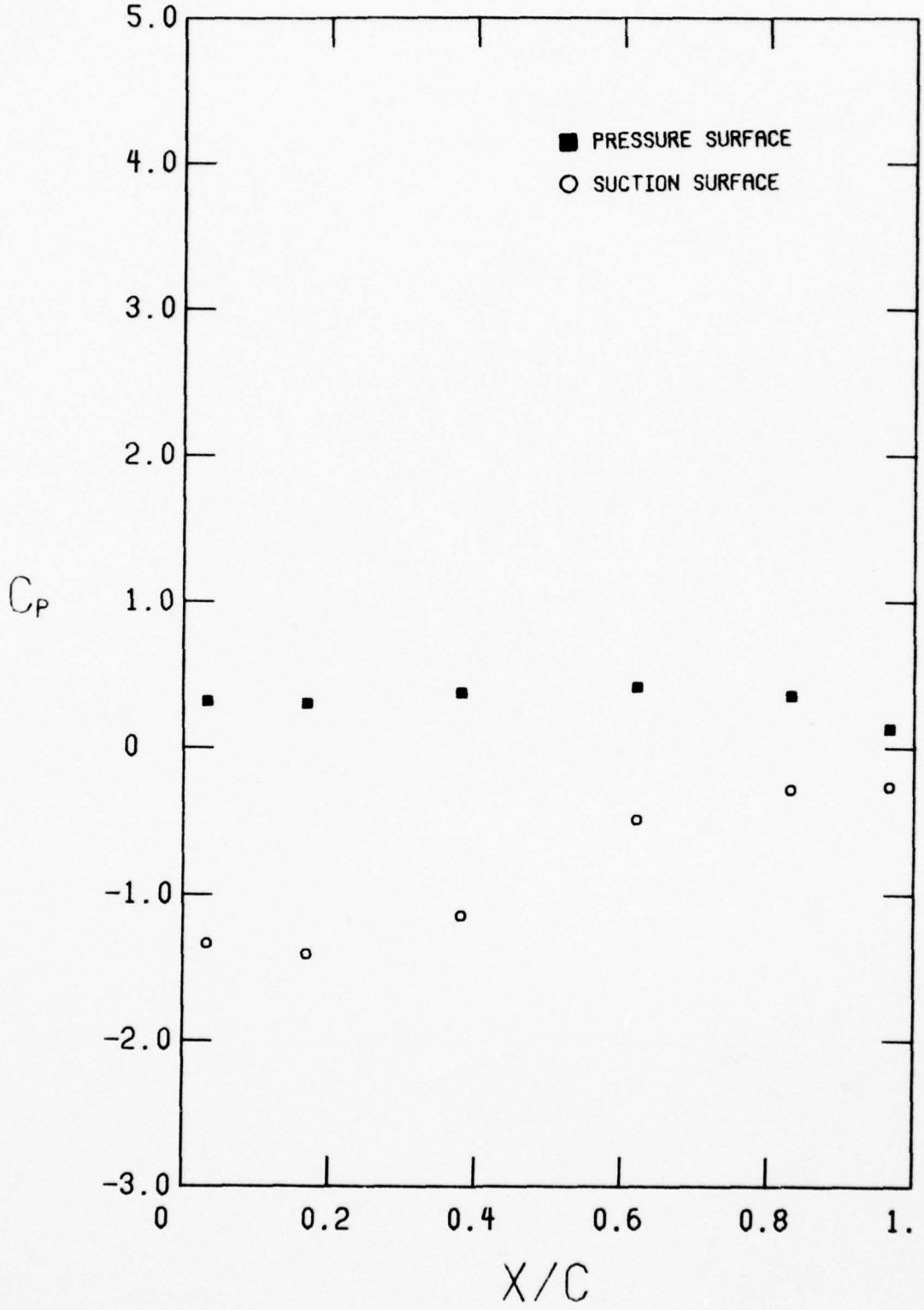

FIGURE 6. CONTINUED
I. $C_X/U = 0.658$

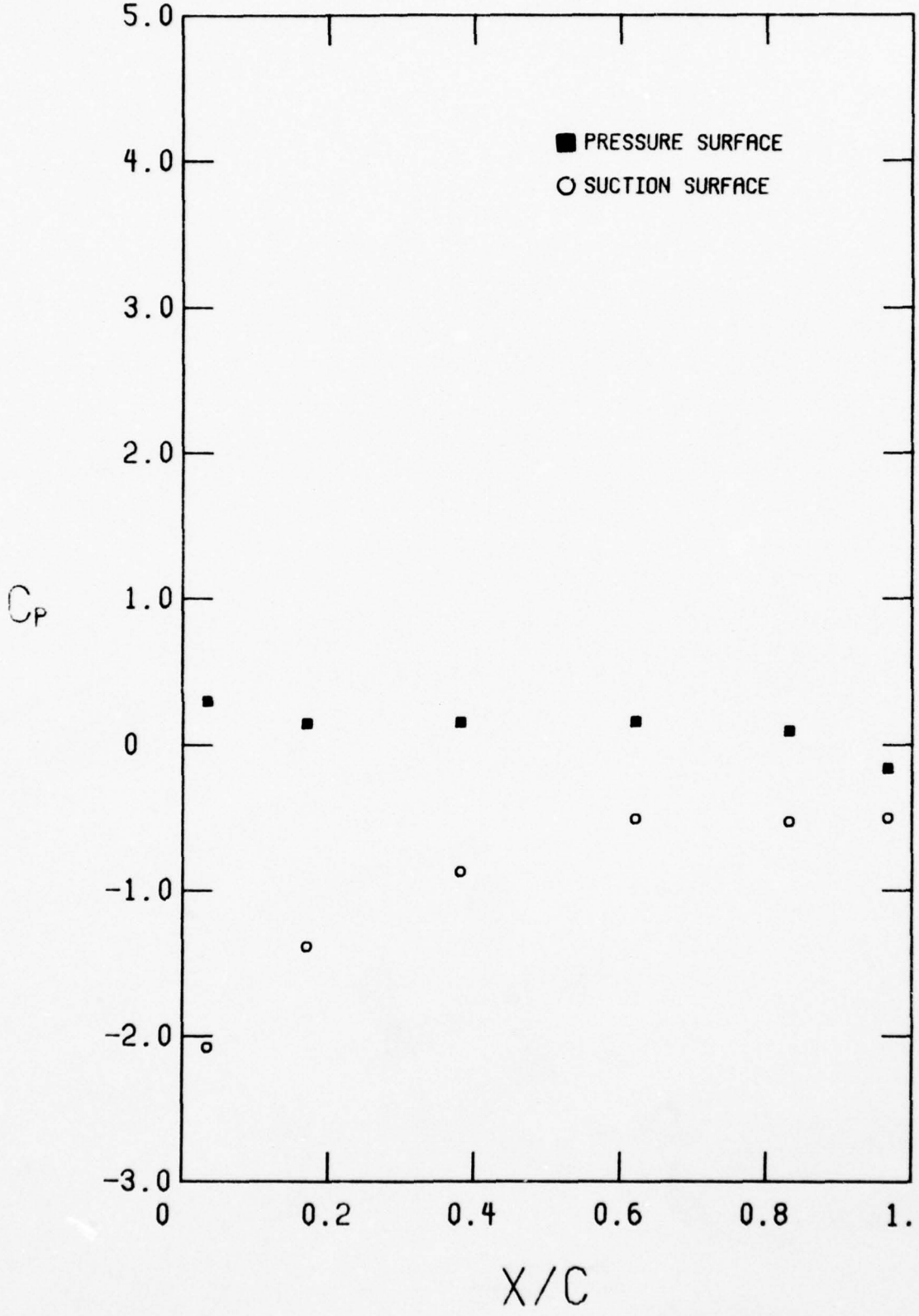

FIGURE 6. CONTINUED

J. $C_X/U = 0.549$

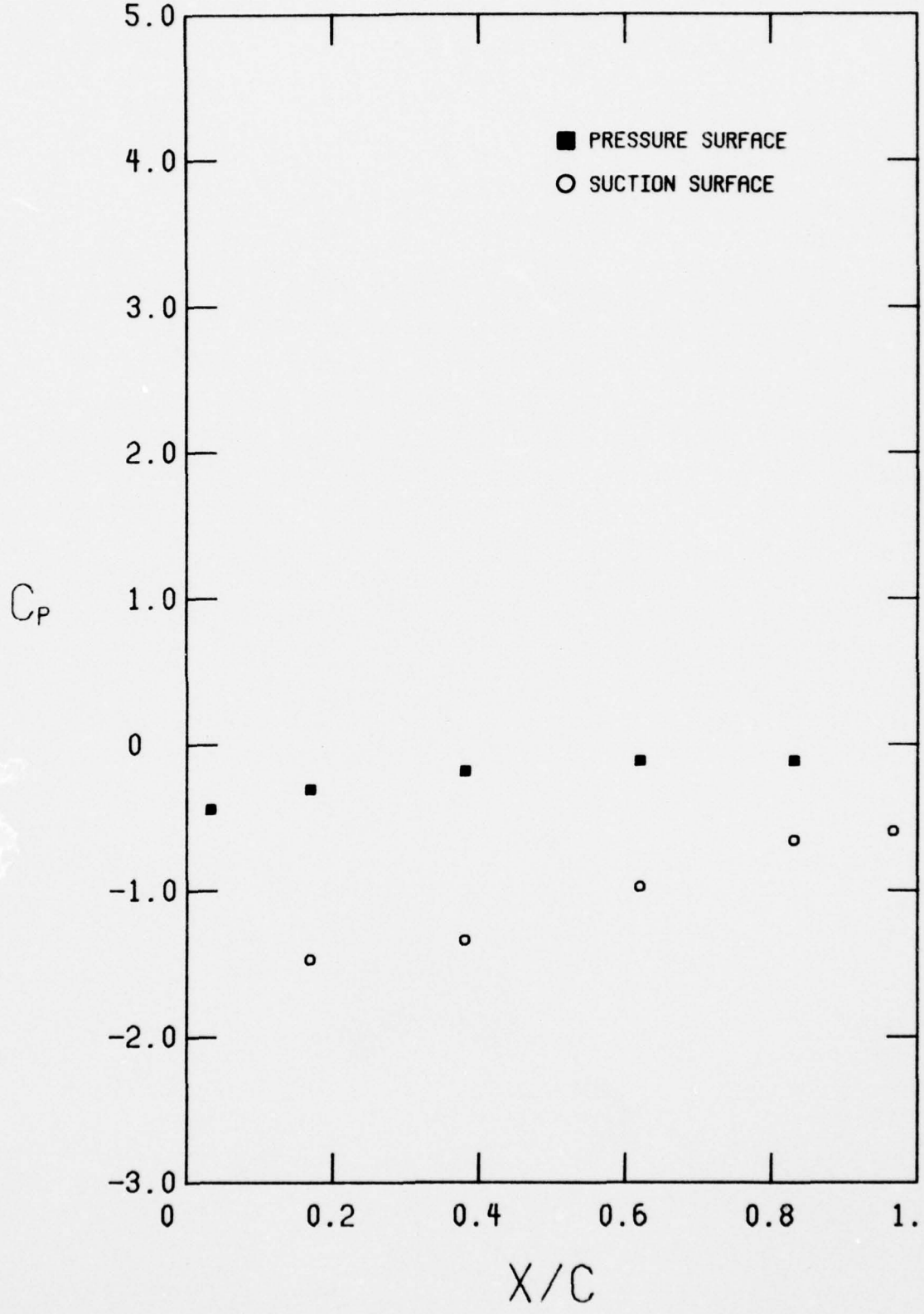

FIGURE 6. CONTINUED
K. $C_x/U = 0.546$ (STALL INCEPTION)

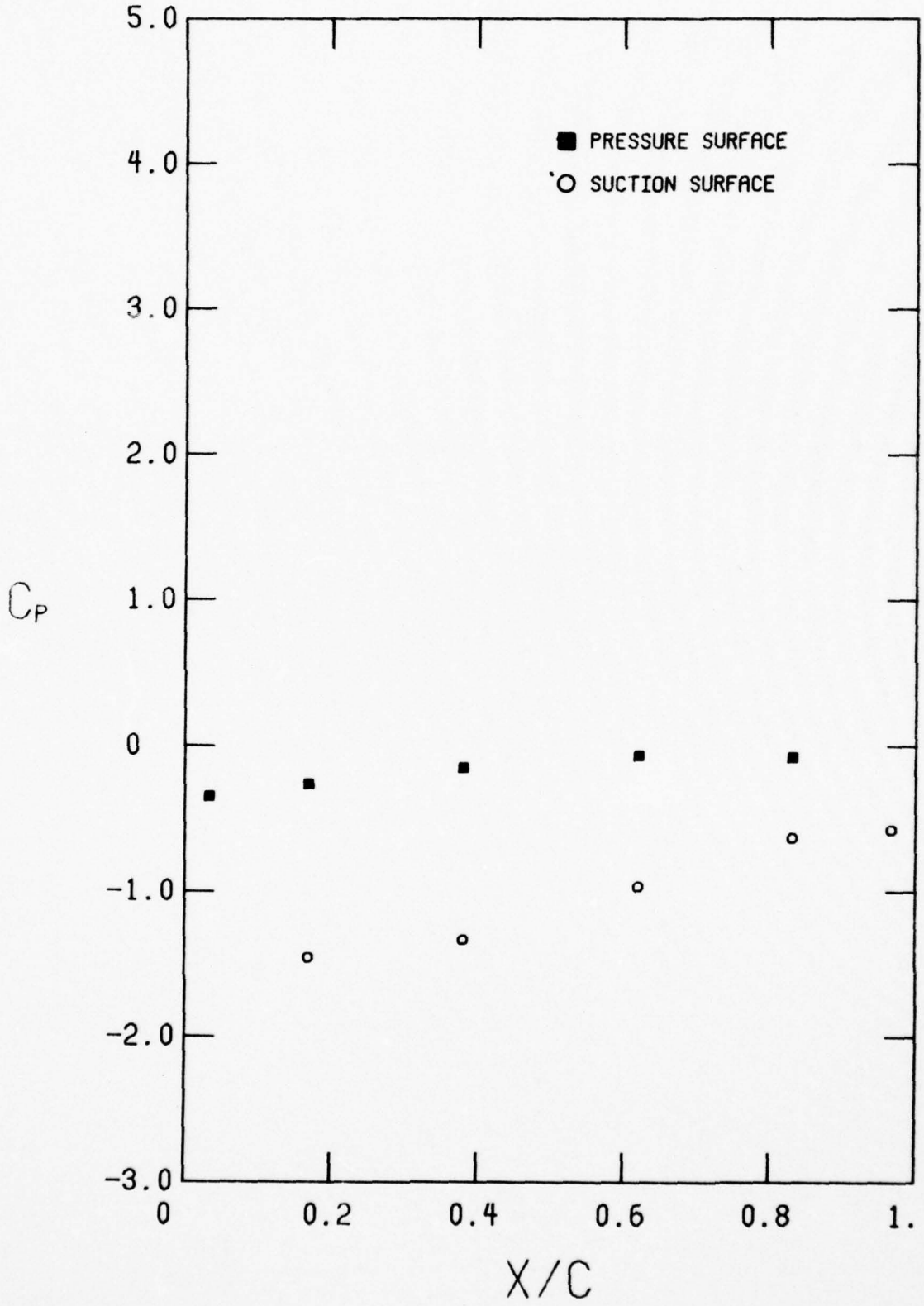

FIGURE 6. CONTINUED
L. $C_X/U = 0.568$ (STALLED)

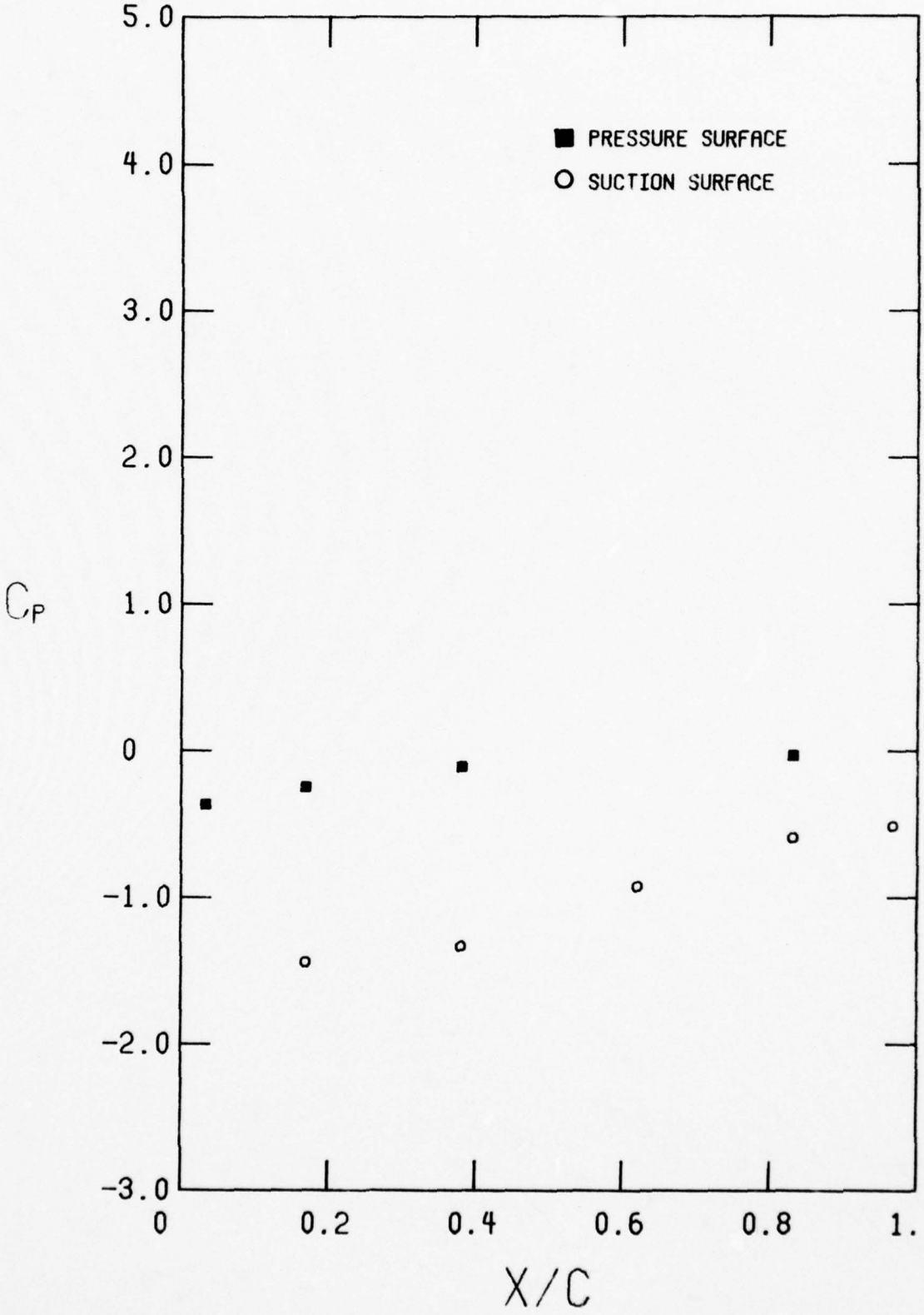

FIGURE 6. CONTINUED
M. $C_X/U = 0.588$ (STALLED)

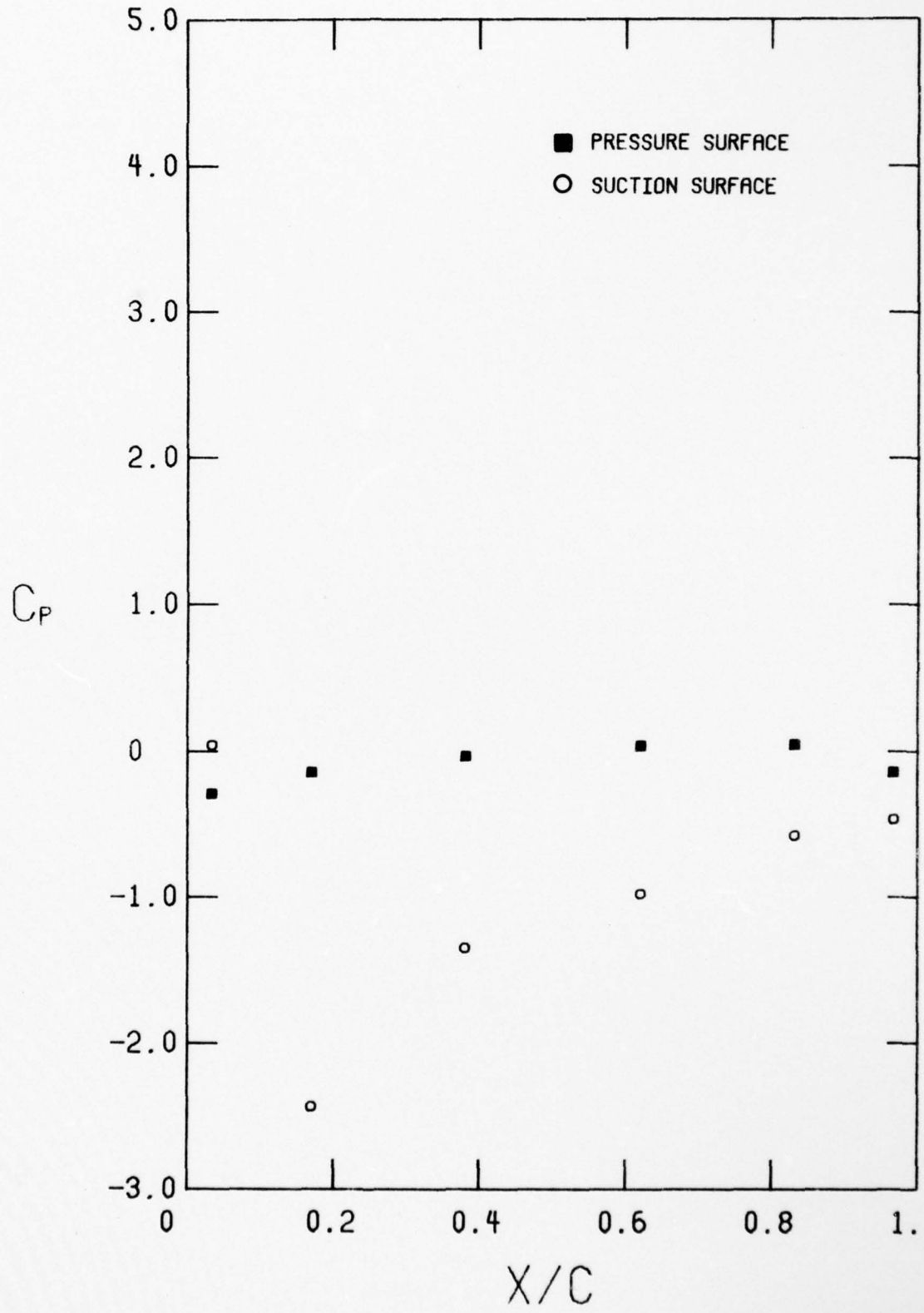

FIGURE 6. CONTINUED
N. $C_X/U = 0.614$ (STALLED)

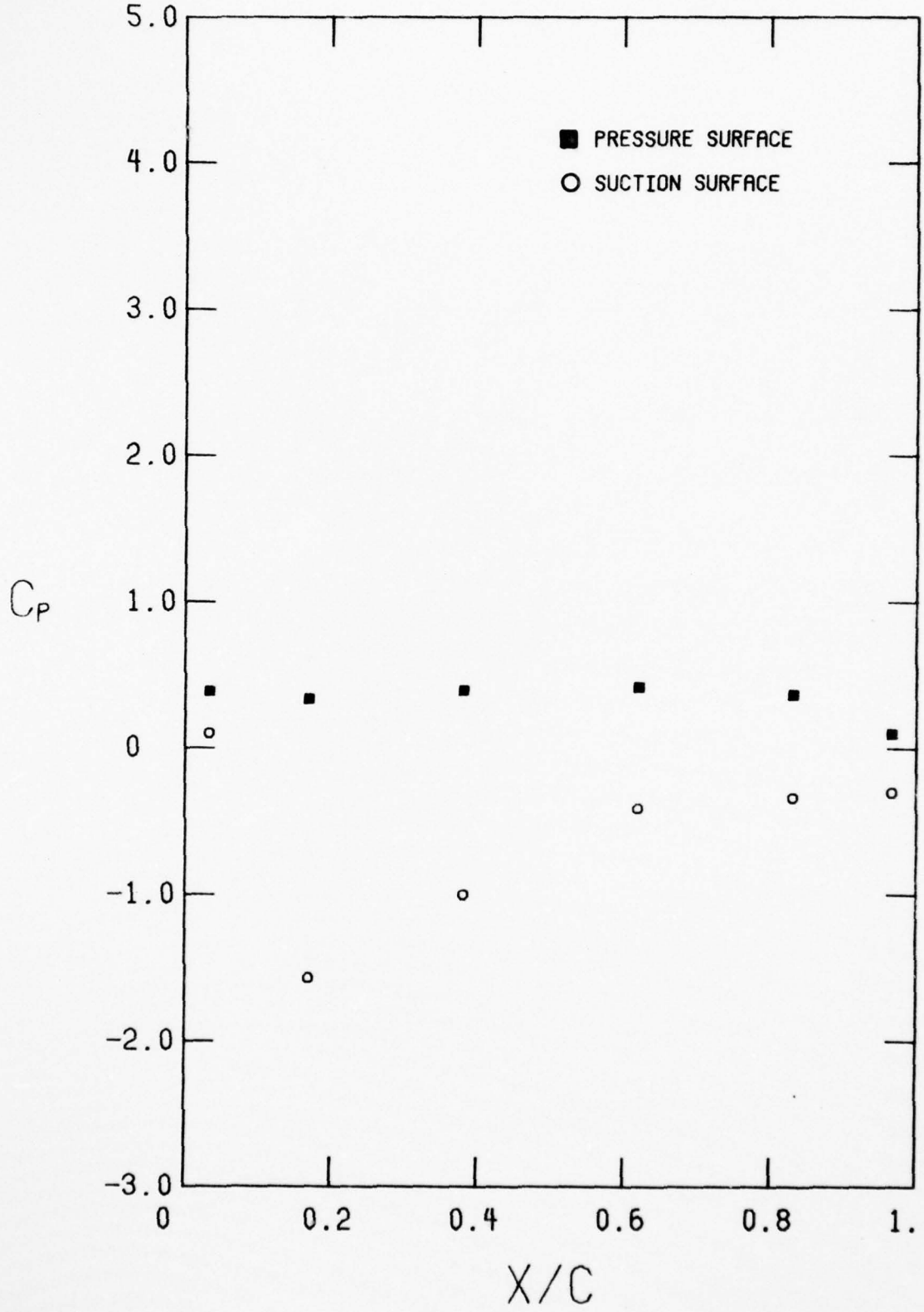

FIGURE 6. CONCLUDED

o. $C_X/U = 0.625$ (RECOVERY FROM STALL)

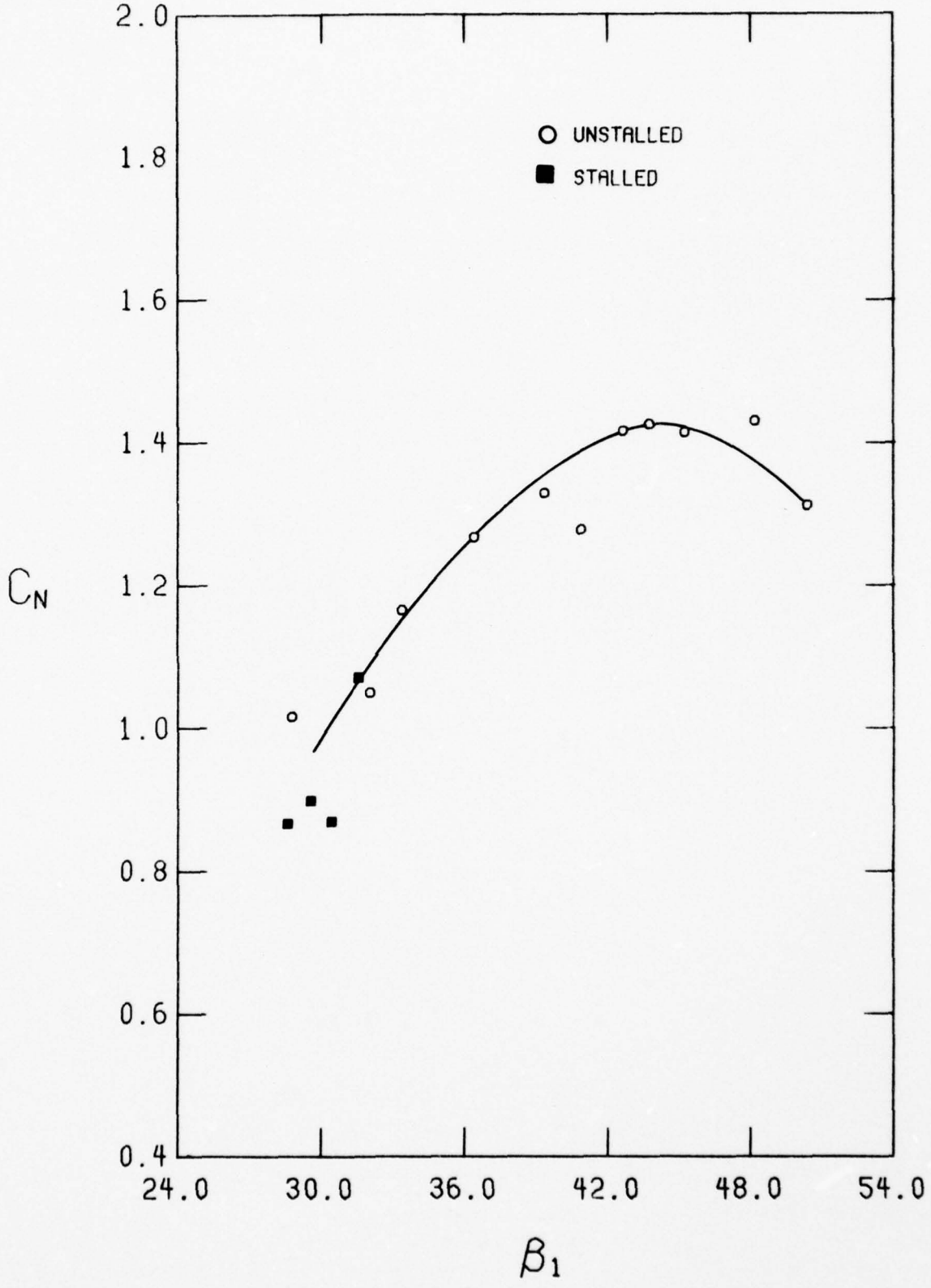

FIGURE 7. UNDISTORTED FLOW NORMAL FORCE COEFFICIENT AS A FUNCTION OF INLET ANGLE

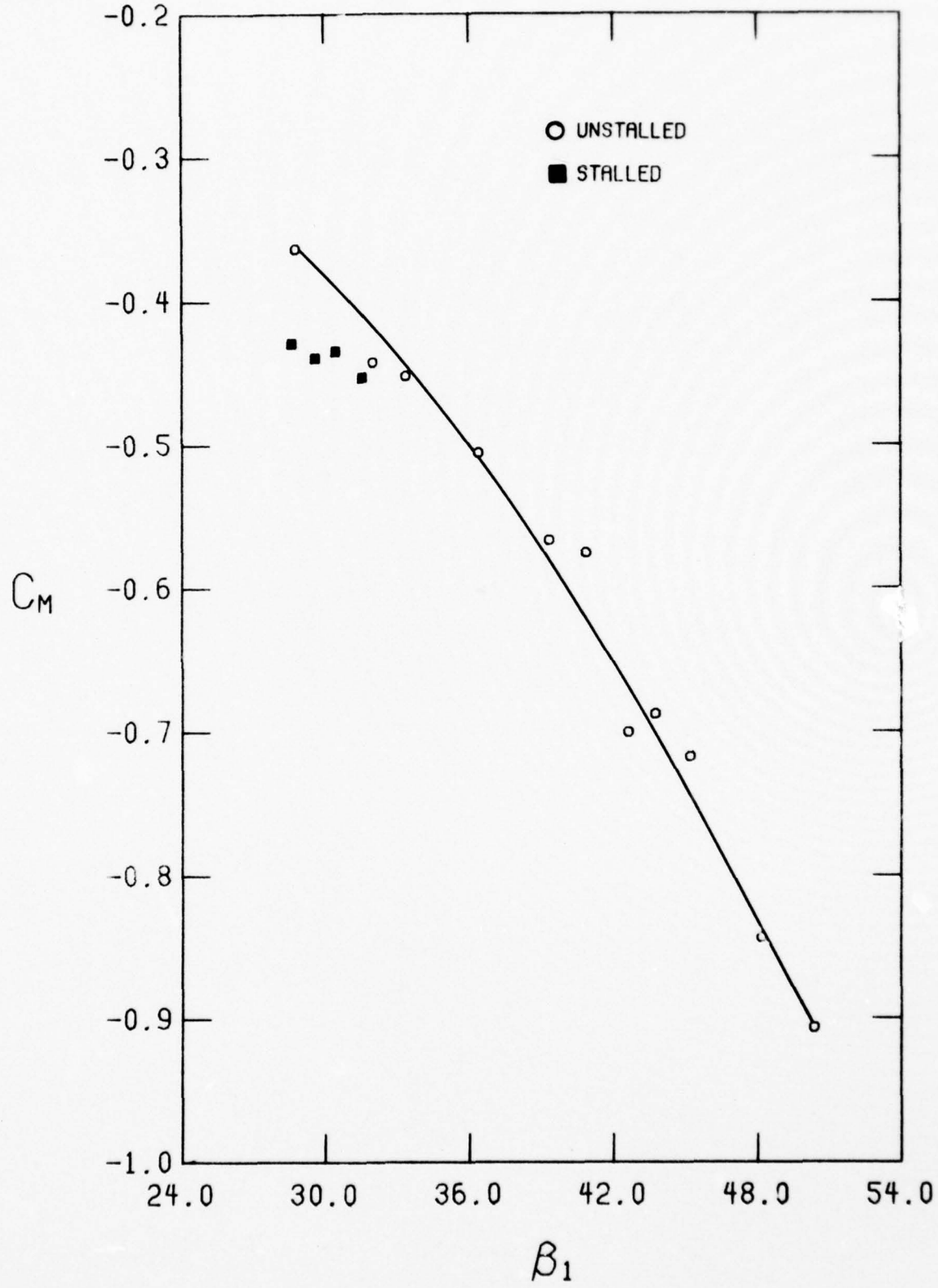

FIGURE 8. UNDISTORTED FLOW PITCHING MOMENT COEFFICIENT AS A FUNCTION OF INLET ANGLE

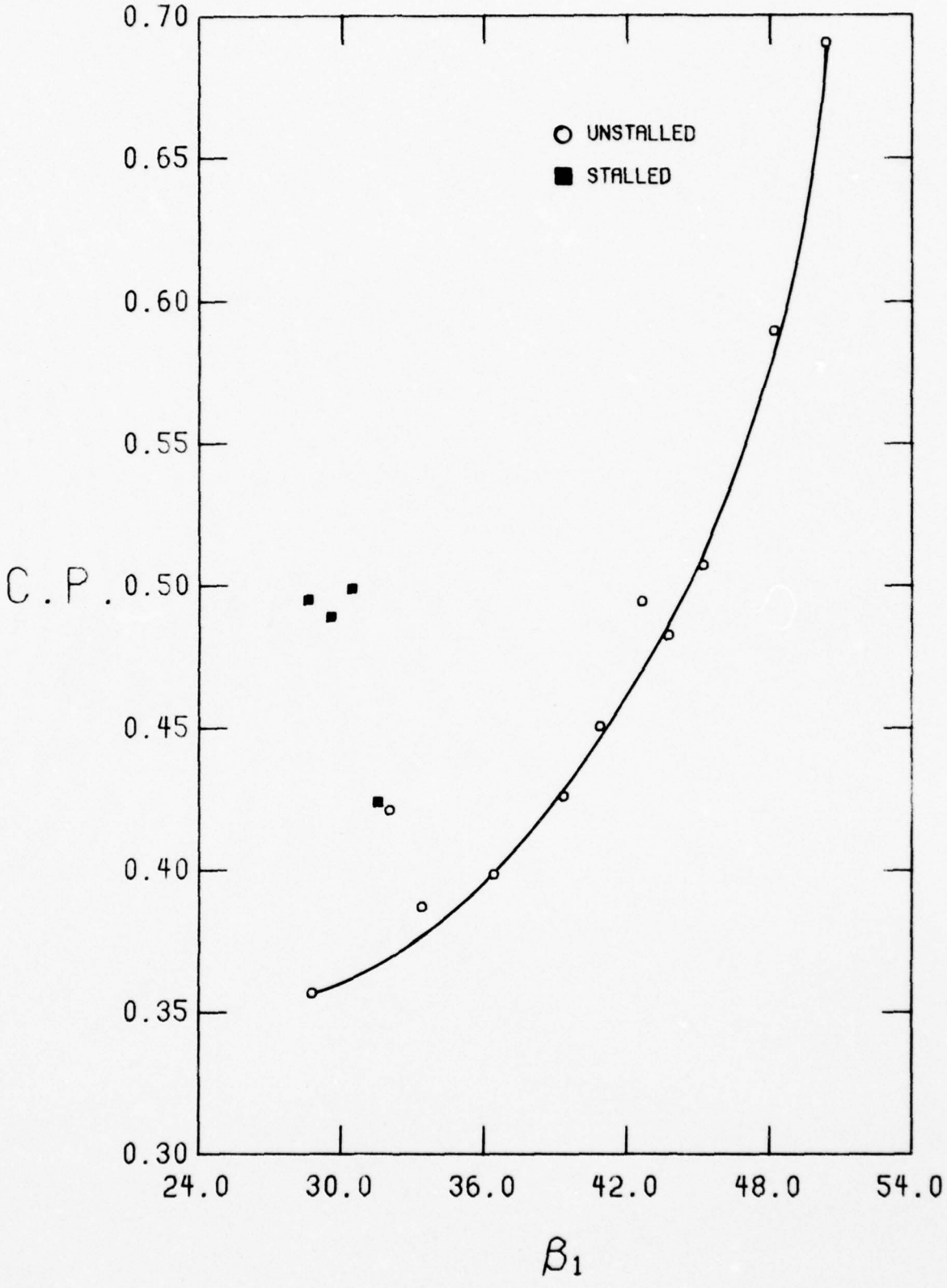

FIGURE 9. UNDISTORTED FLOW CENTER OF PRESSURE LOCATION AS A FUNCTION OF INLET ANGLE

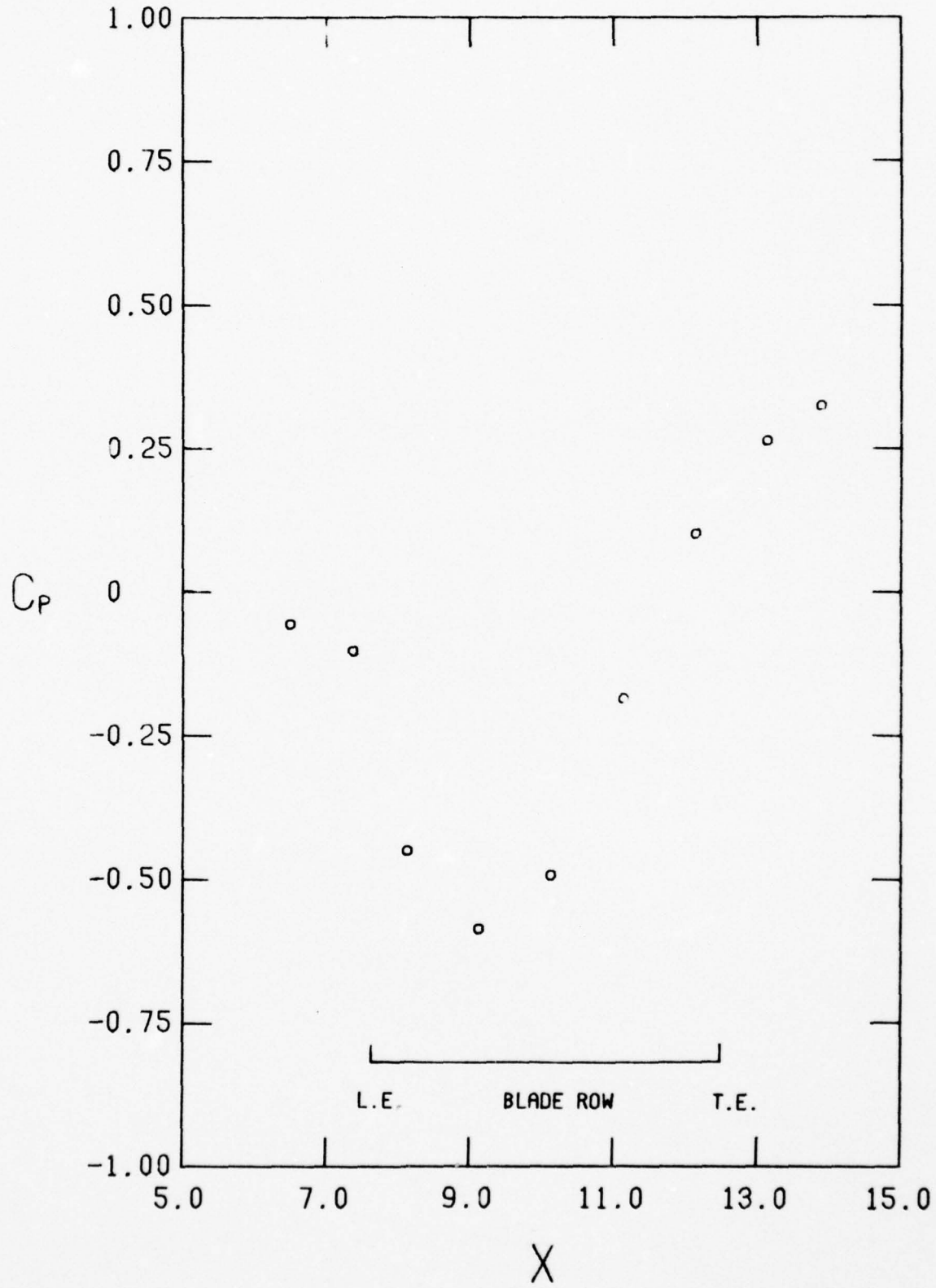

FIGURE 10. UNDISTORTED FLOW PRESSURE COEFFICIENT VARIATION ACROSS ROTOR

A. $C_x/U = 1.207$

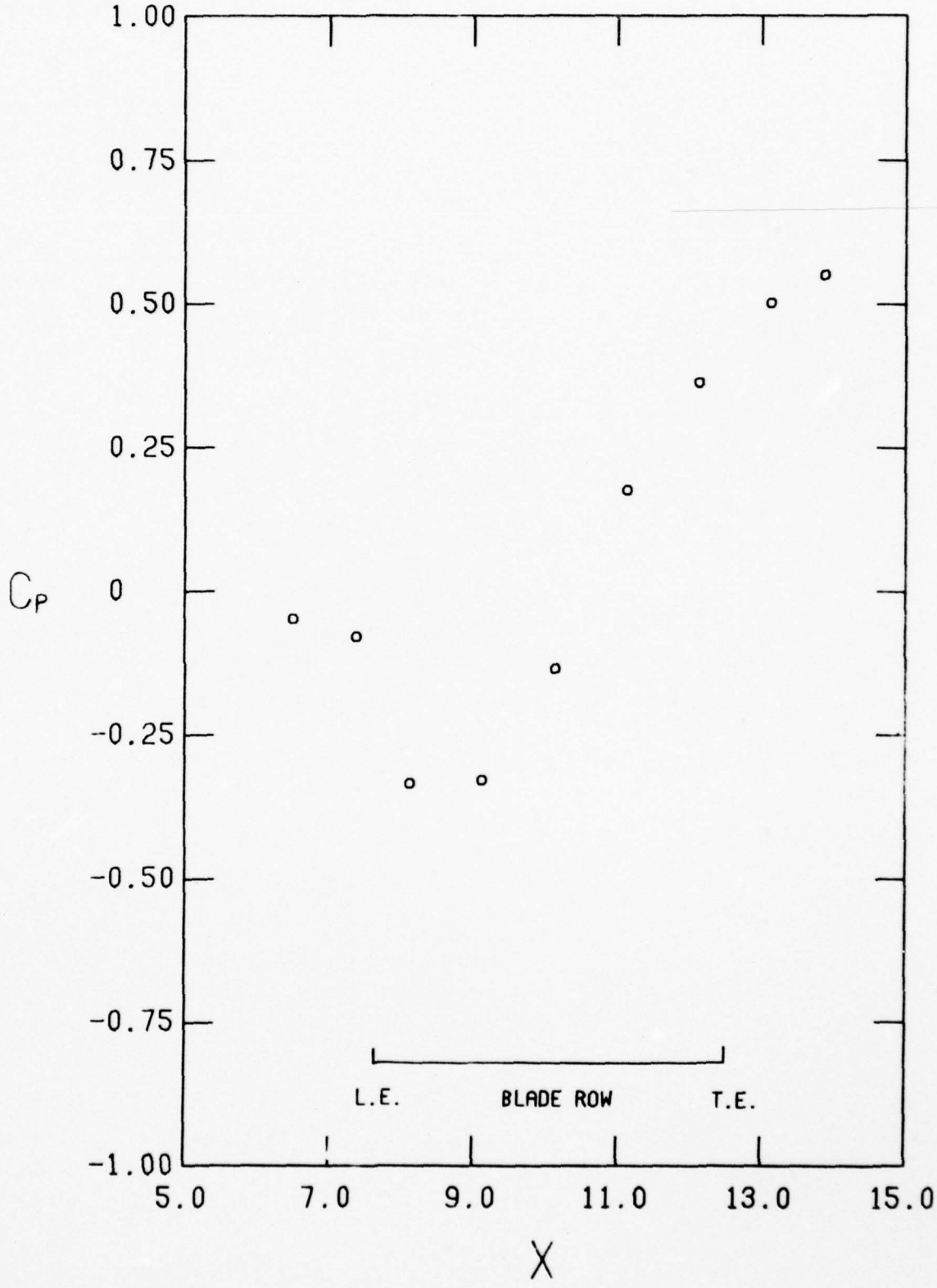

FIGURE 10. CONTINUED
B. $C_X/U = 1.117$

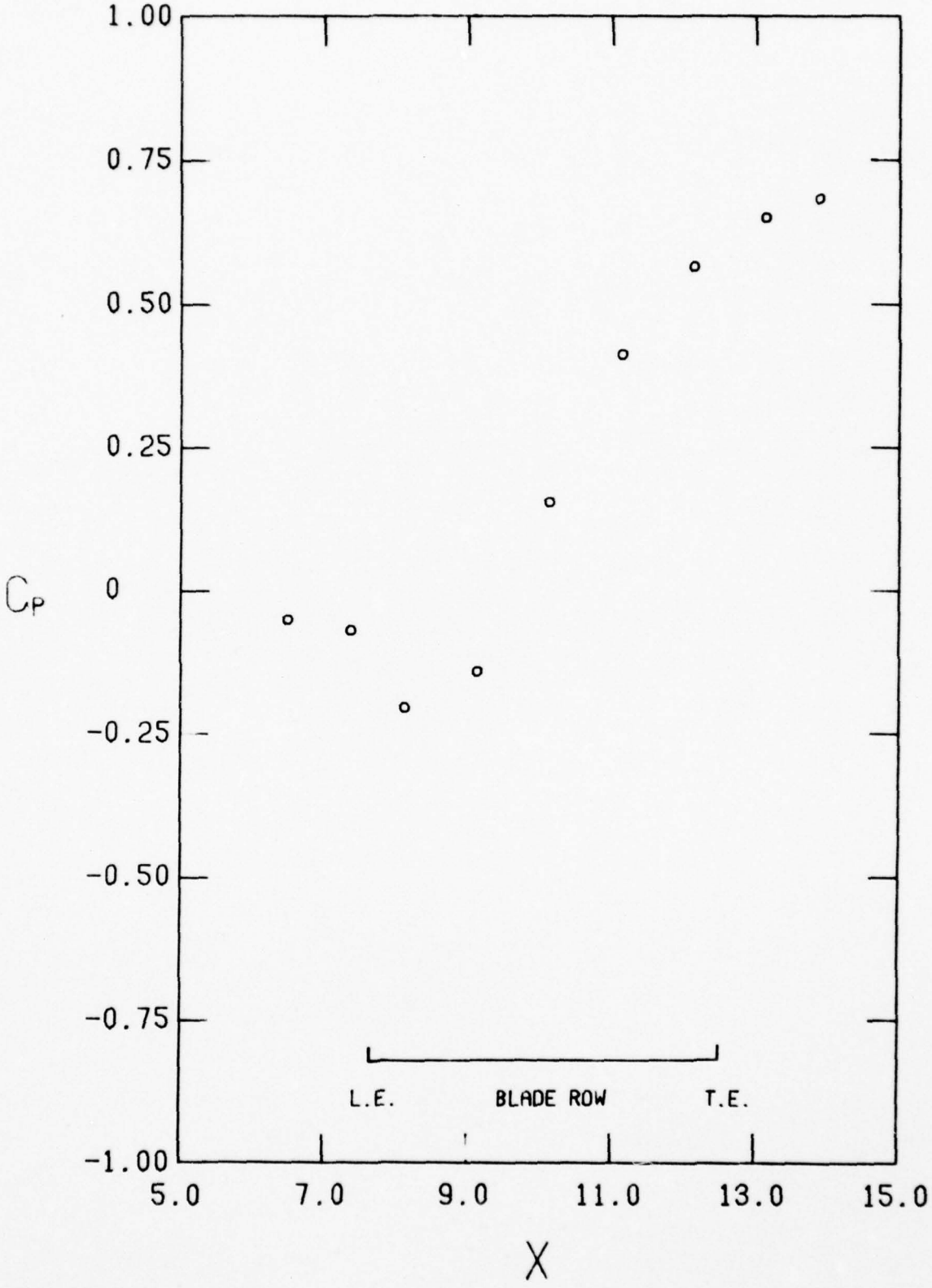

FIGURE 10. CONTINUED
c. $C_X/U = 1.007$

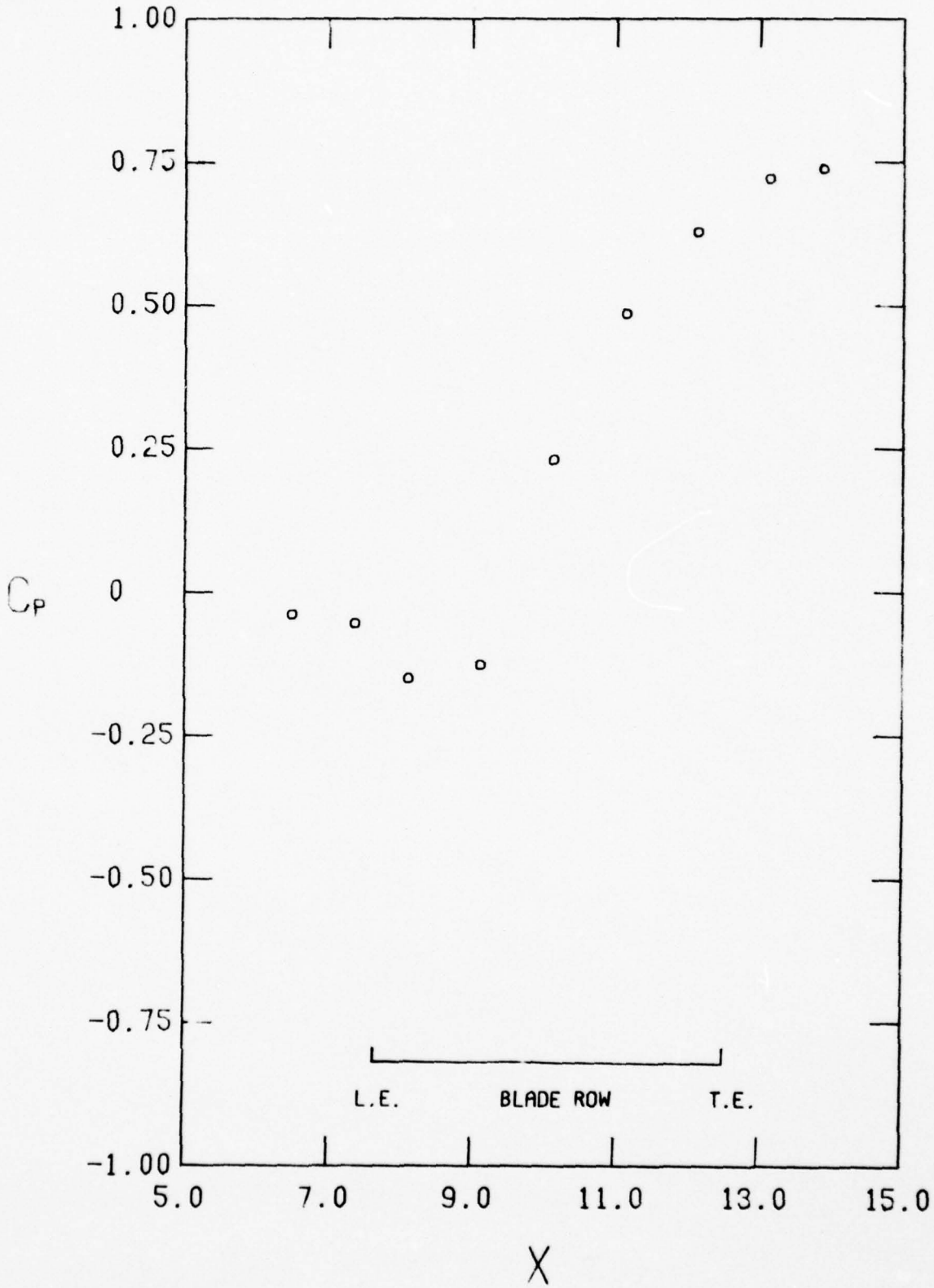

FIGURE 10. CONTINUED
D. $C_X/U = 0.957$

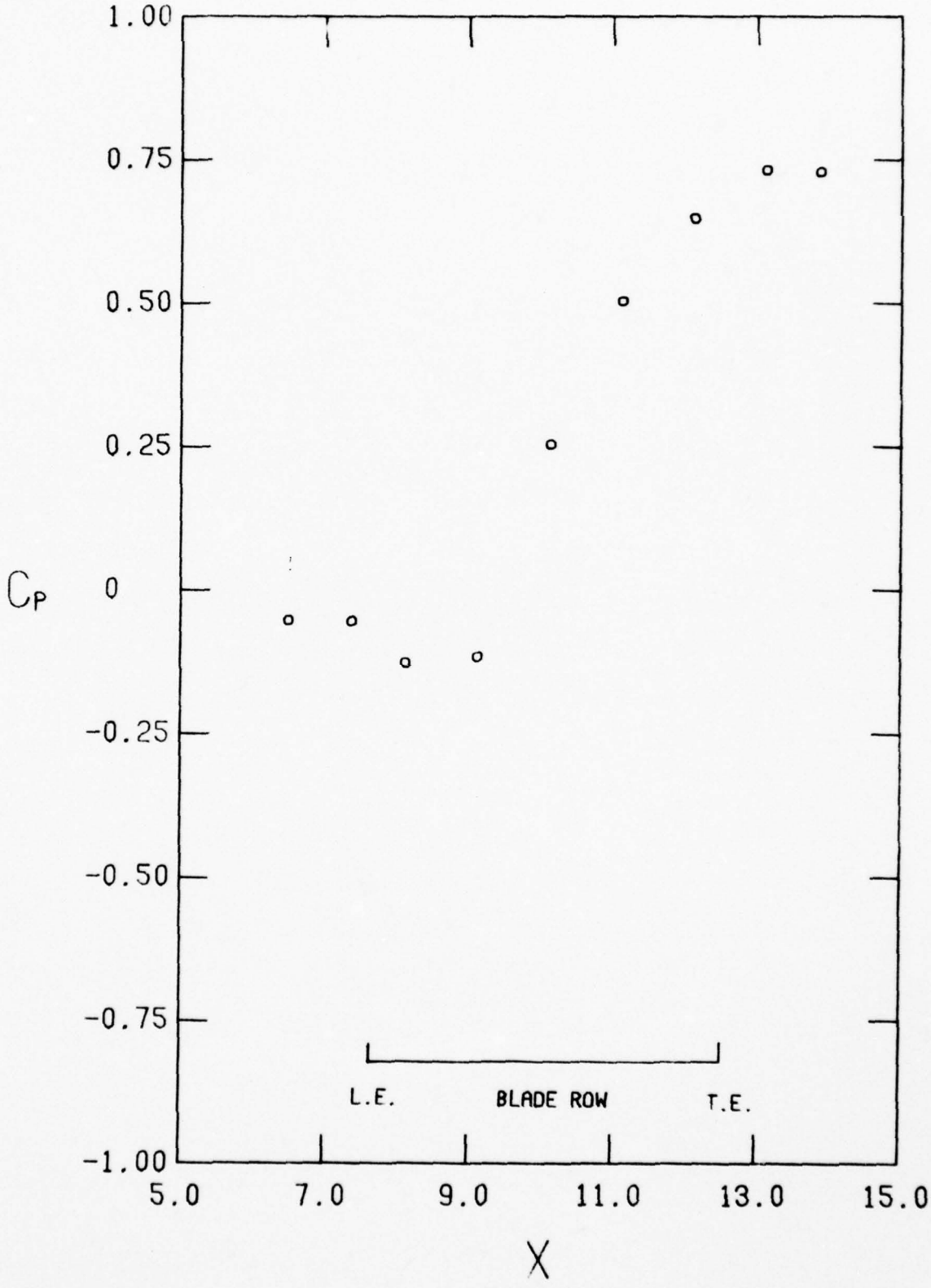

FIGURE 10. CONTINUED
E. $C_X/U = 0.920$

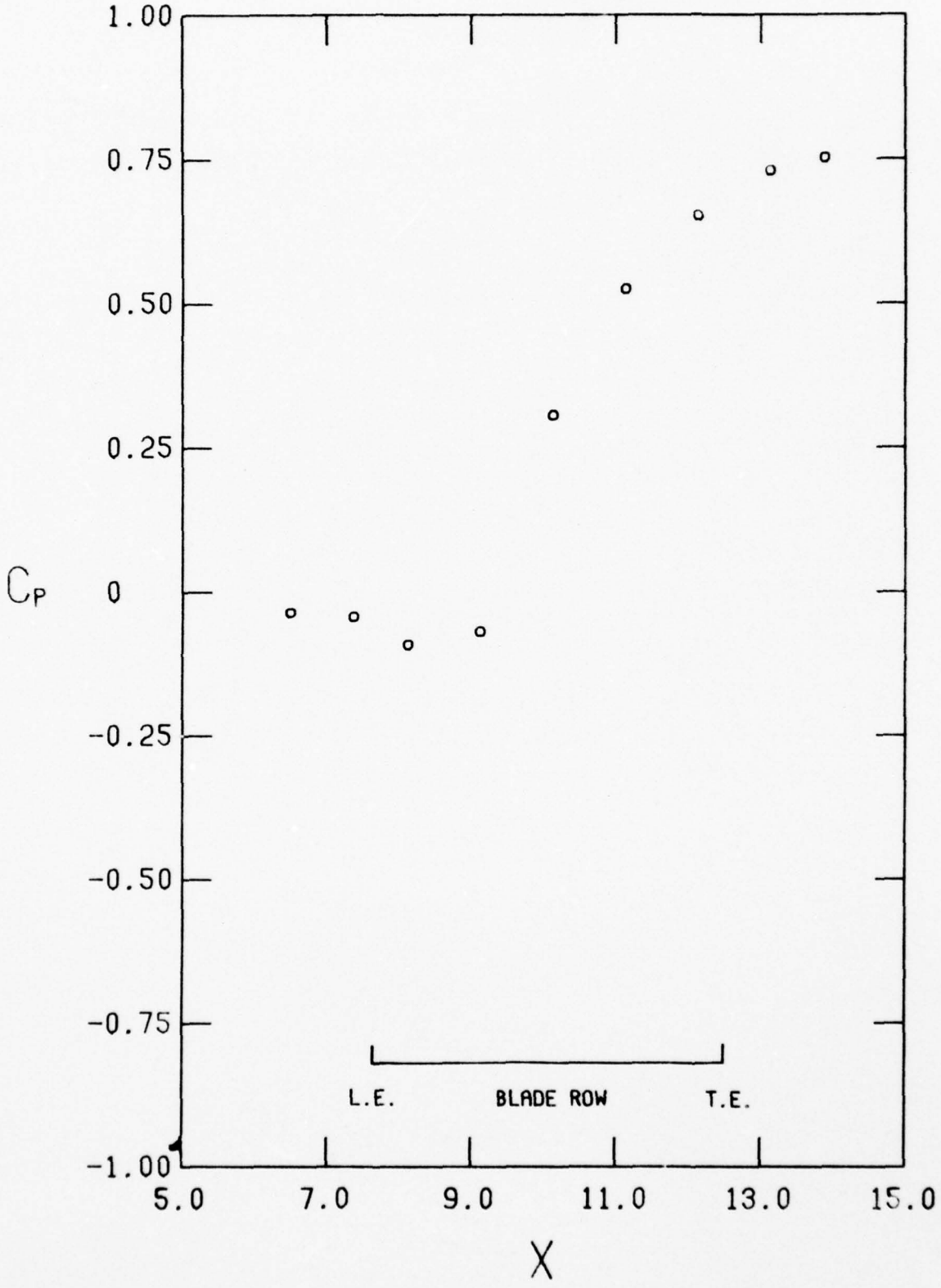

FIGURE 10. CONTINUED
F. $C_X/U = 0.865$

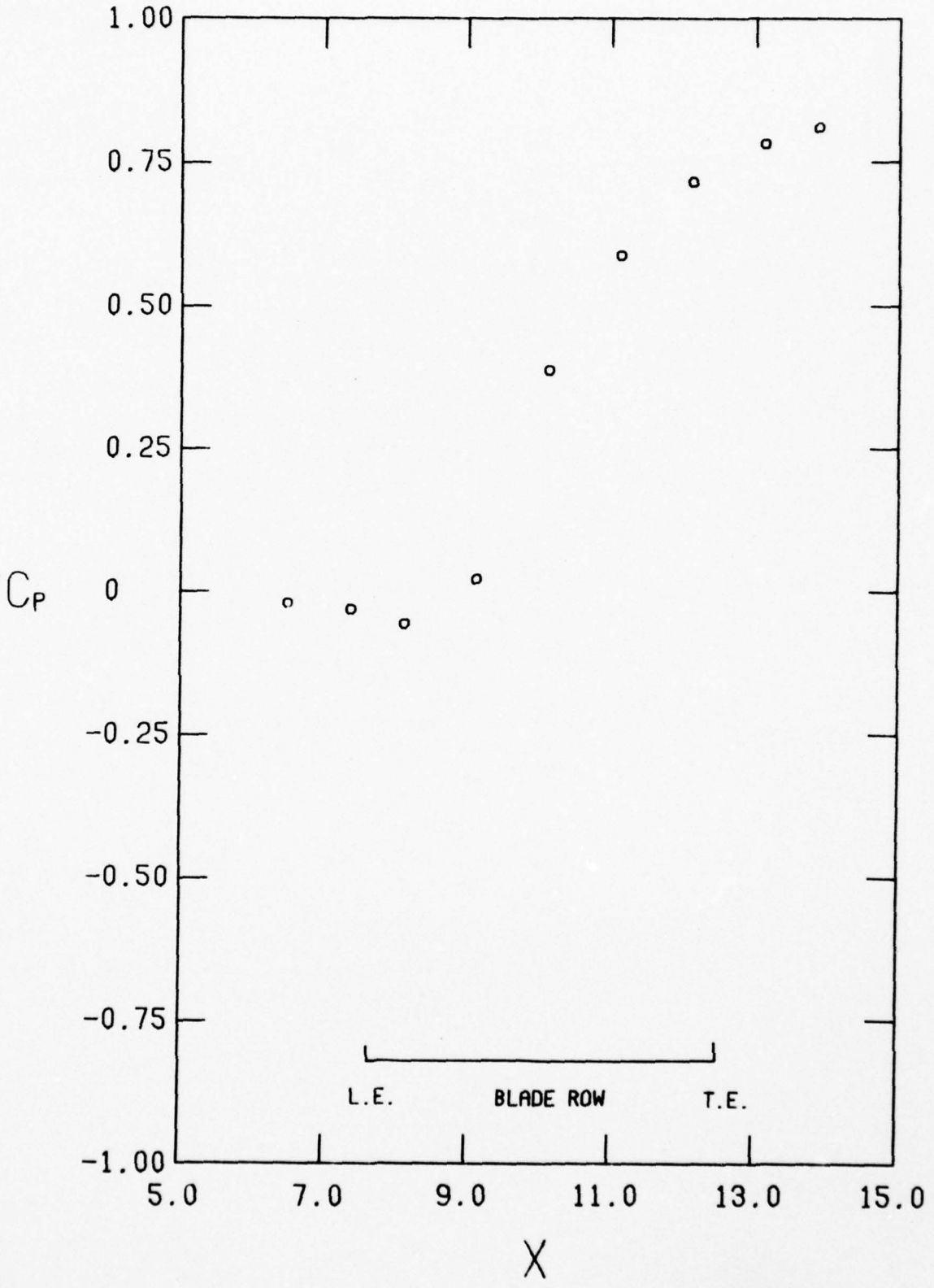

FIGURE 10. CONTINUED
G. $C_X/U = 0.819$

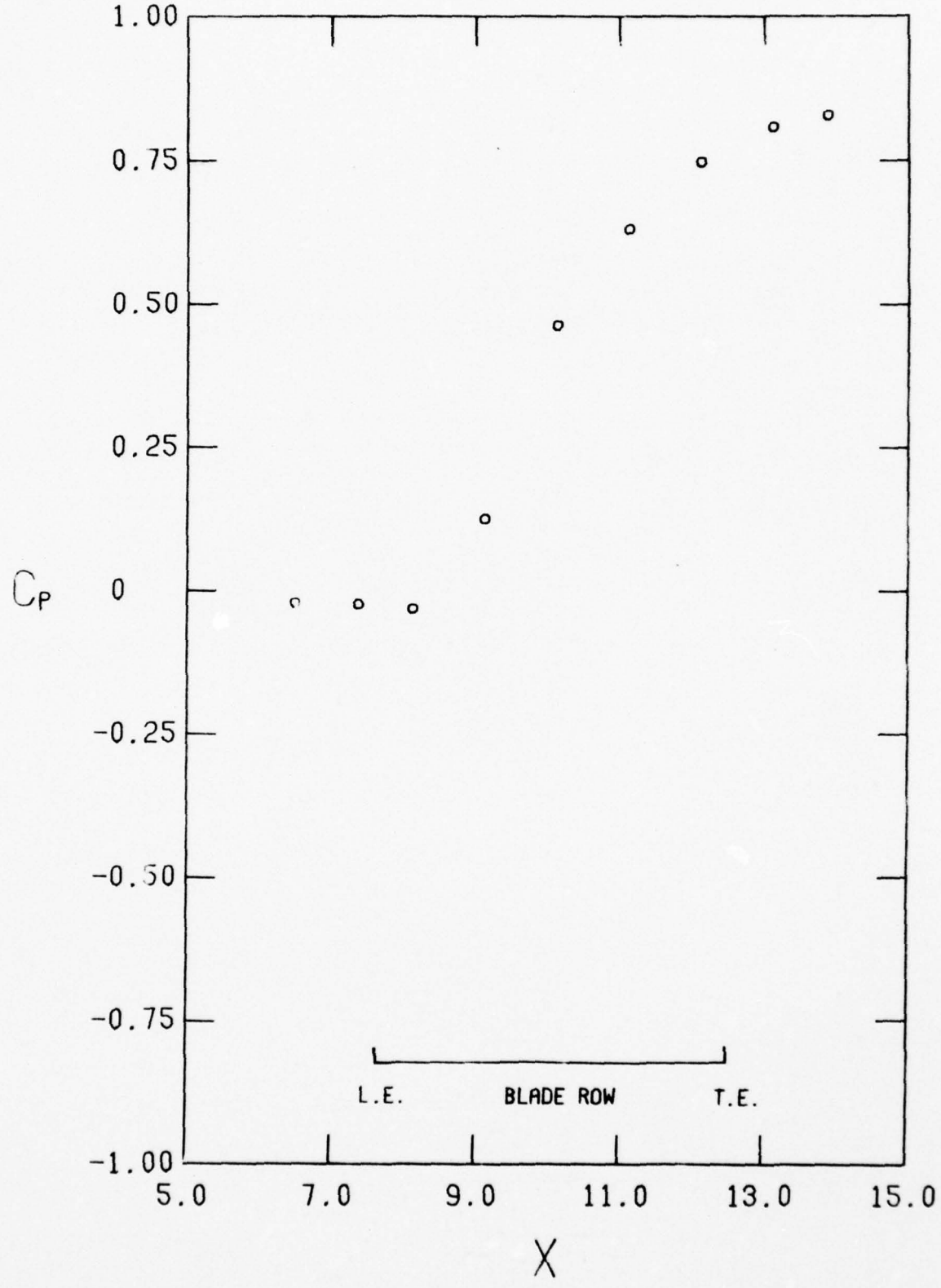

FIGURE 10. CONTINUED
H. $C_X/U = 0.737$

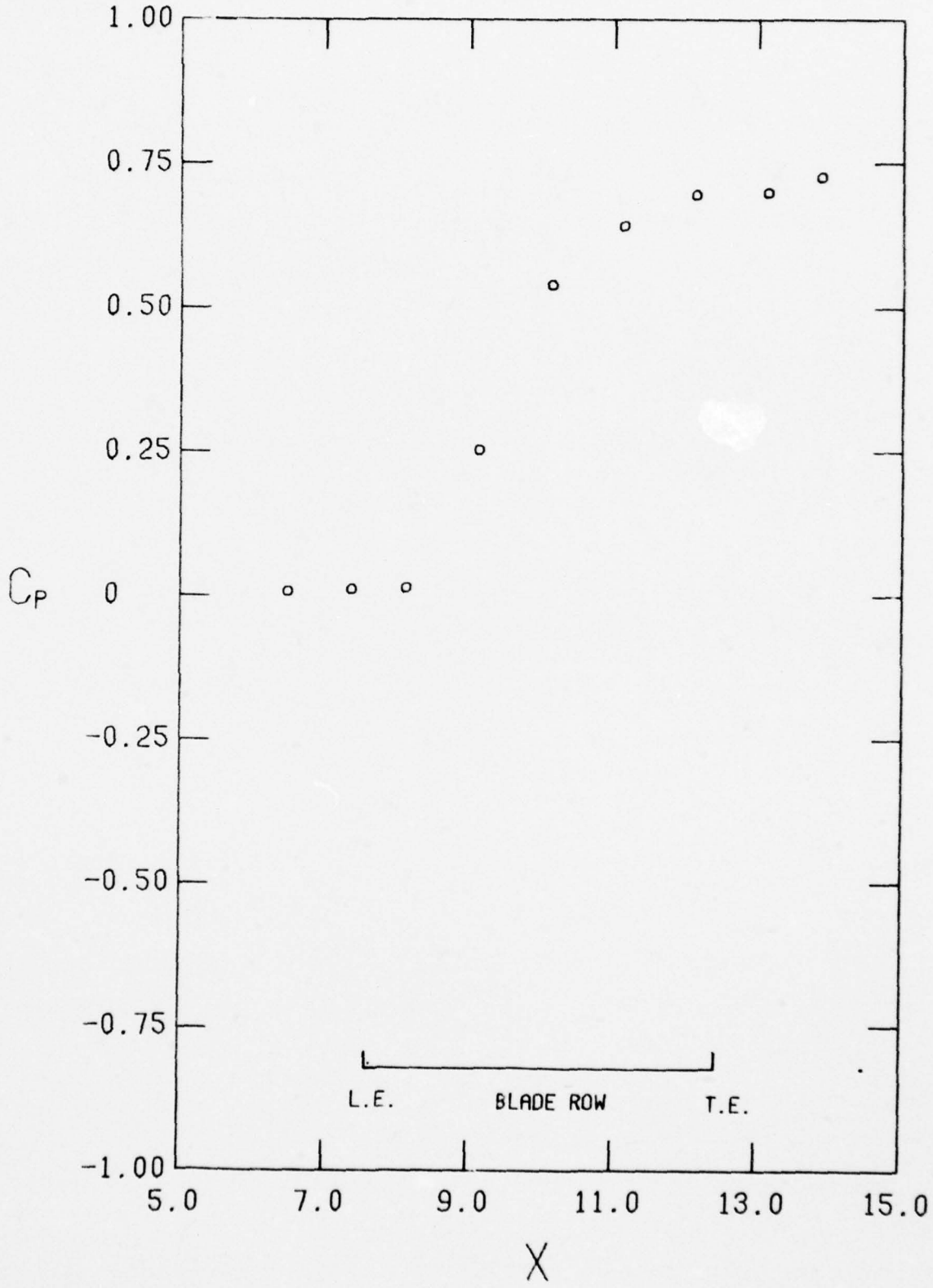

FIGURE 10. CONTINUED
I. $C_X/U = 0.658$

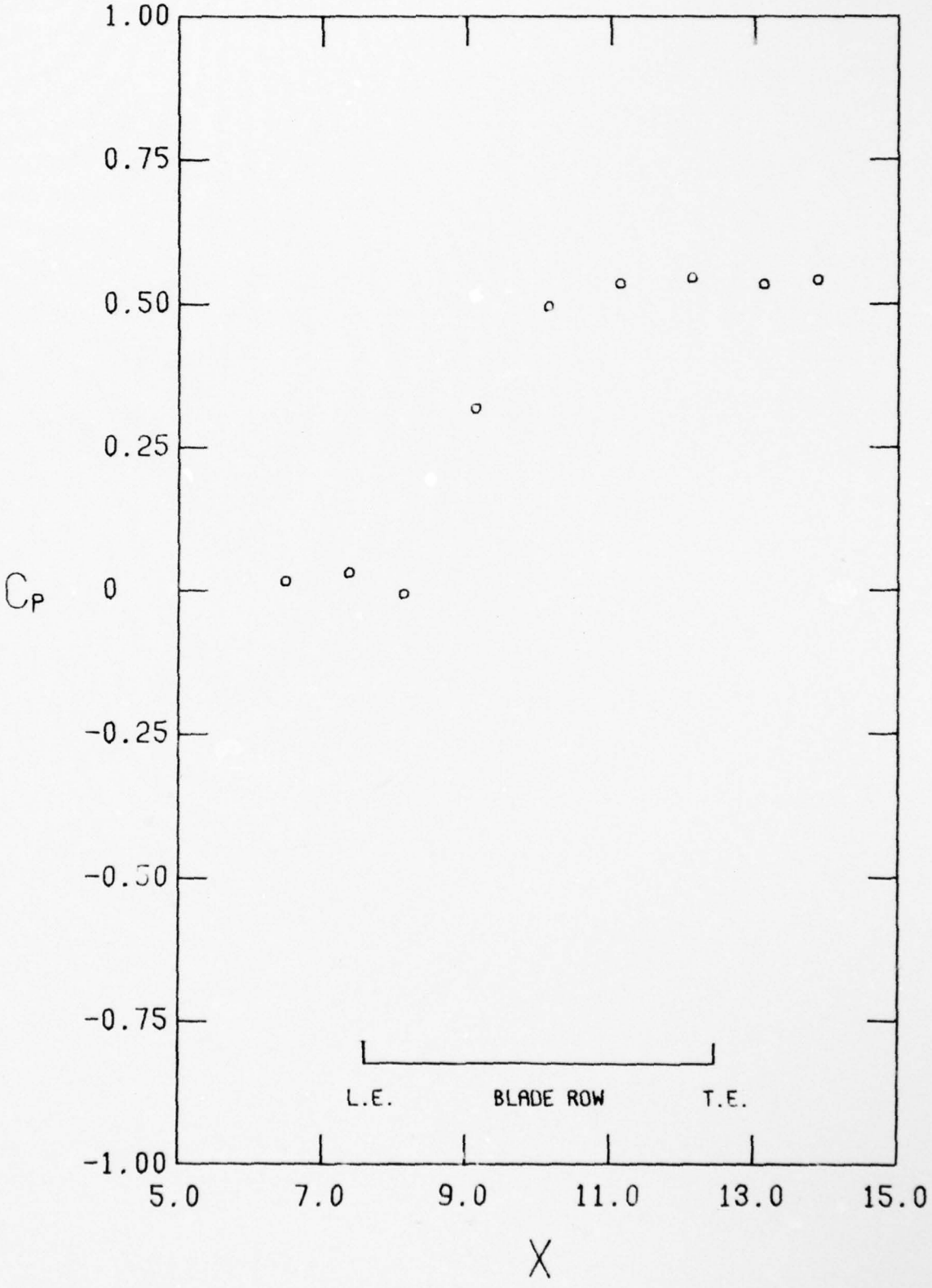

FIGURE 10. CONTINUED
J. $C_X/U = 0.549$

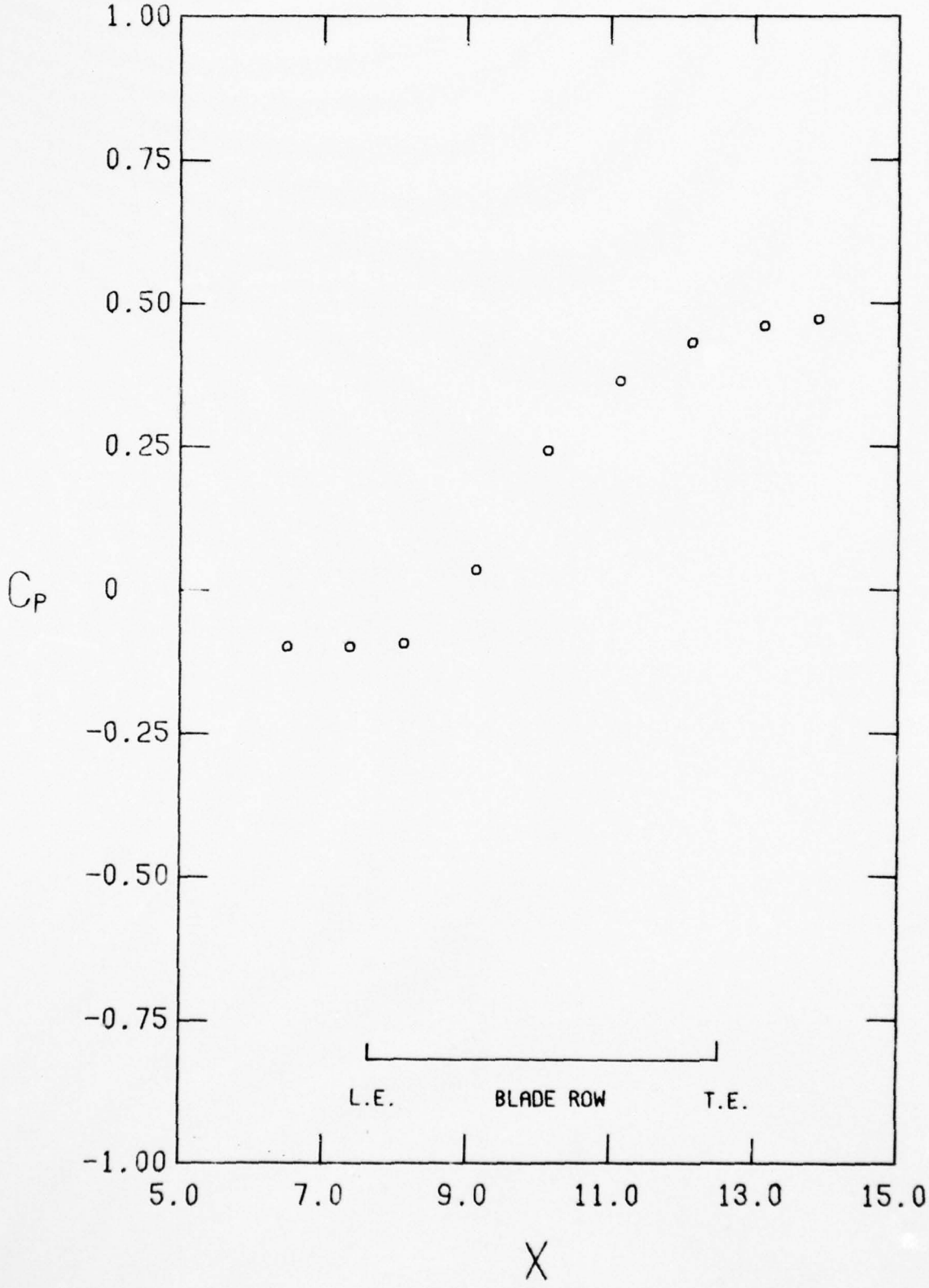

FIGURE 10. CONTINUED
K. $C_X/U = 0.546$ (STALL INCEPTION)

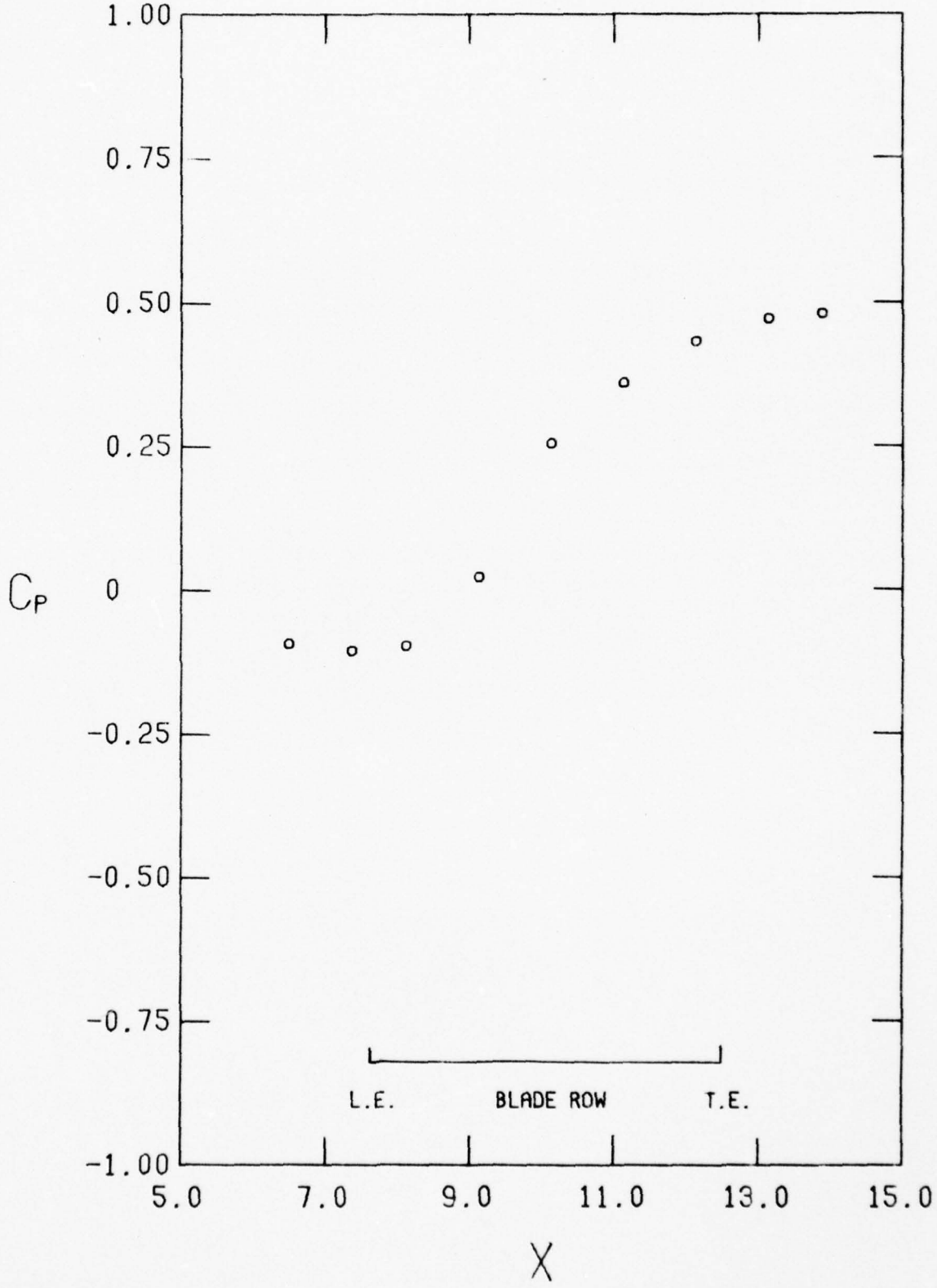

FIGURE 10. CONTINUED
L. $C_X/U = 0.568$ (STALLED)

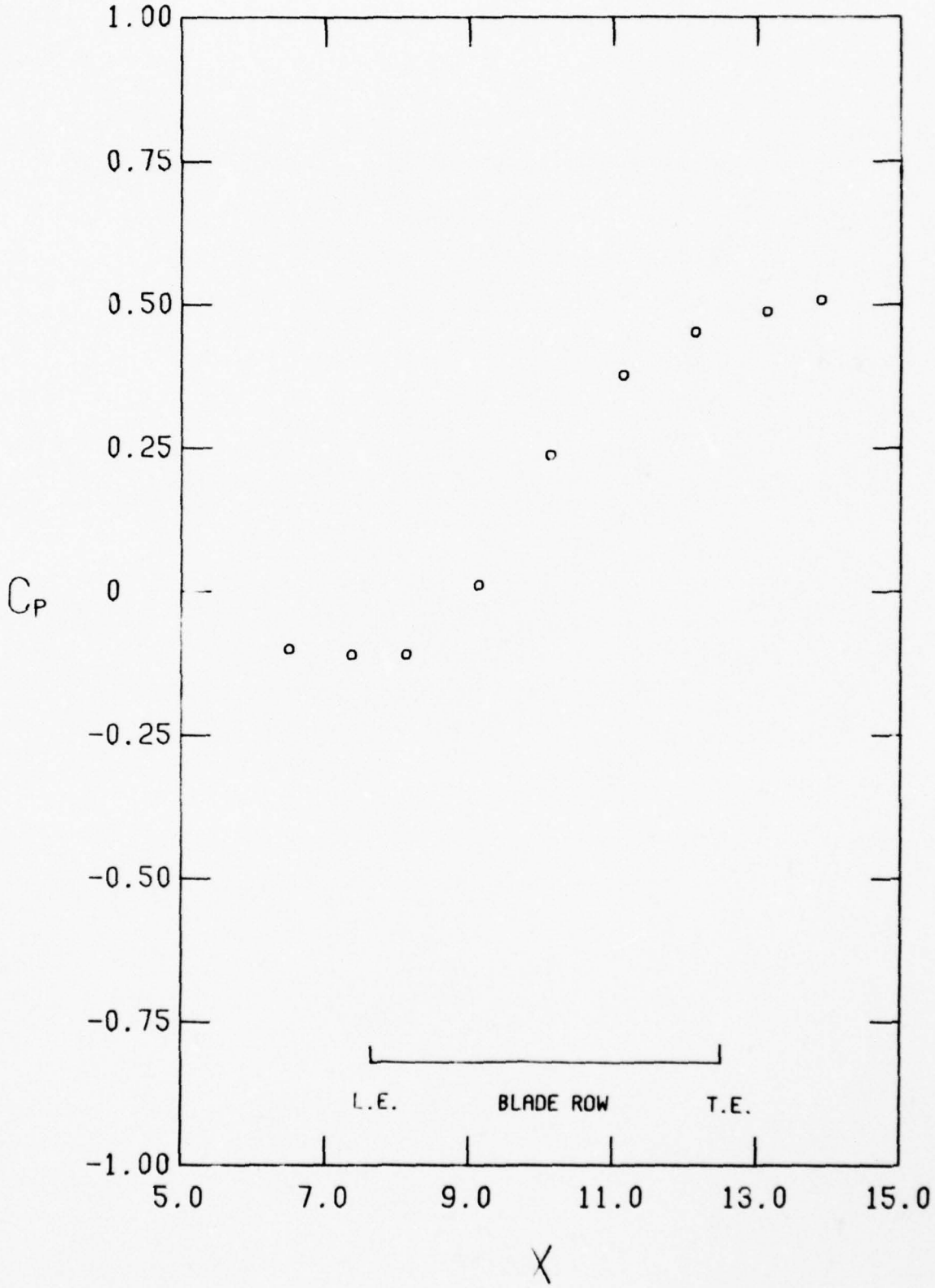

FIGURE 10. CONTINUED
M. $C_X/U = 0.588$ (STALLED)

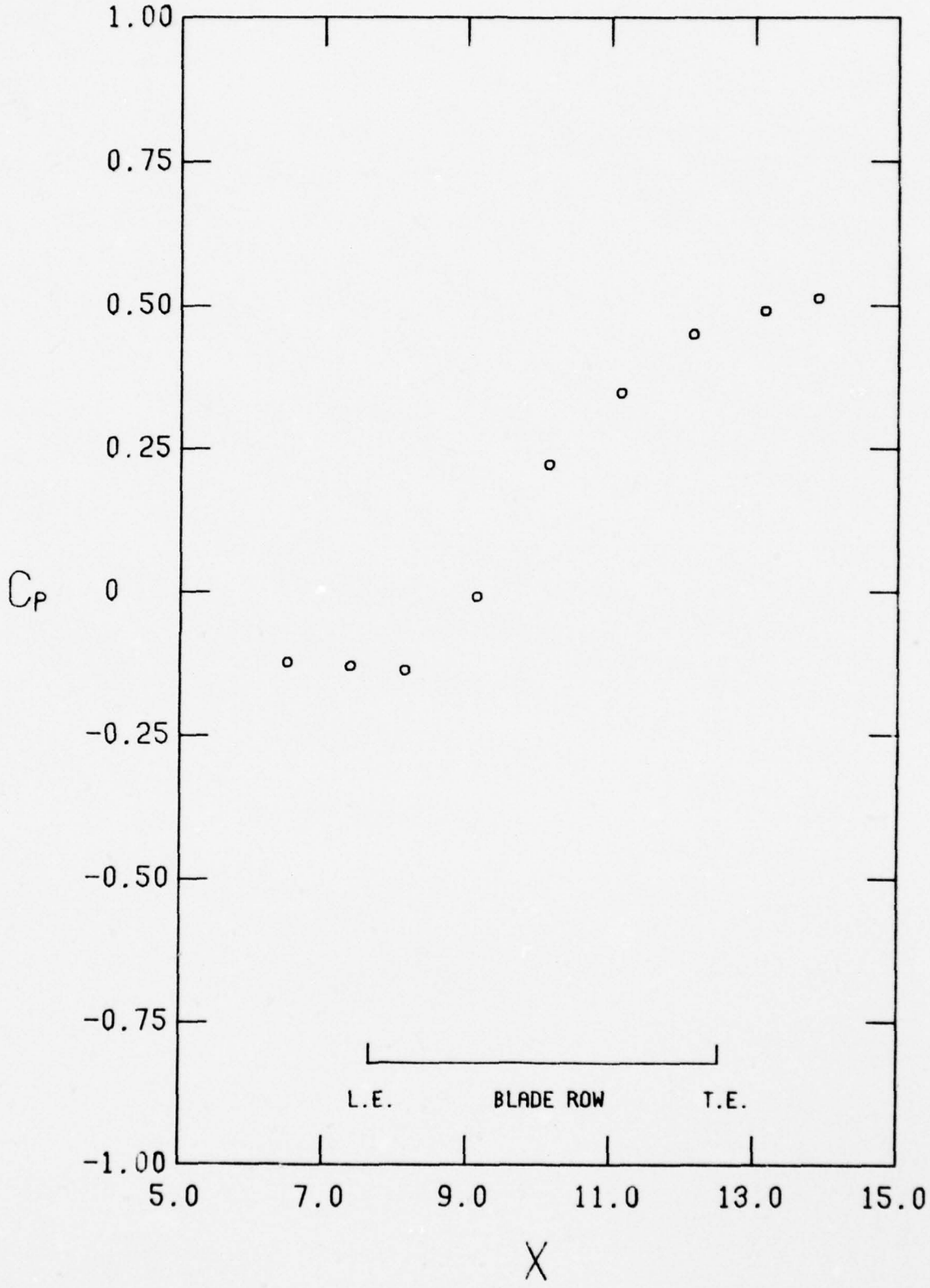

FIGURE 10. CONTINUED
N. $C_X/U = 0.614$ (STALLED)

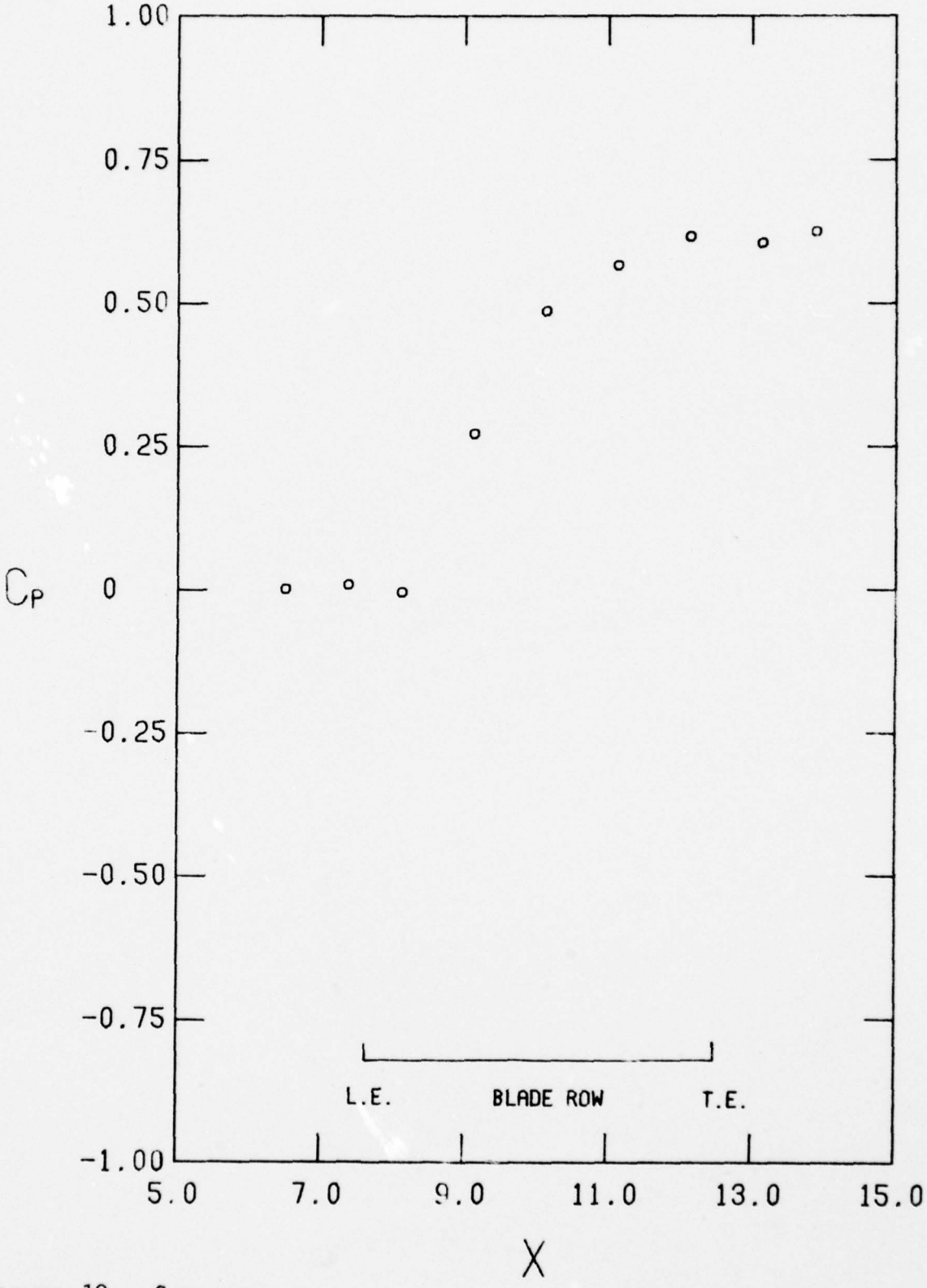

FIGURE 10. CONCLUDED

o. $C_X/U = 0.625$ (RECOVERY FROM STALL)

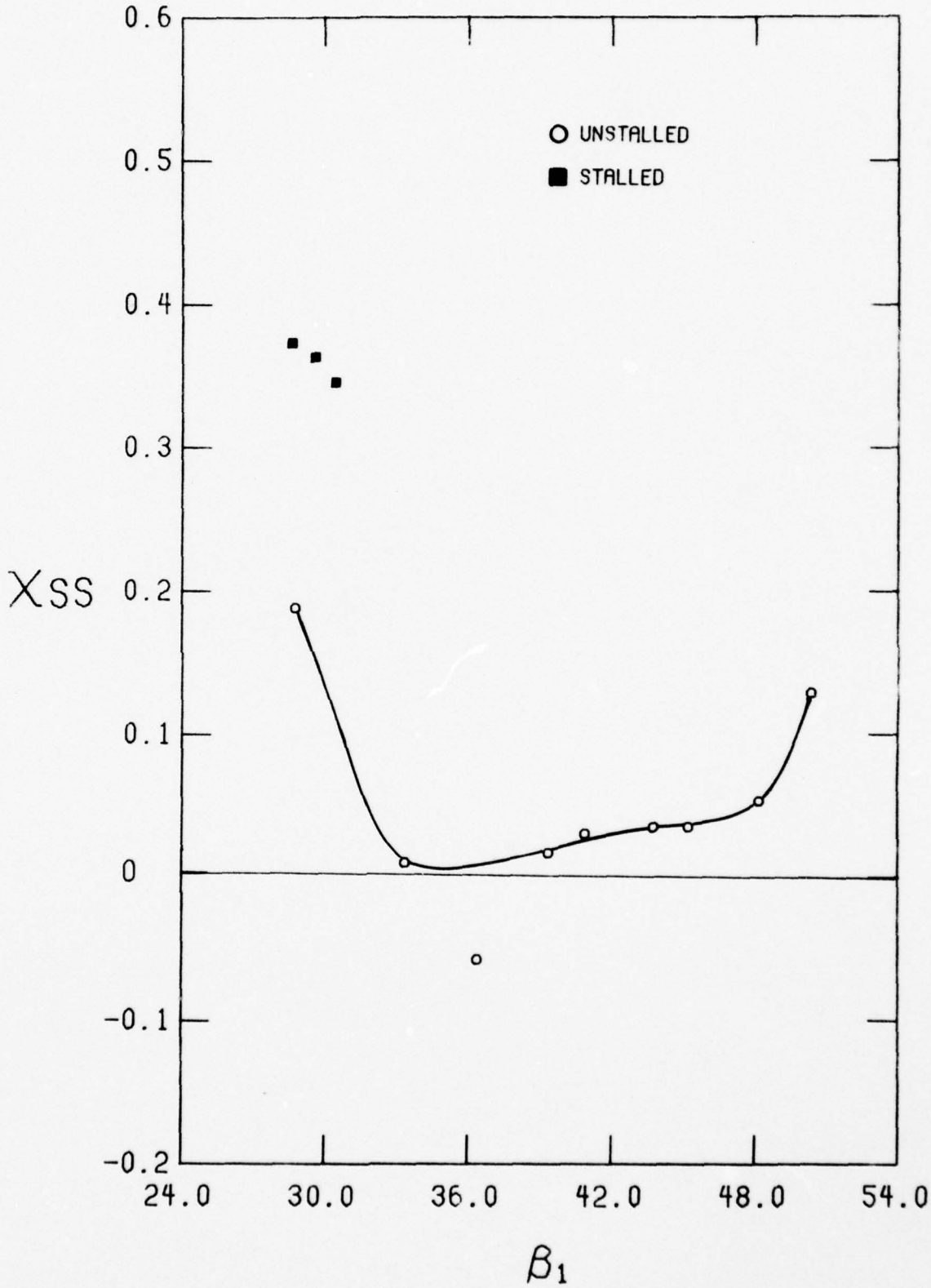

FIGURE 11. UNDISTORTED FLOW LOSS COEFFICIENT AS A FUNCTION OF INLET ANGLE

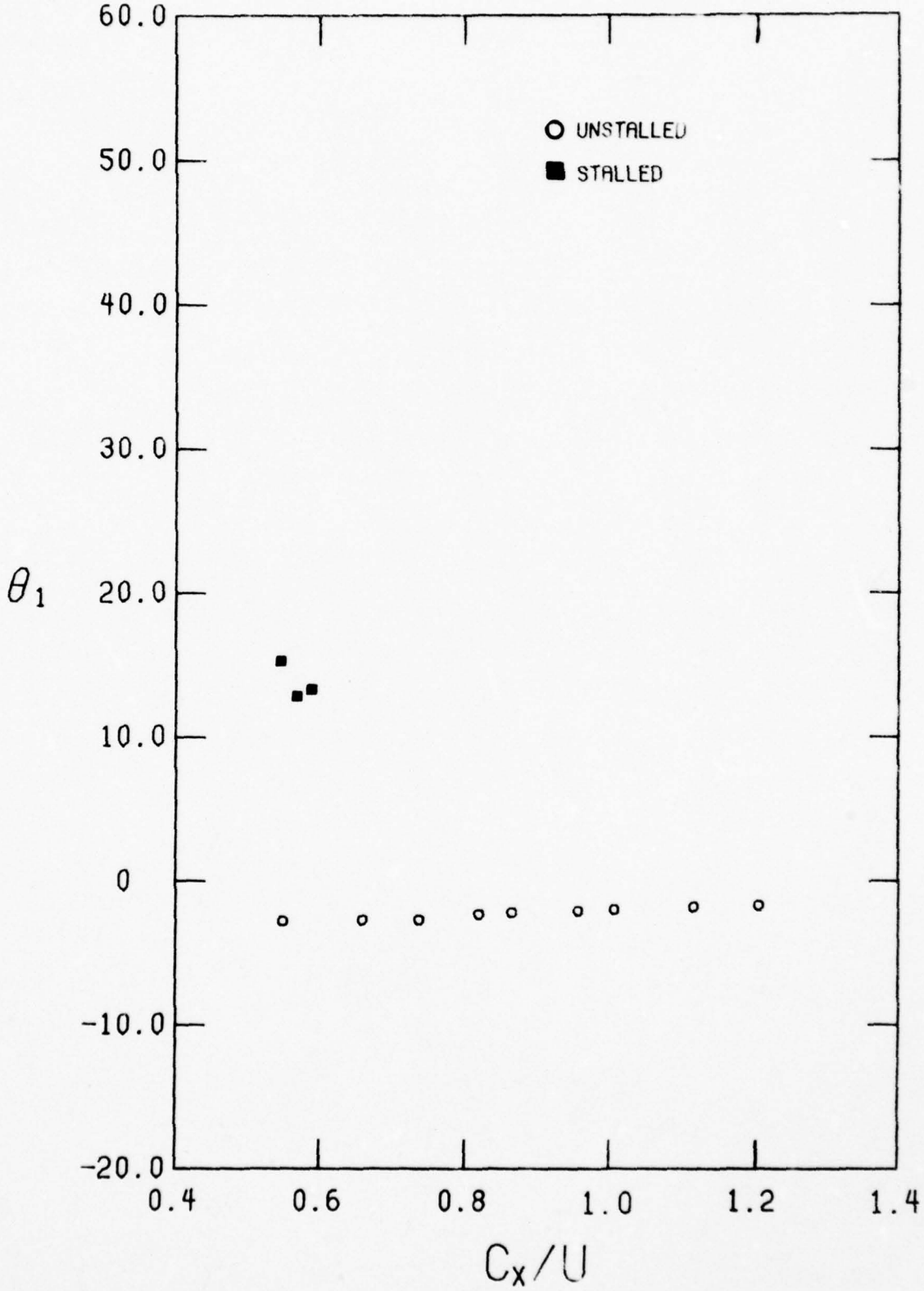

FIGURE 12. UNDISTORTED FLOW STATIONARY REFERENCE FRAME FLOW ANGLES

A. ROTOR ENTRANCE ANGLE

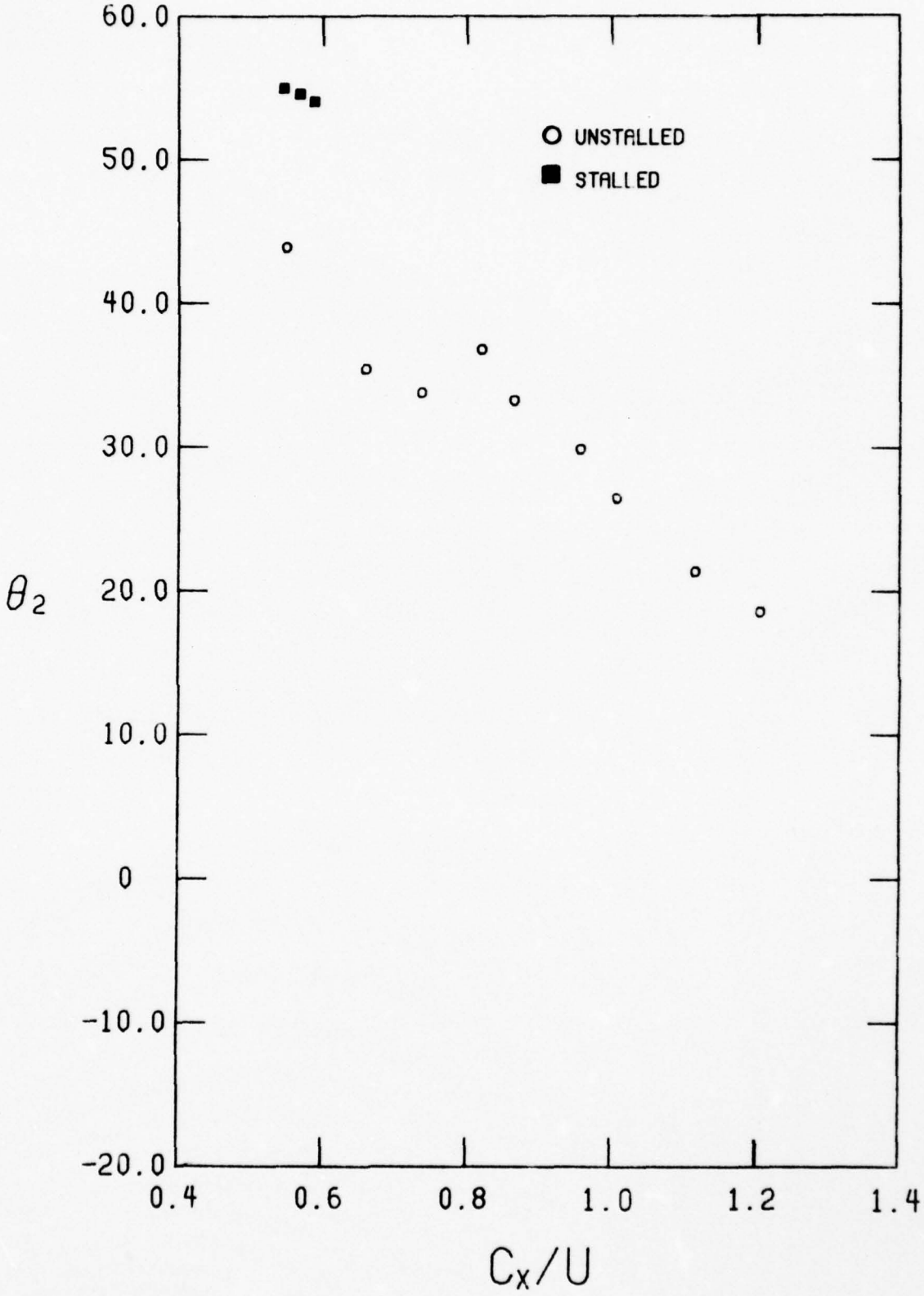

FIGURE 12. CONCLUDED

B. ROTOR EXIT ANGLE

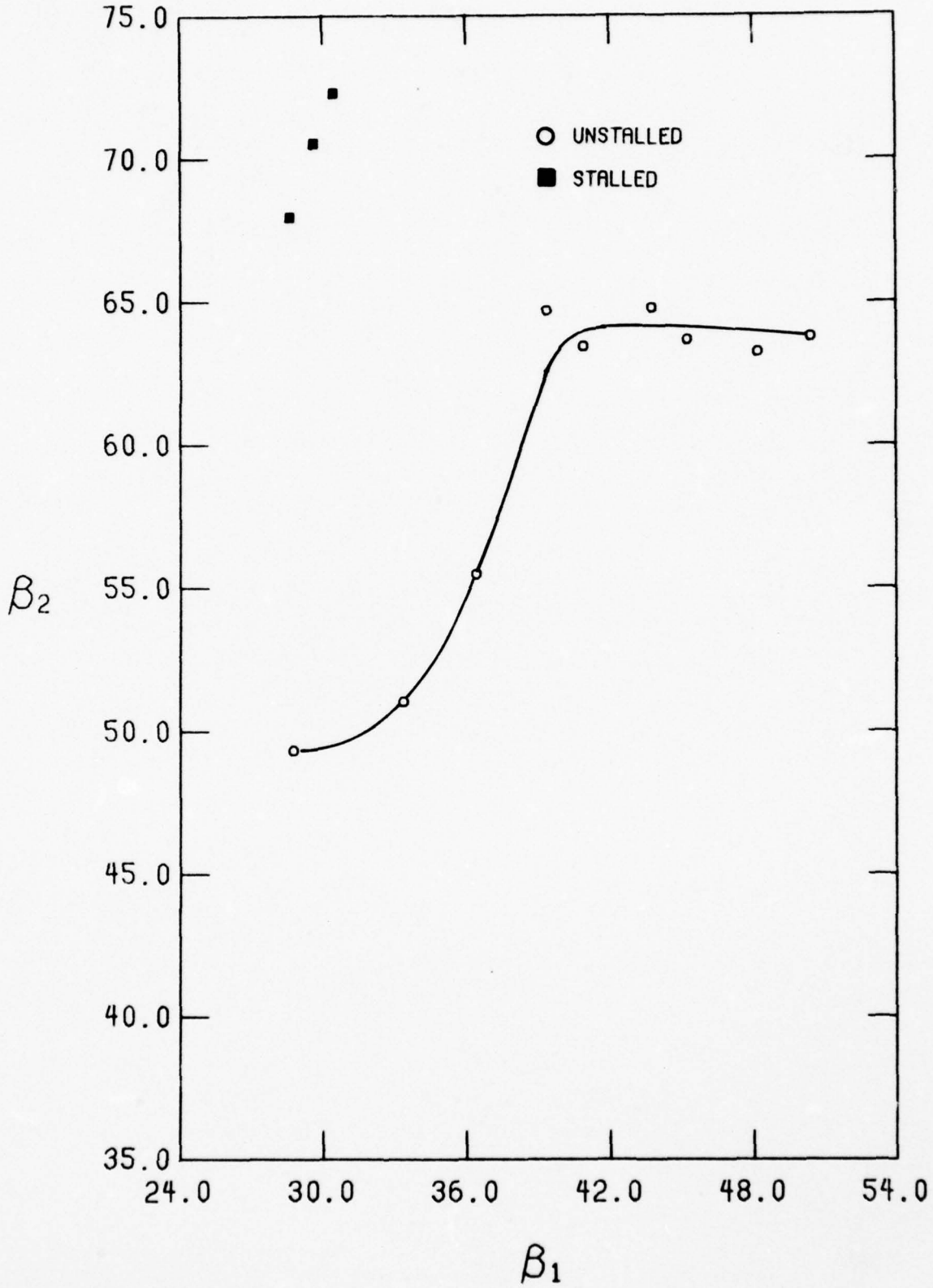

FIGURE 13. UNDISTORTED FLOW EXIT ANGLE AS A FUNCTION OF INLET ANGLE

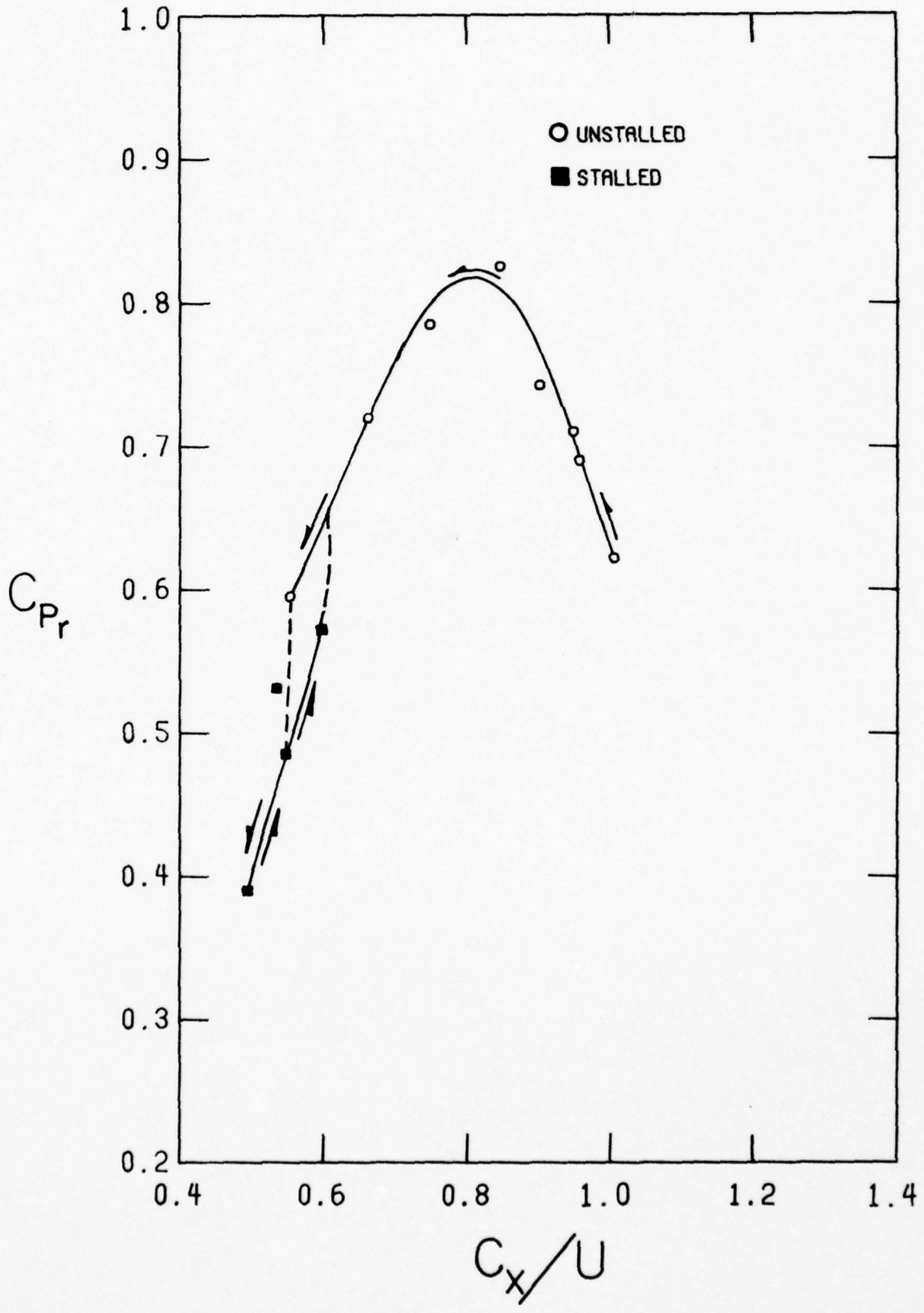

FIGURE 14. DISTORTED FLOW ROTOR PRESSURE RISE

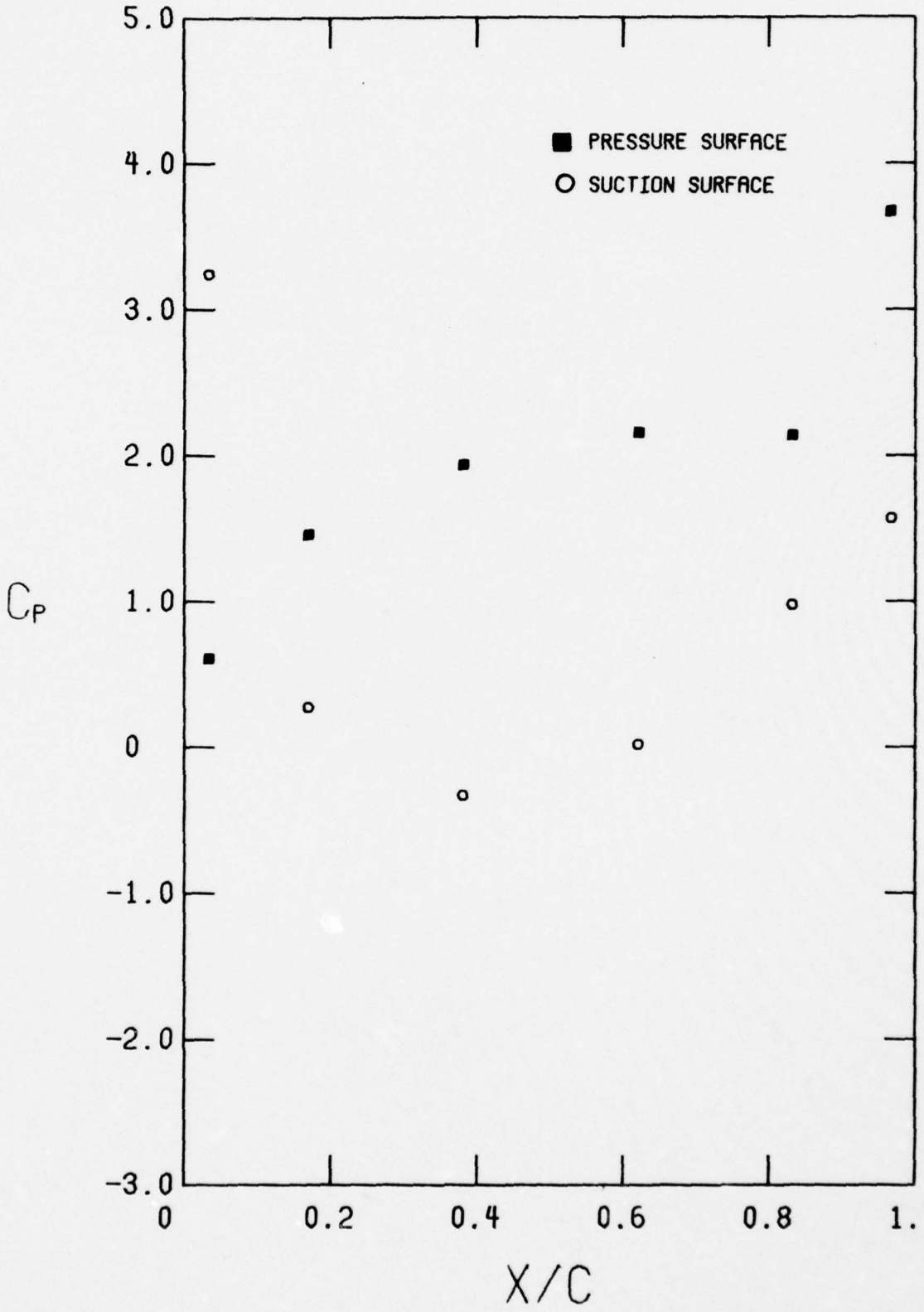

FIGURE 15. DISTORTED FLOW BLADE PRESSURE DISTRIBUTIONS
A. $C_X/U = 1.005$

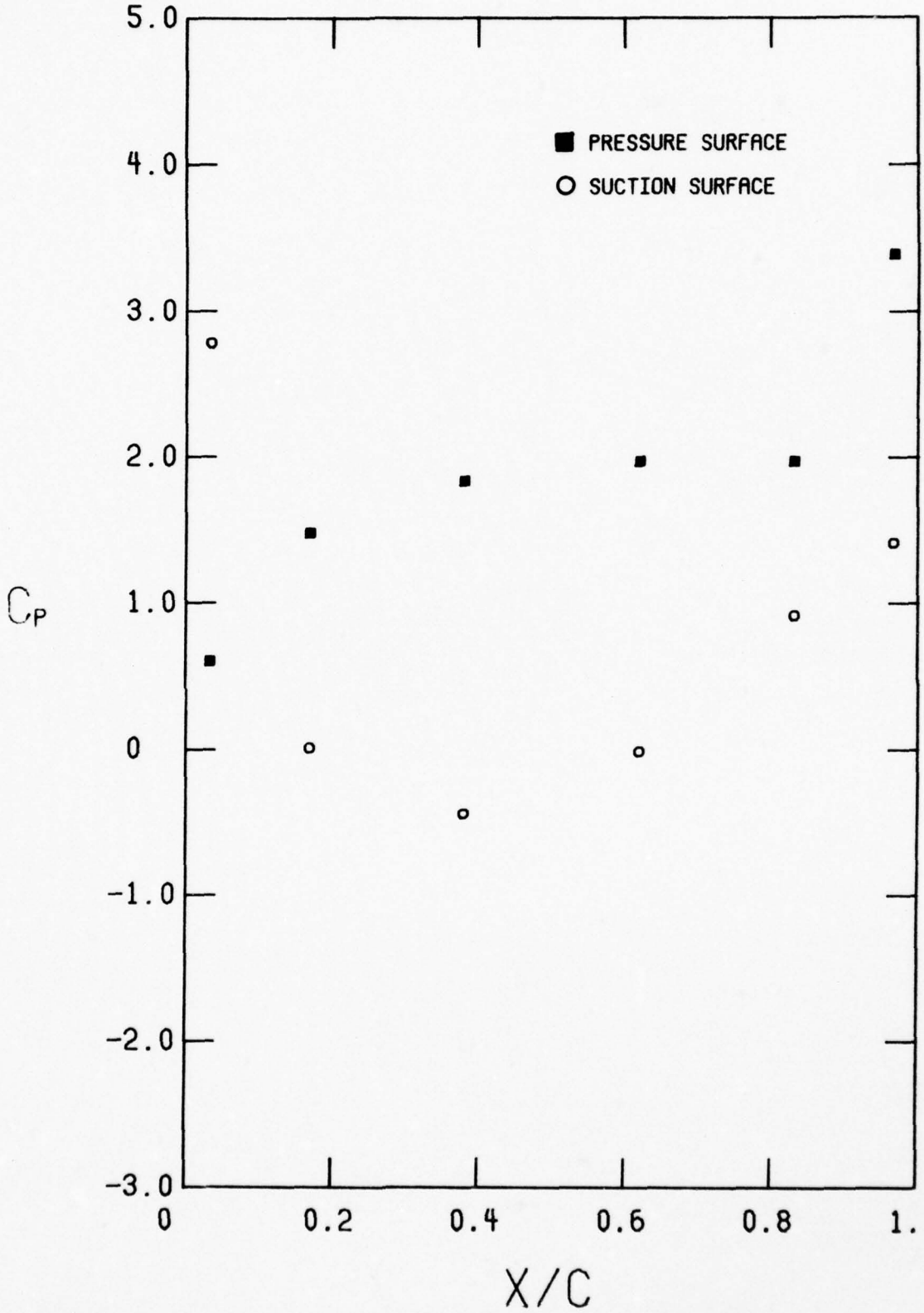

FIGURE 15. CONTINUED
B. $C_X/U = 0.956$

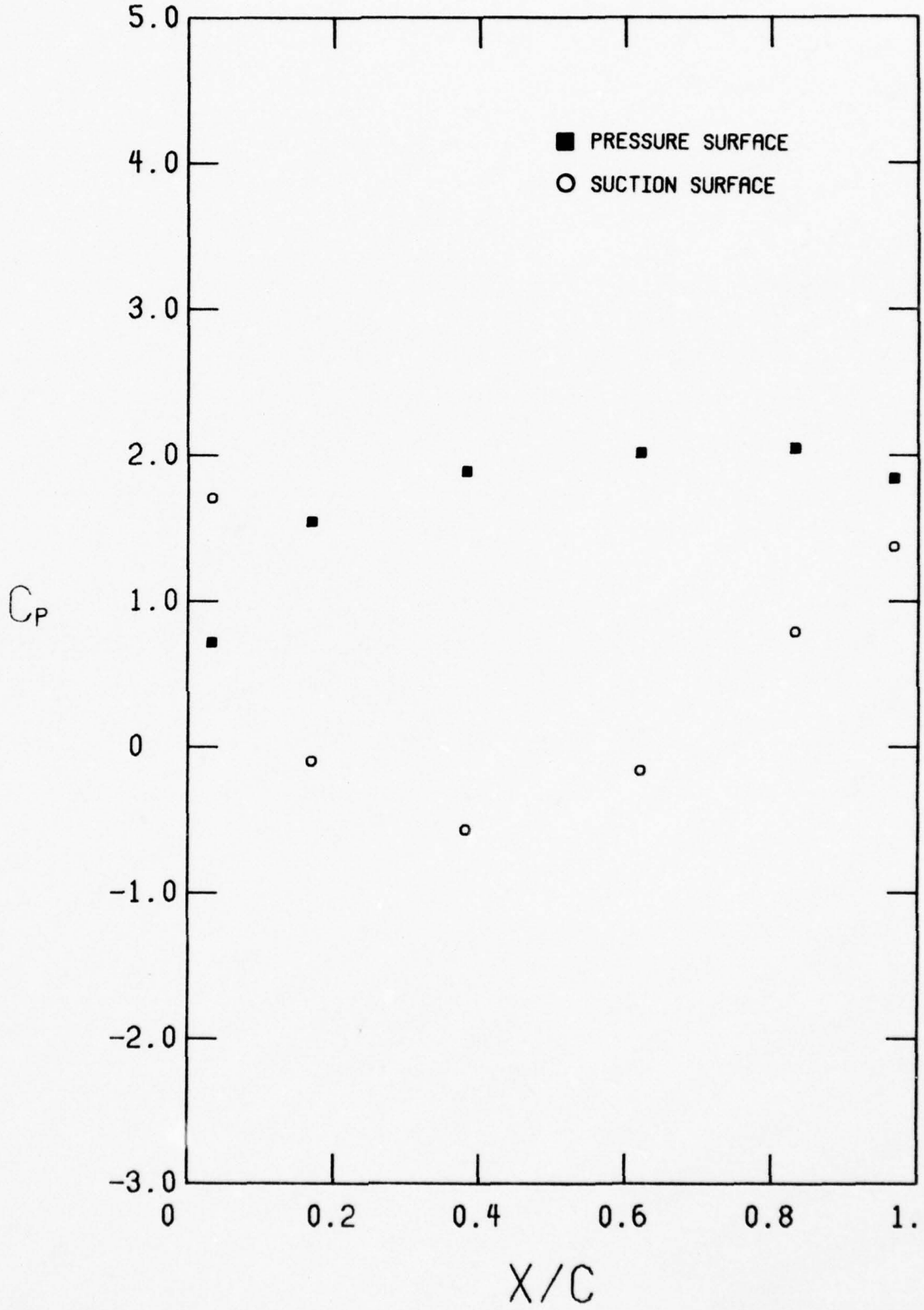

FIGURE 15. CONTINUED
c. $C_X/U = 0.949$

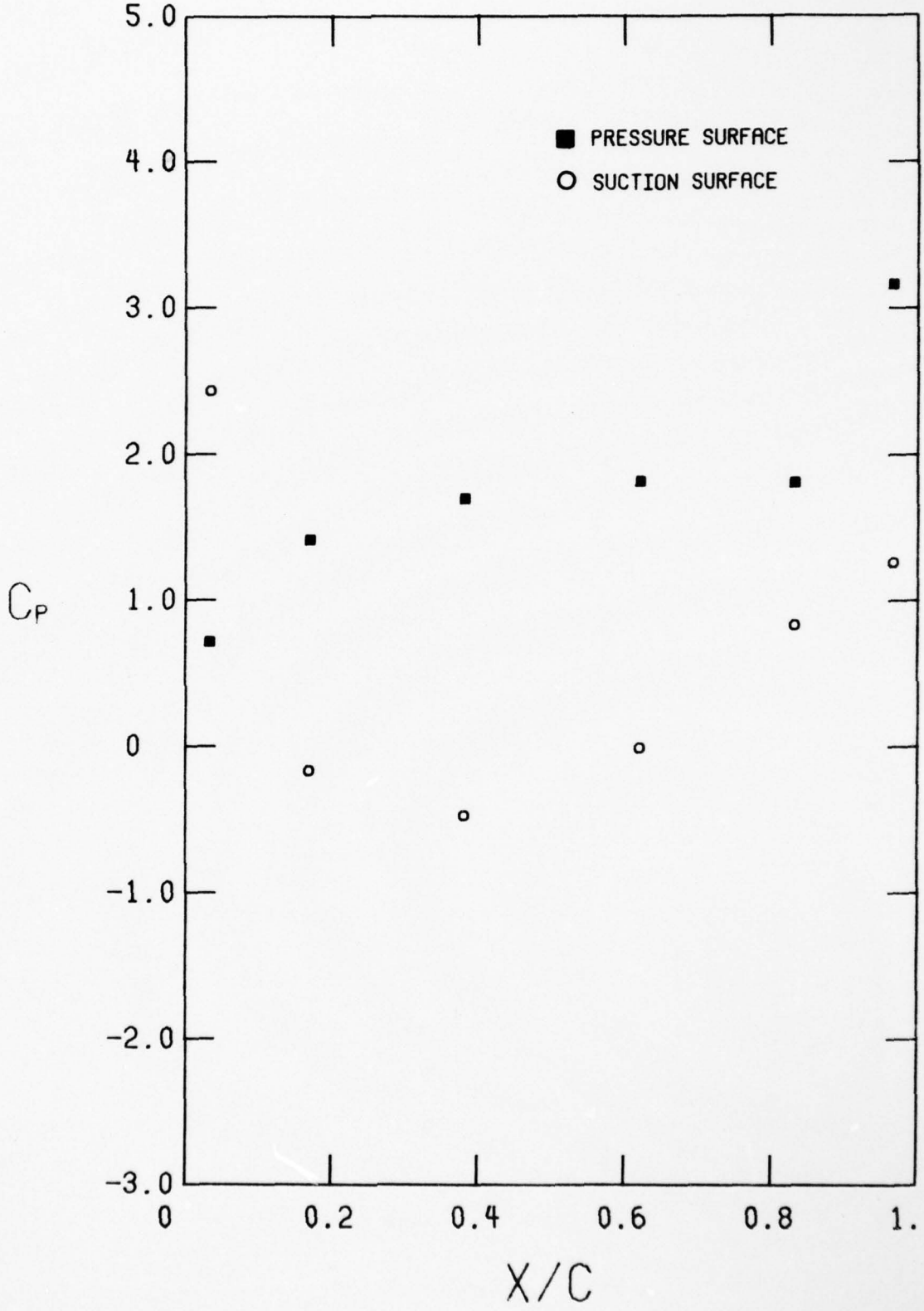

FIGURE 15. CONTINUED
D. $C_X/U = 0.901$

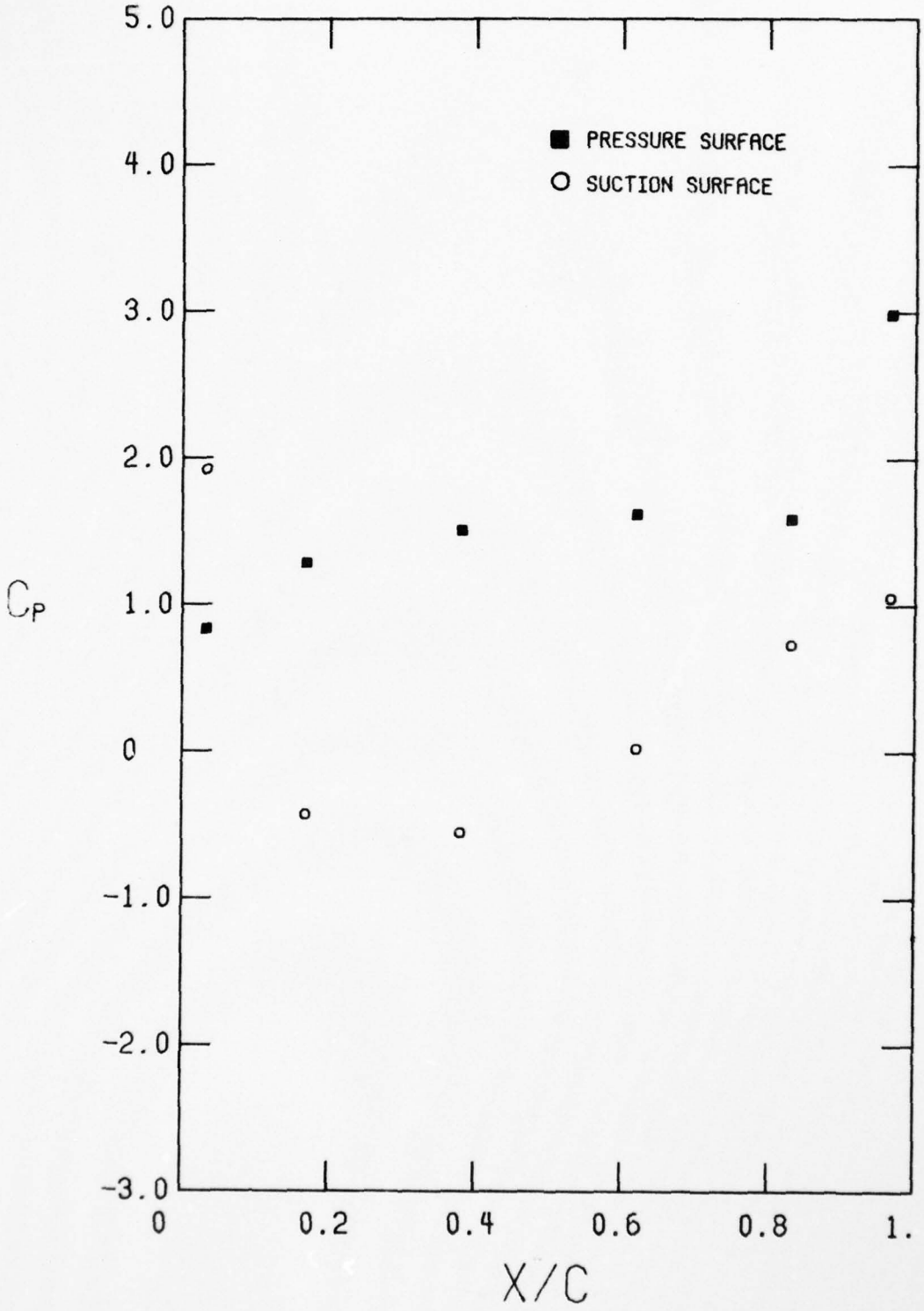

FIGURE 15. CONTINUED

E. $C_x/U = 0.845$

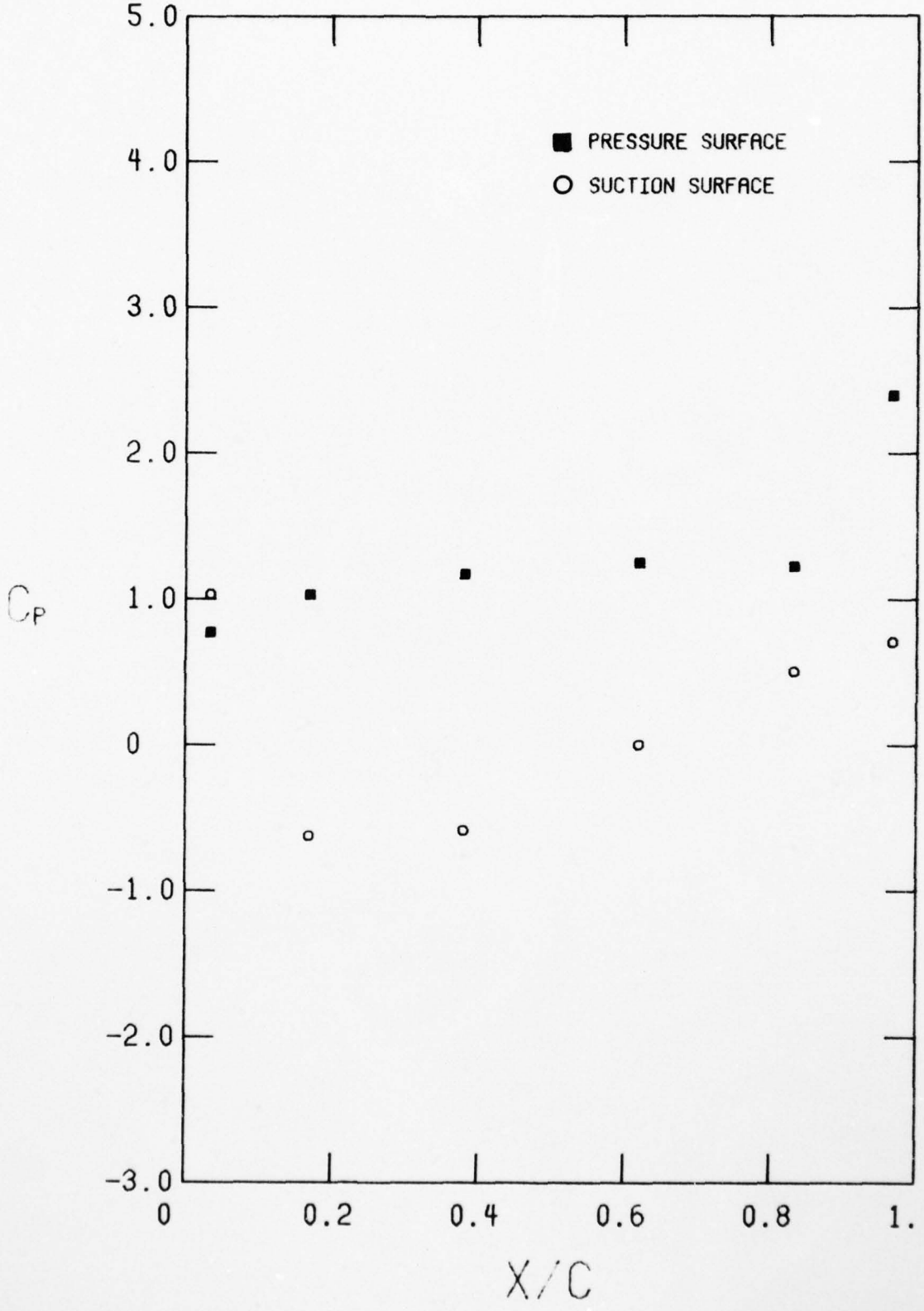

FIGURE 15. CONTINUED
F. $C_X/U = 0.747$

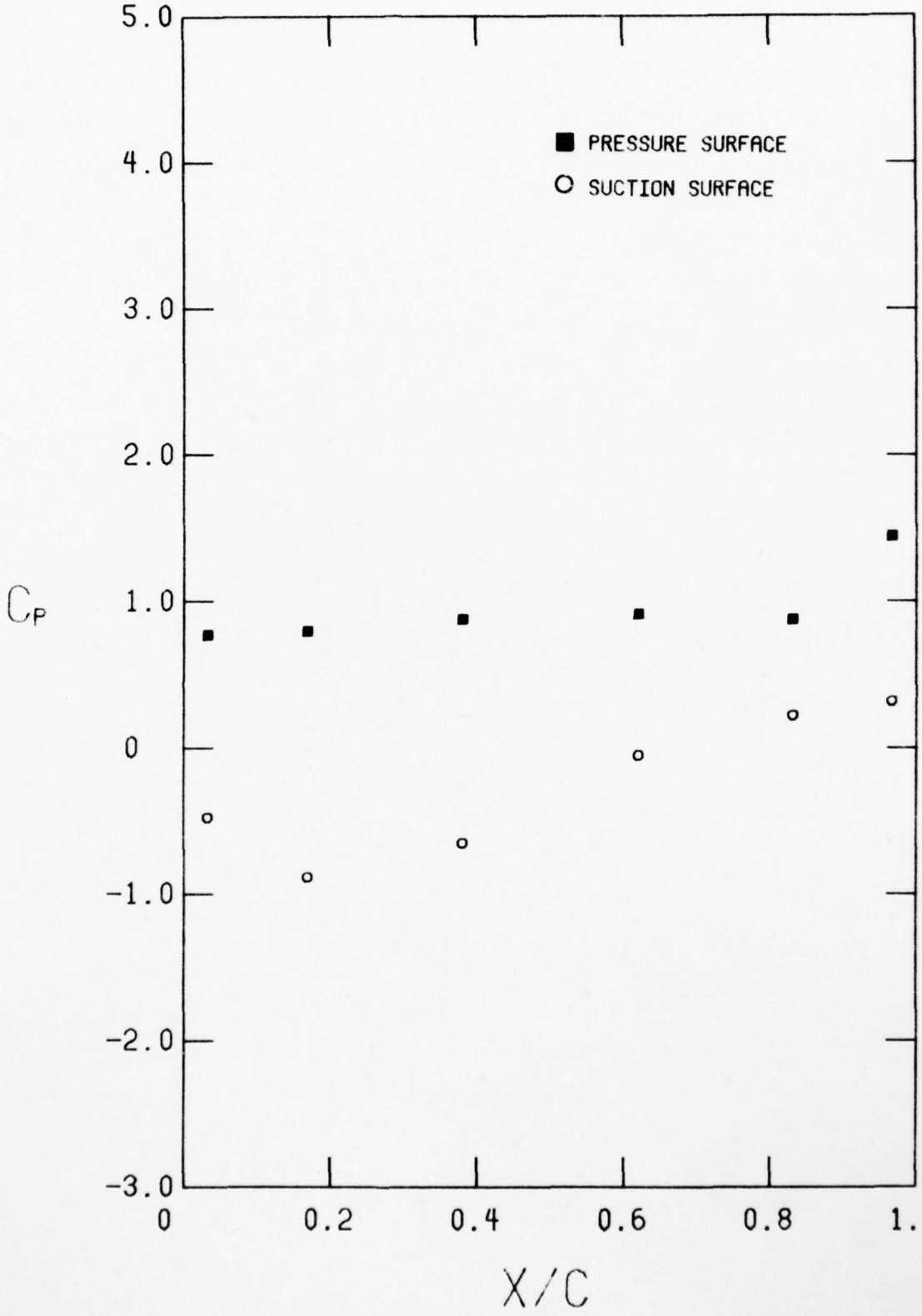

FIGURE 15. CONTINUED
G. $C_X/U = 0.661$

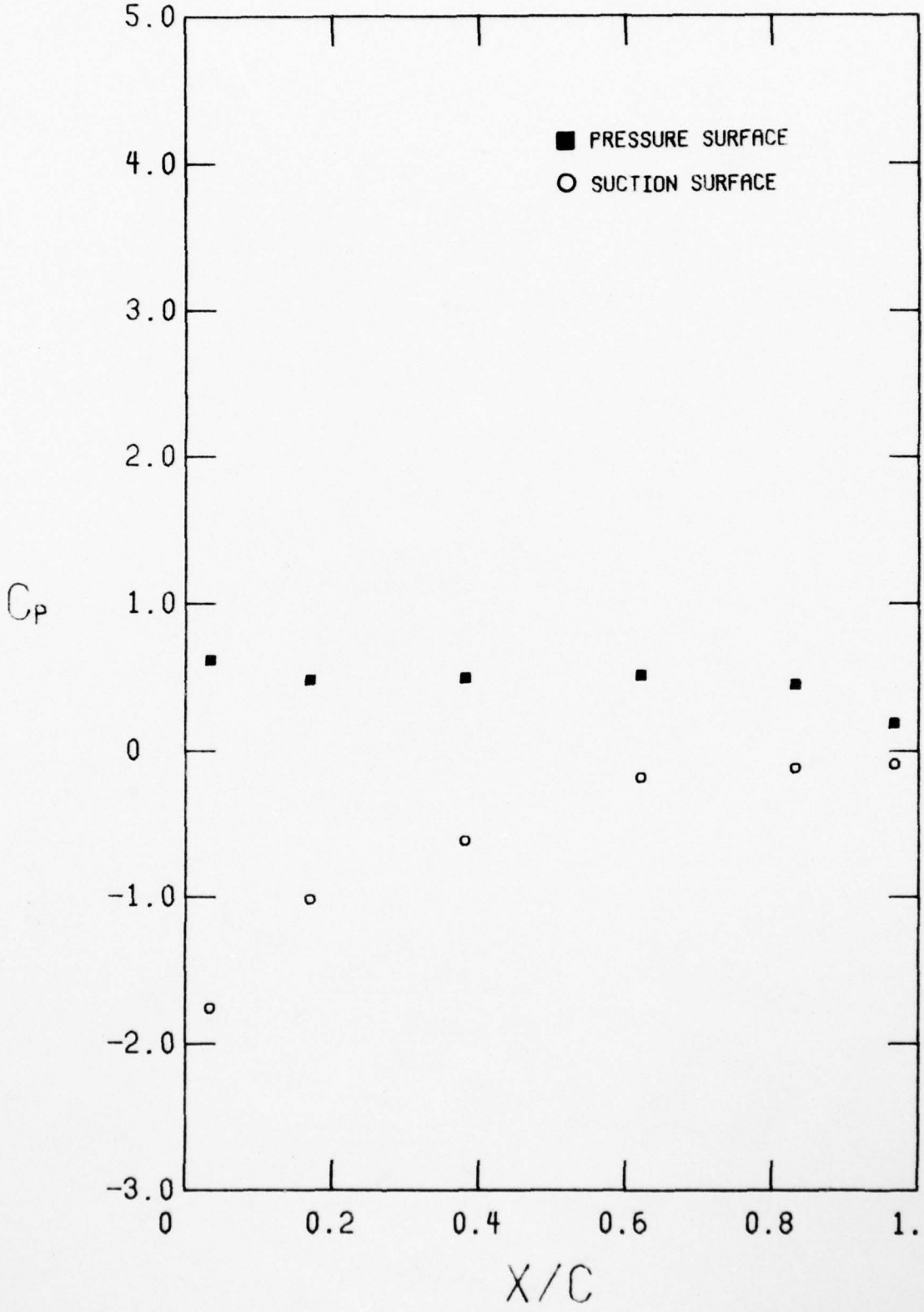

FIGURE 15. CONTINUED
H. $C_X/U = 0.554$

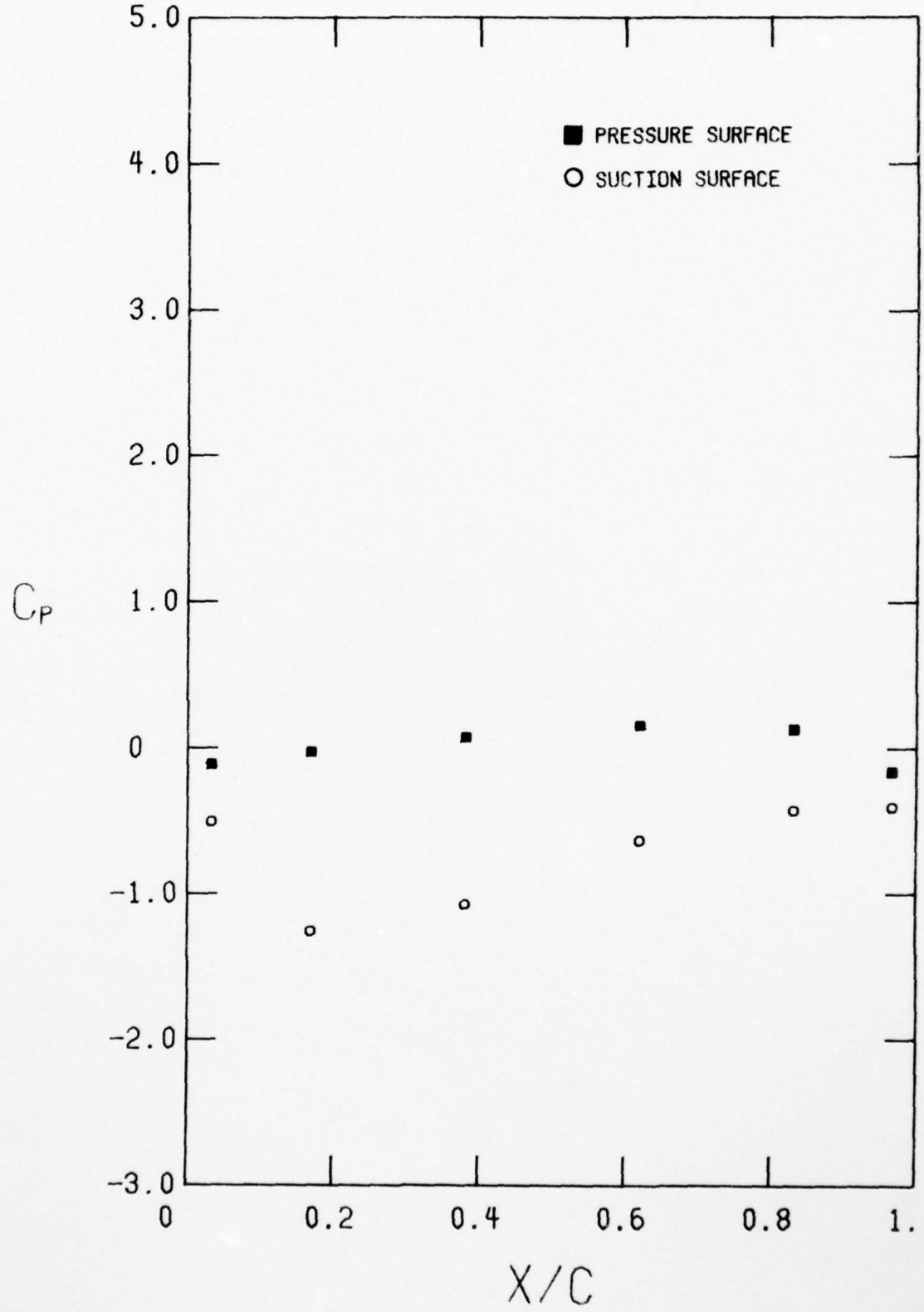

FIGURE 15. CONTINUED

I. $C_X/U = 0.547$ (STALL INCEPTION)

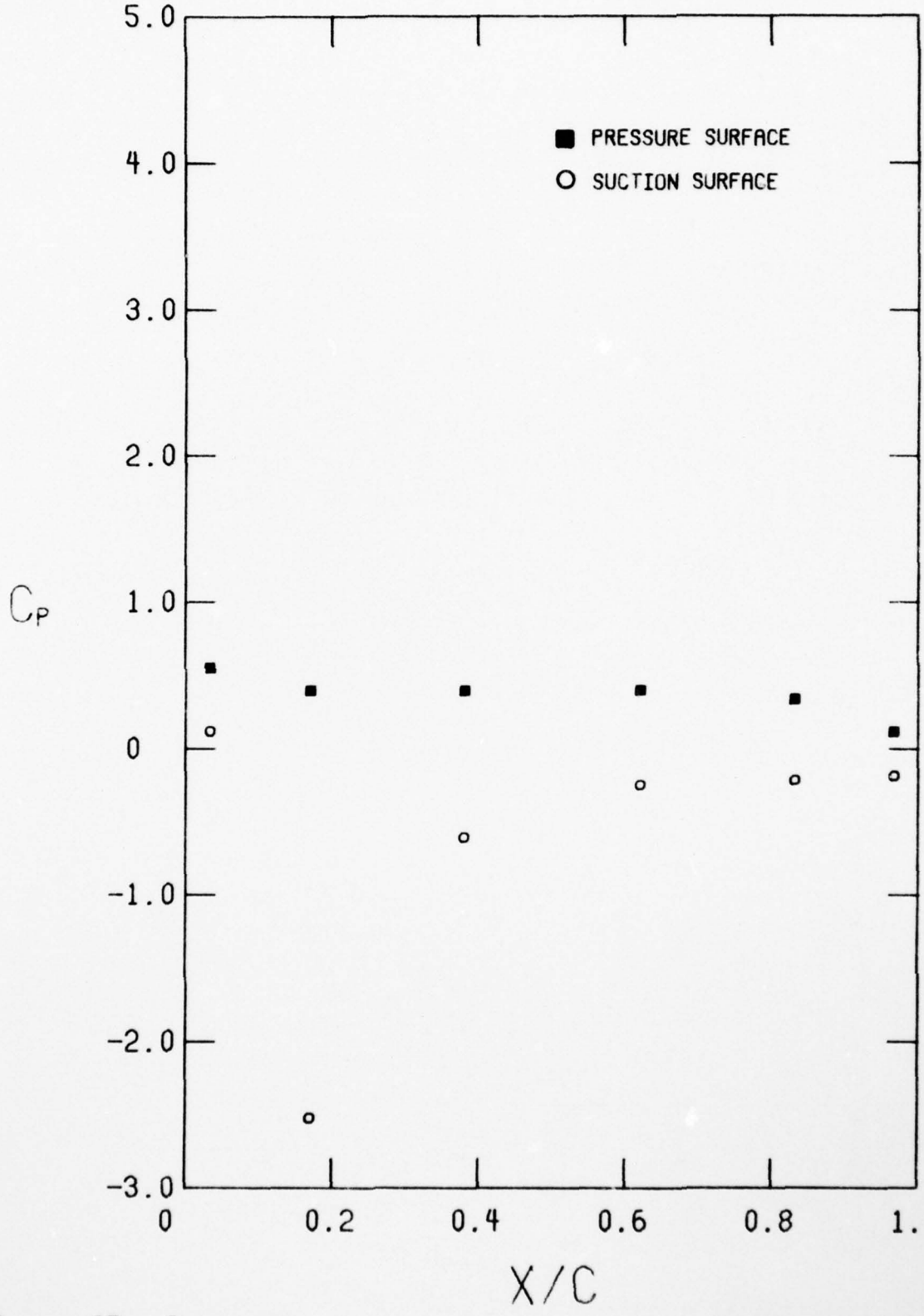

FIGURE 15. CONTINUED

J. $C_X/U = 0.534$ (STALLED)

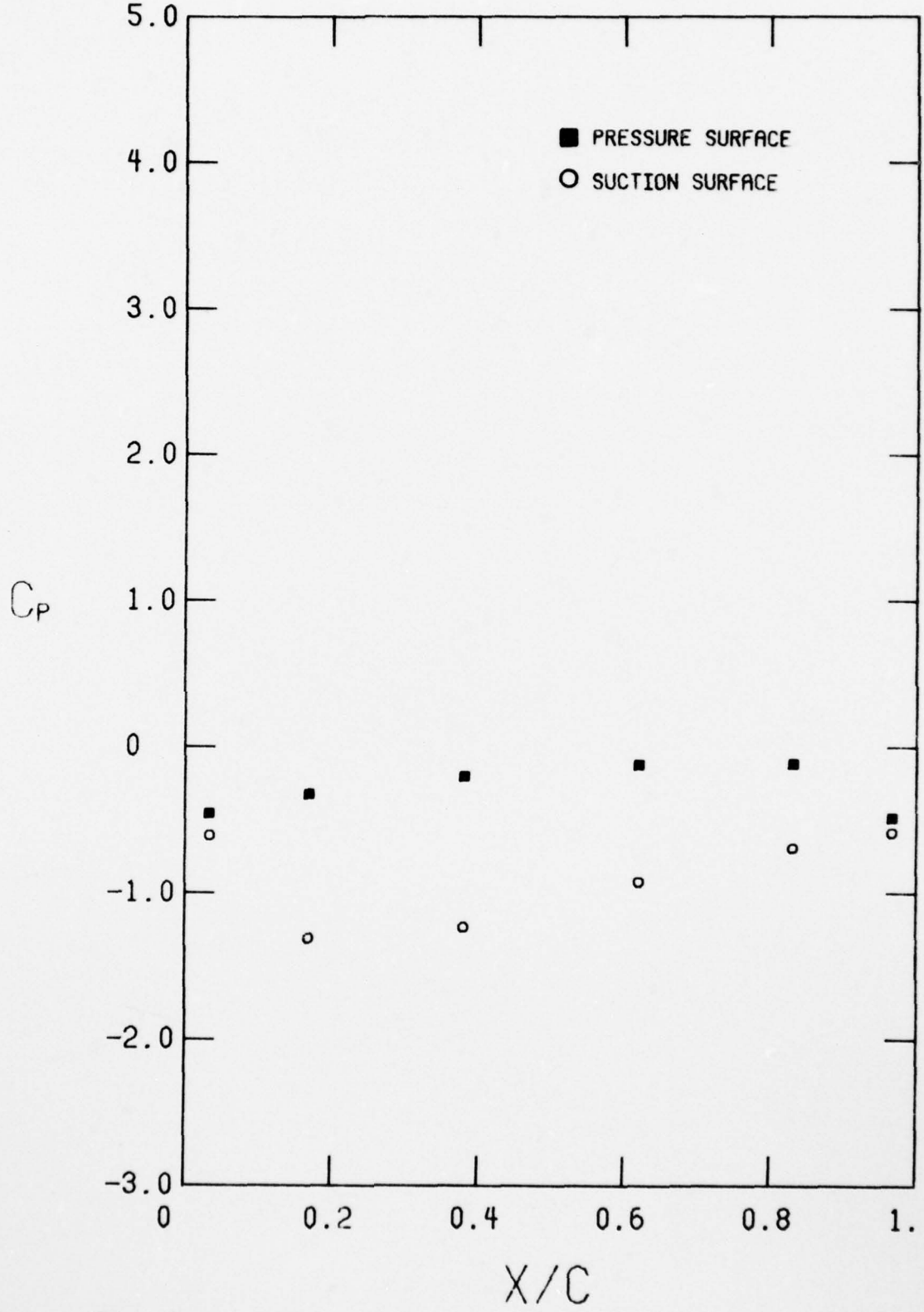

FIGURE 15. CONTINUED

K. $C_X/U = 0.496$ (STALLED)

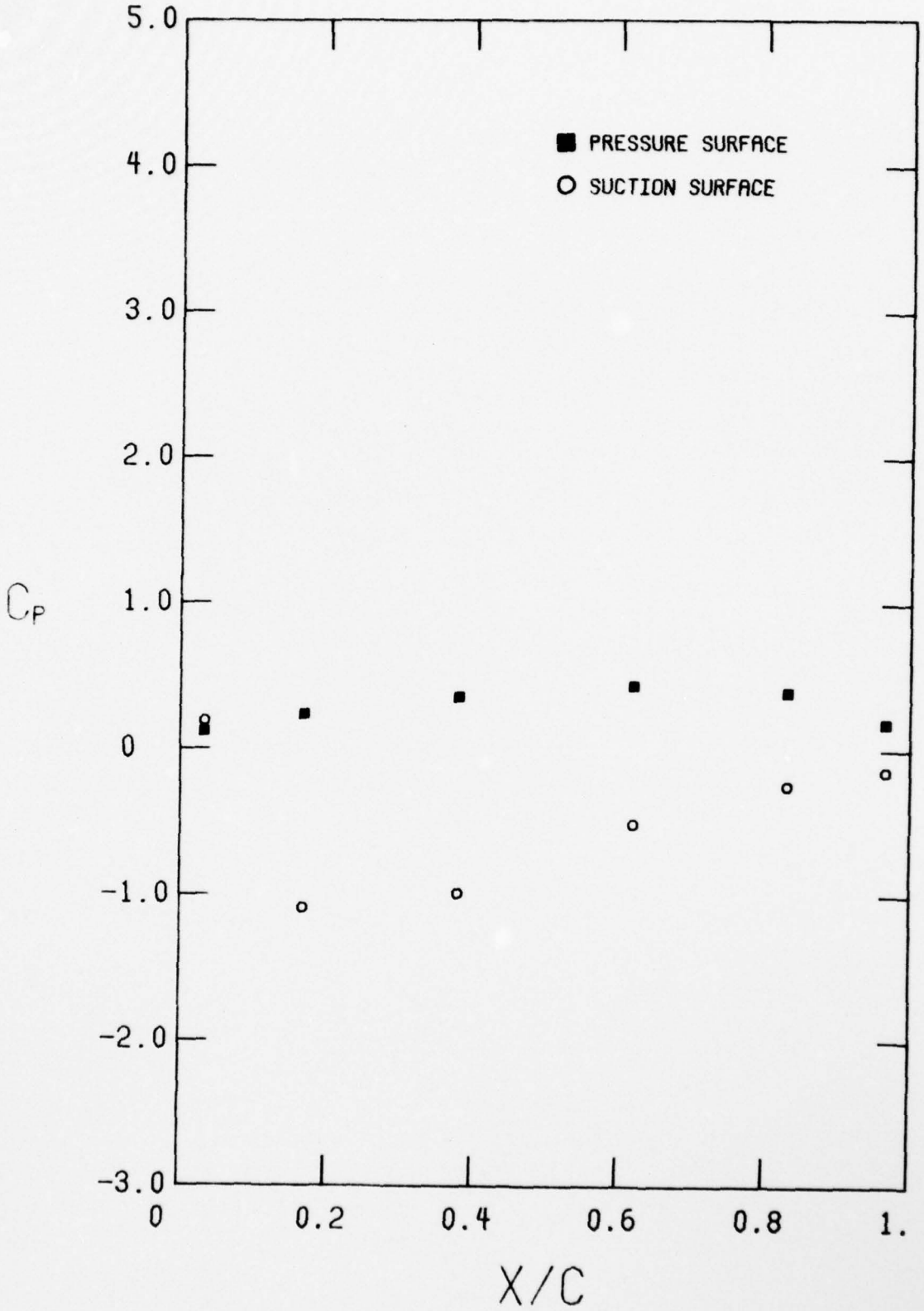

FIGURE 15. CONCLUDED

L. $C_X/U = 0.597$ (NEAR RECOVERY)

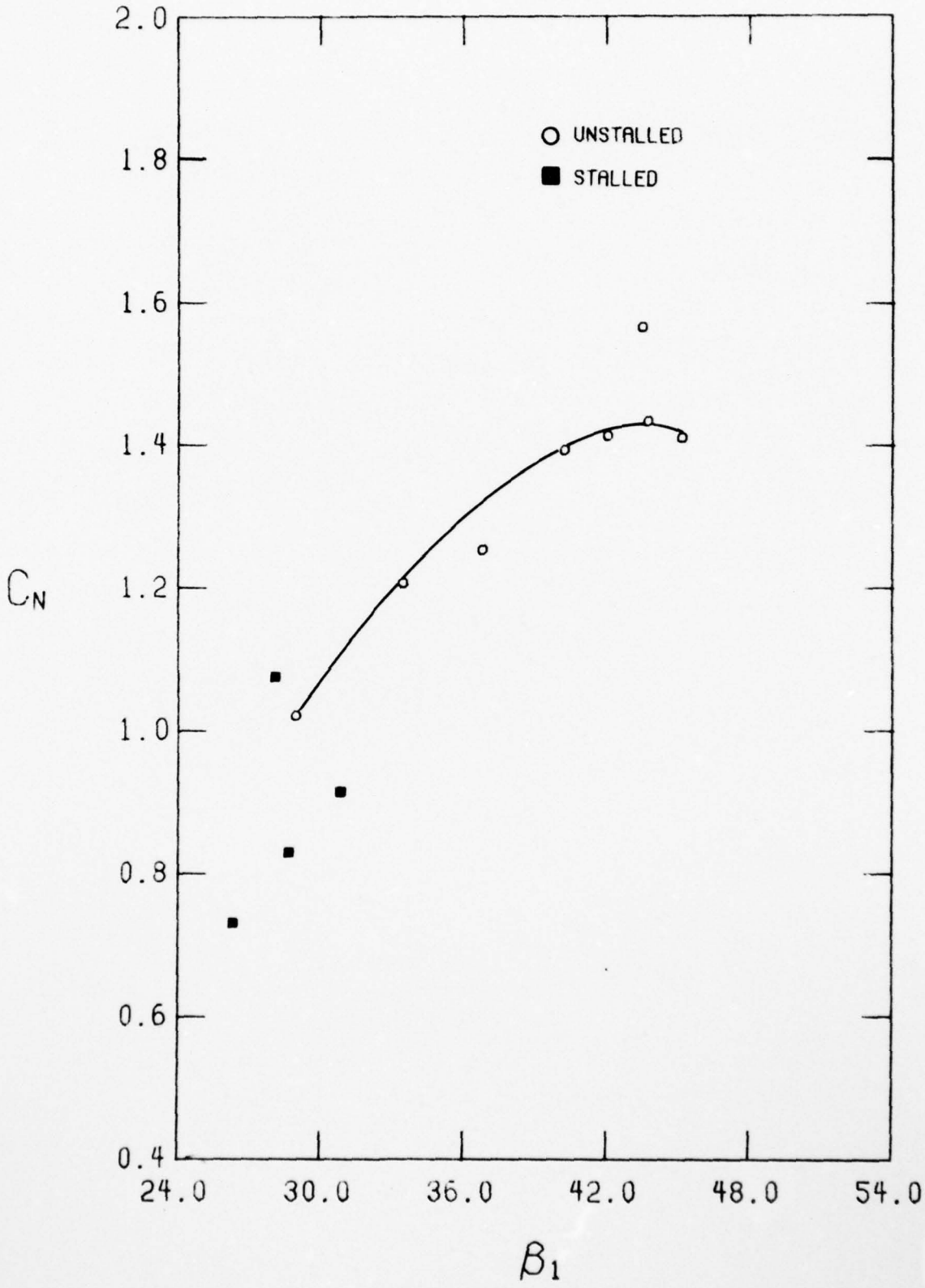

FIGURE 16. DISTORTED FLOW NORMAL FORCE COEFFICIENT AS A FUNCTION OF INLET ANGLE

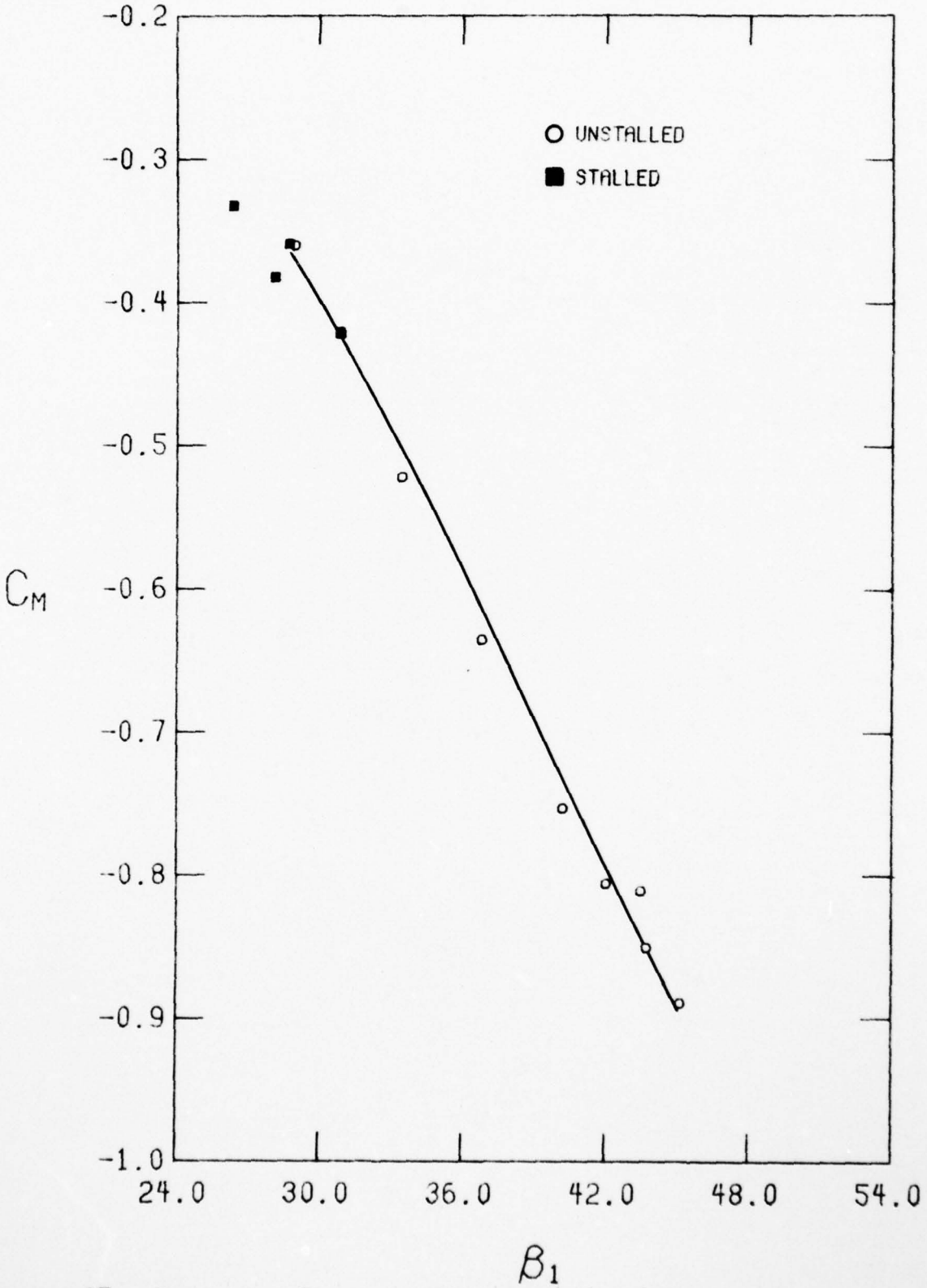

FIGURE 17. DISTORTED PITCHING MOMENT COEFFICIENT AS A FUNCTION OF INLET ANGLE

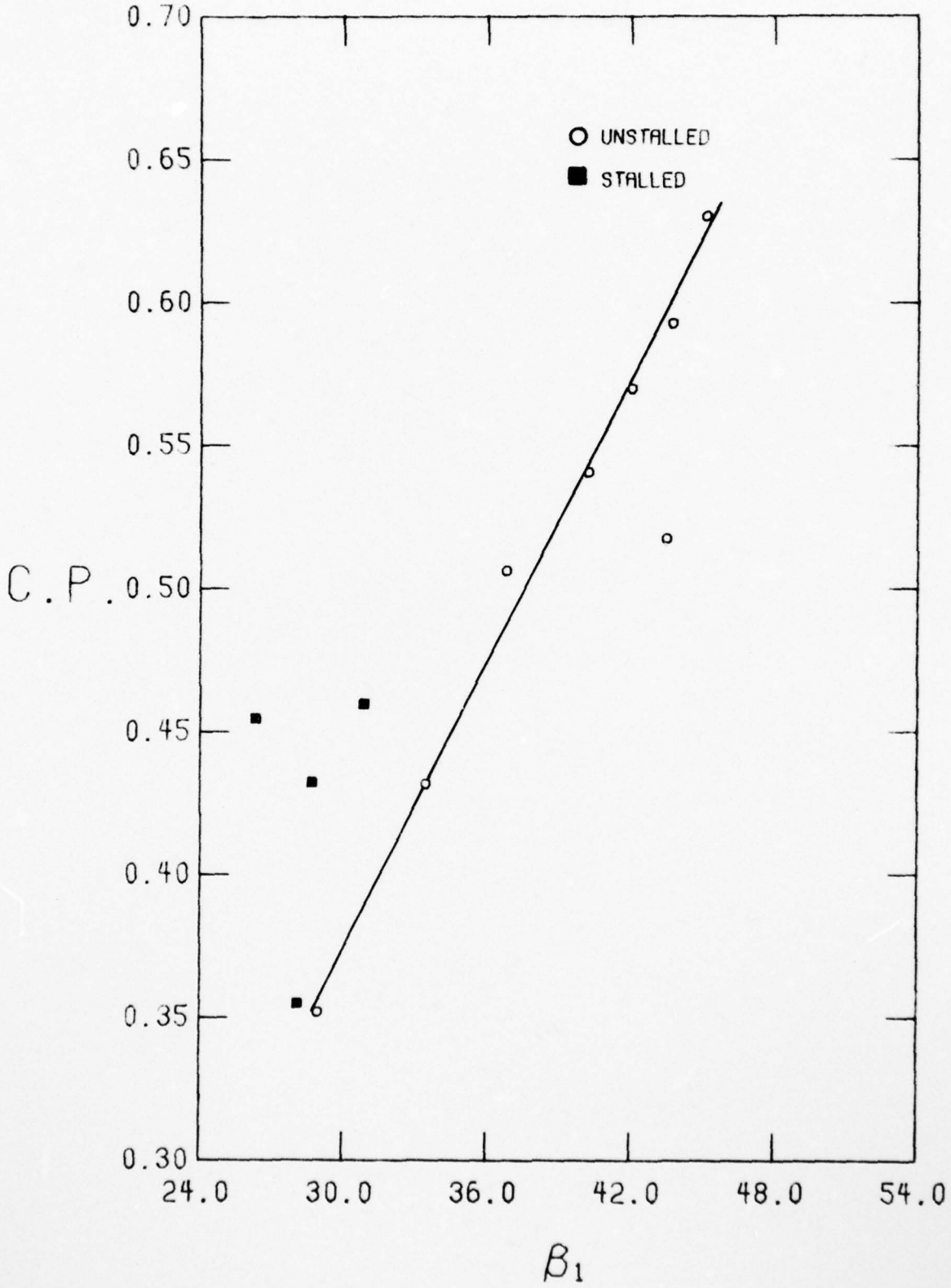

FIGURE 18. DISTORTED FLOW CENTER OF PRESSURE LOCATION AS A FUNCTION OF INLET ANGLE

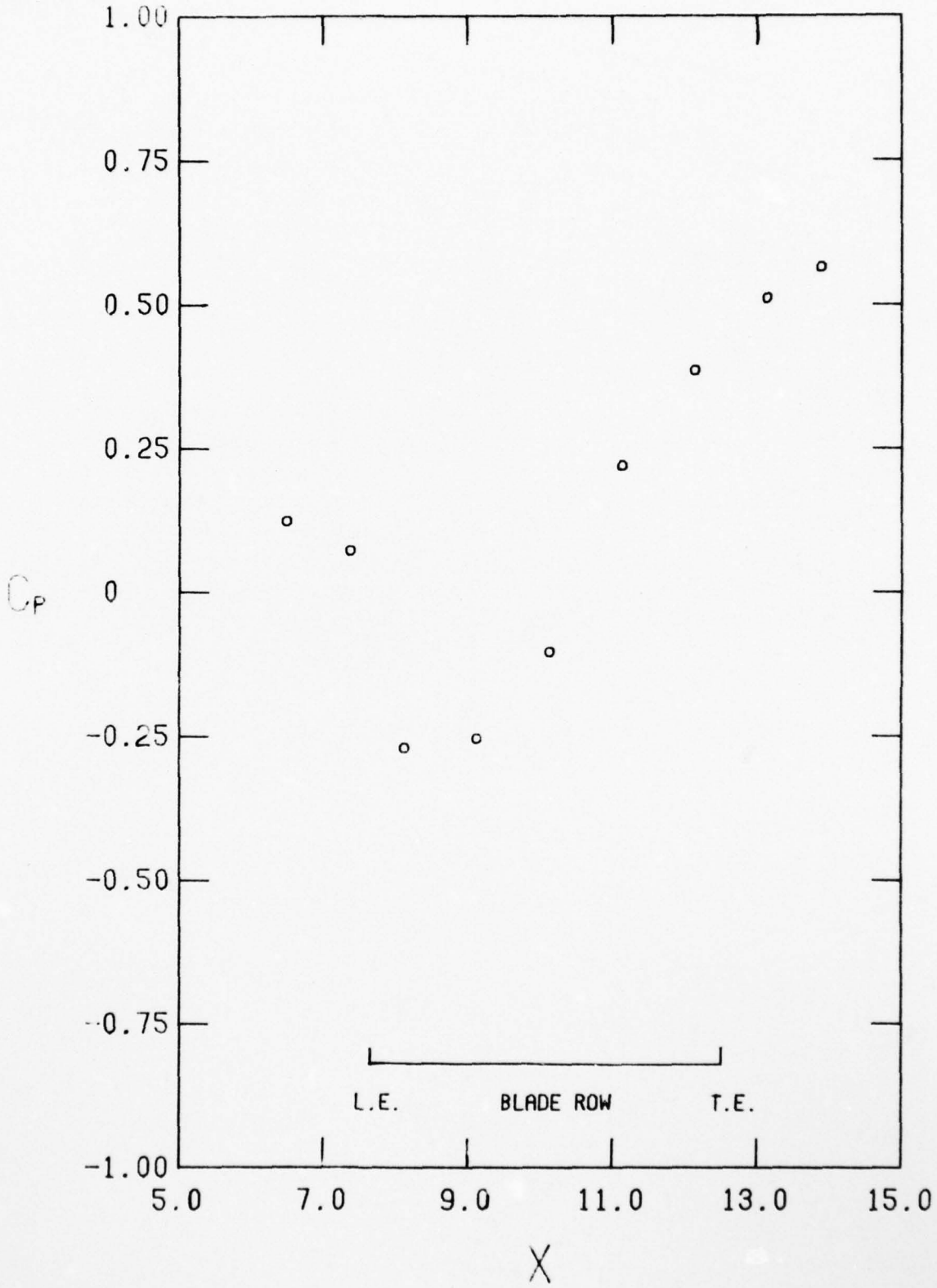

FIGURE 19. DISTORTED FLOW PRESSURE COEFFICIENT VARIATION ACROSS ROTOR A. $C_X/U = 1.005$

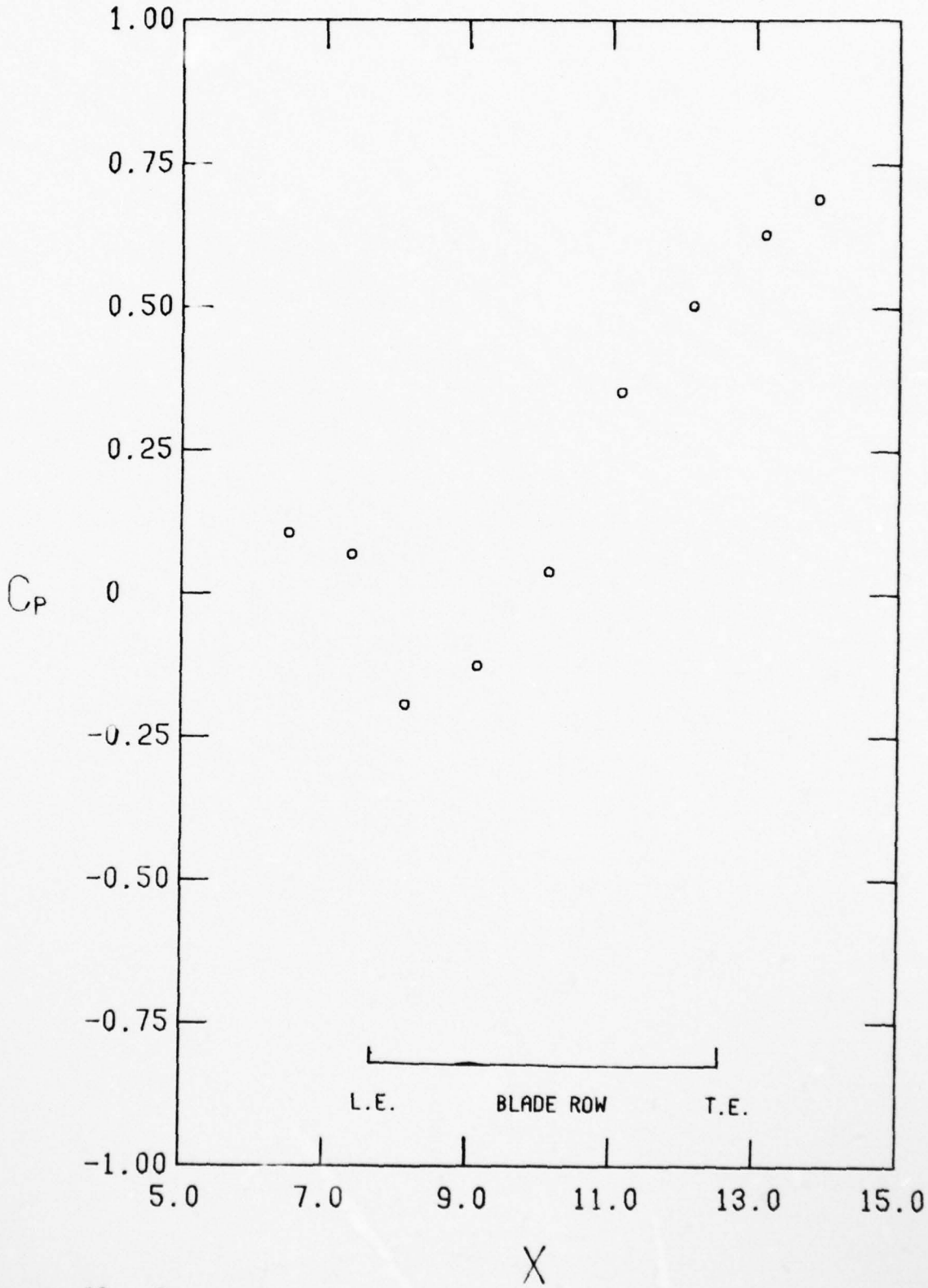

FIGURE 19. CONTINUED
B. Cx/U = 0.956

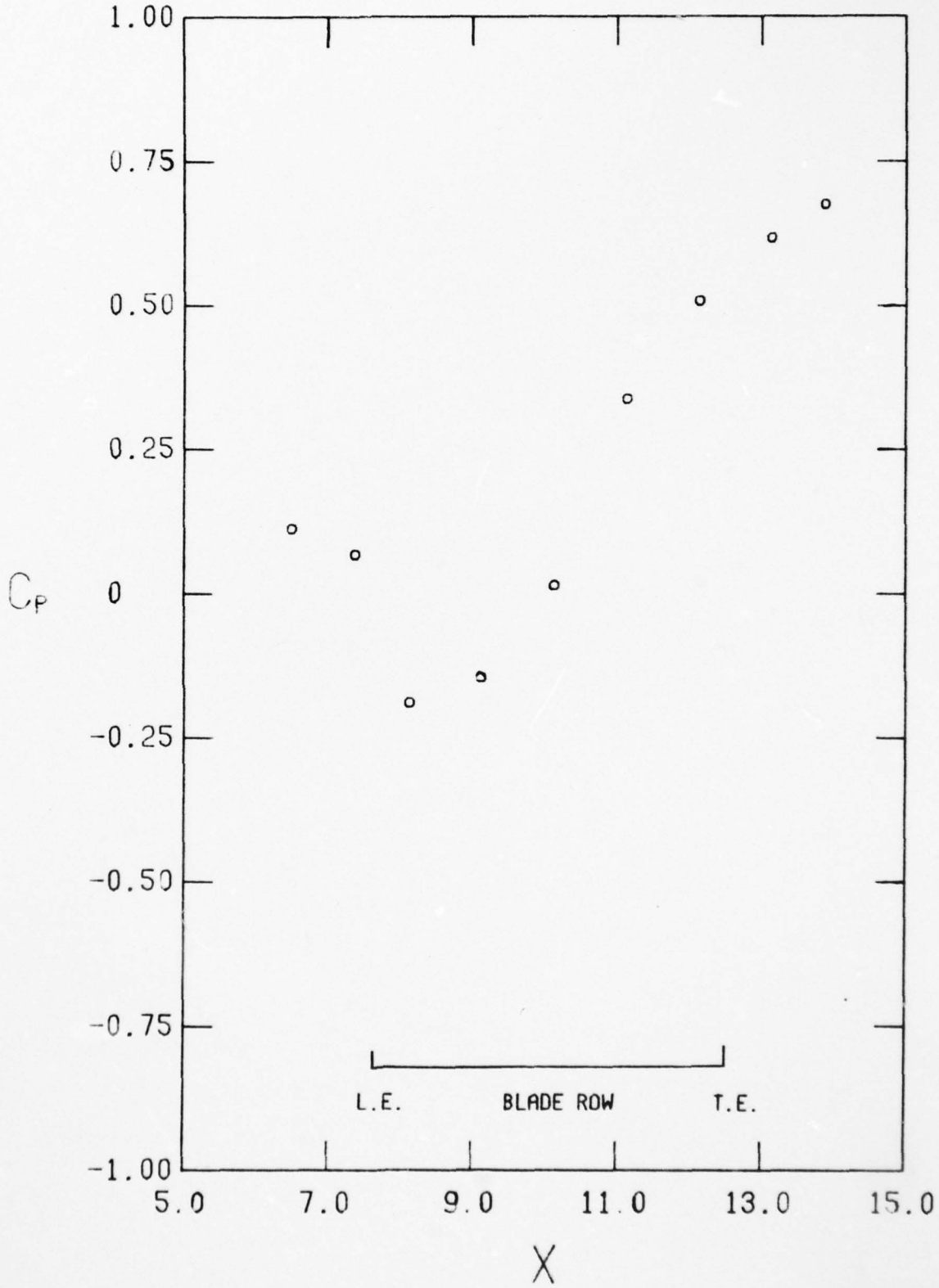

FIGURE 19. CONTINUED
c. $C_X/U = 0.949$

AD-A046 055 NORTH CAROLINA STATE UNIV RALEIGH ENGINEERING DESIGN--ETC F/G 13/7
EFFECT OF INLET DISTORTION ON PERFORMANCE OF A COMPRESSOR STAGE--ETC(U)
APR 77 L W HARDIN, W C GRIFFITH, J N PERKINS F44620-76-C-0055

UNCLASSIFIED NCSU/EDC-77-1 AFOSR-TR-77-1238 NL

2 OF 2
ADA
046055

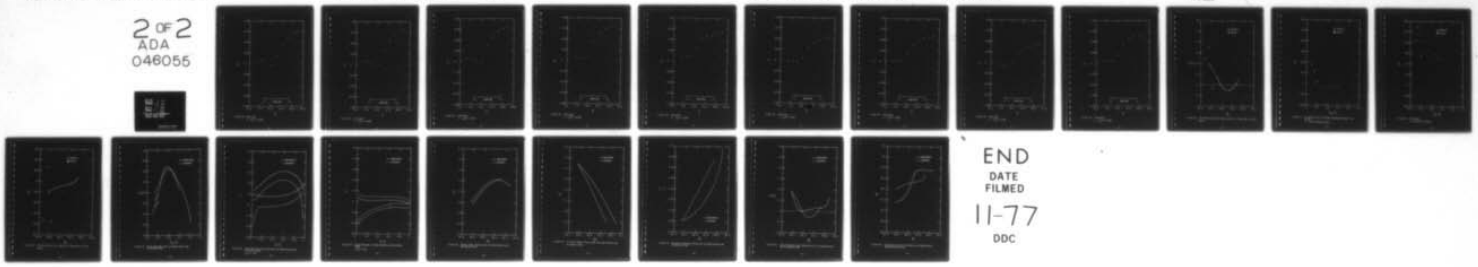

END
DATE
FILMED
11-77
DDC

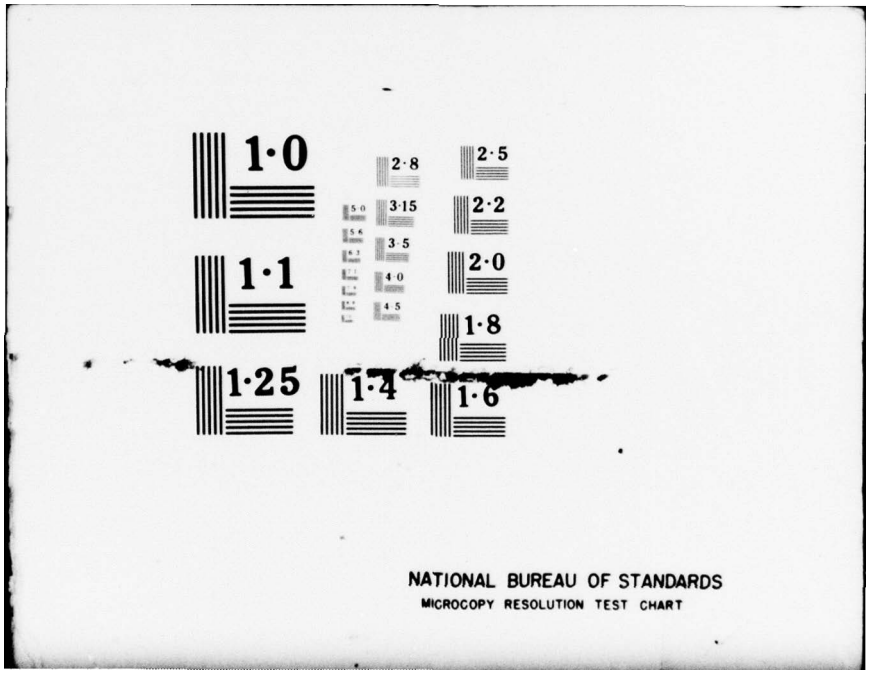
1·0
1·1
1·25
1·4
1·6
1·8
2·0
2·2
2·5
2·8
3·15
3·5
4·0
4·5
5·0
5·6
NATIONAL BUREAU OF STANDARDS
MICROCOPY RESOLUTION TEST CHART

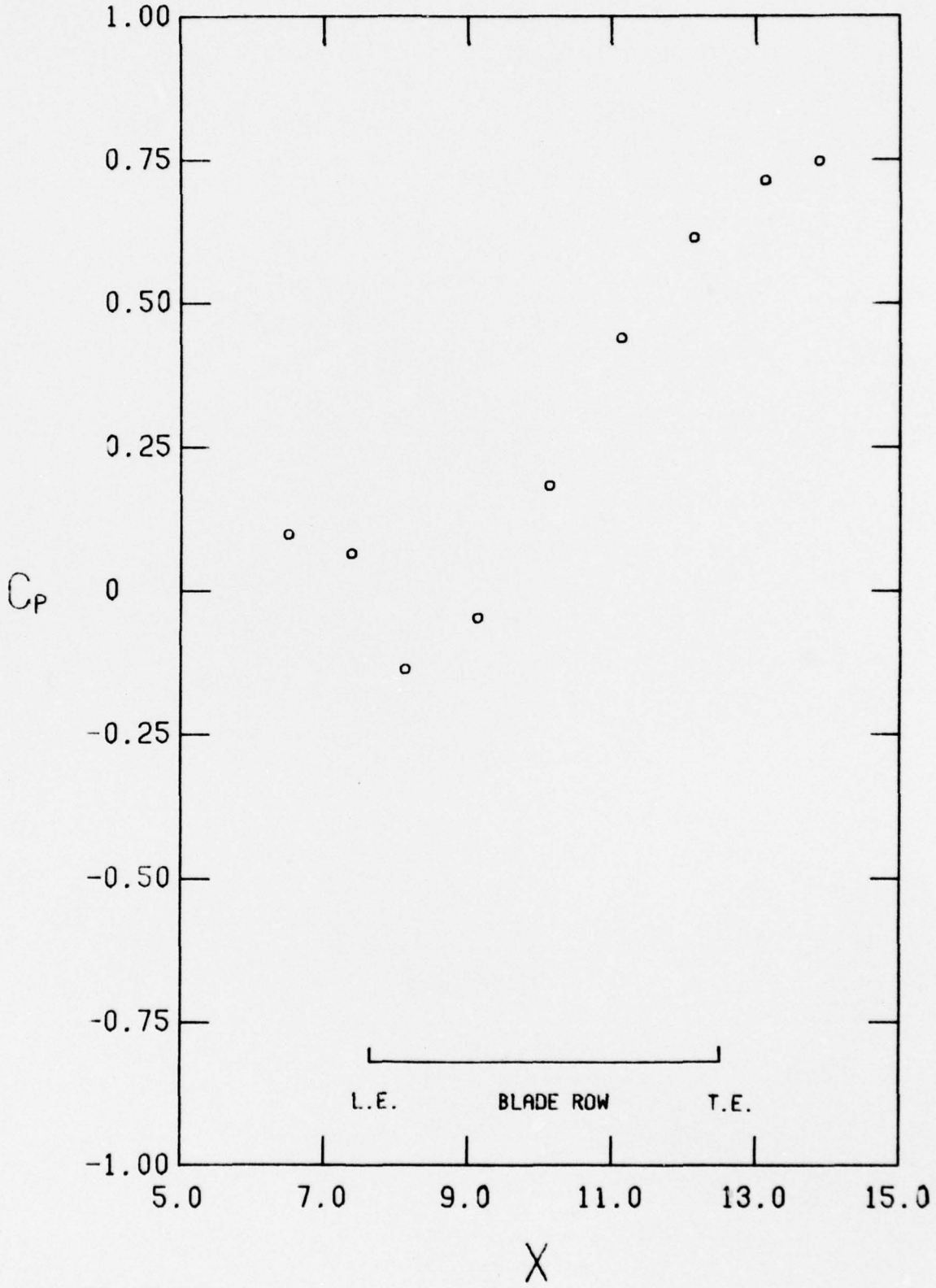

FIGURE 19. CONTINUED

D. $C_X/U = 0.901$

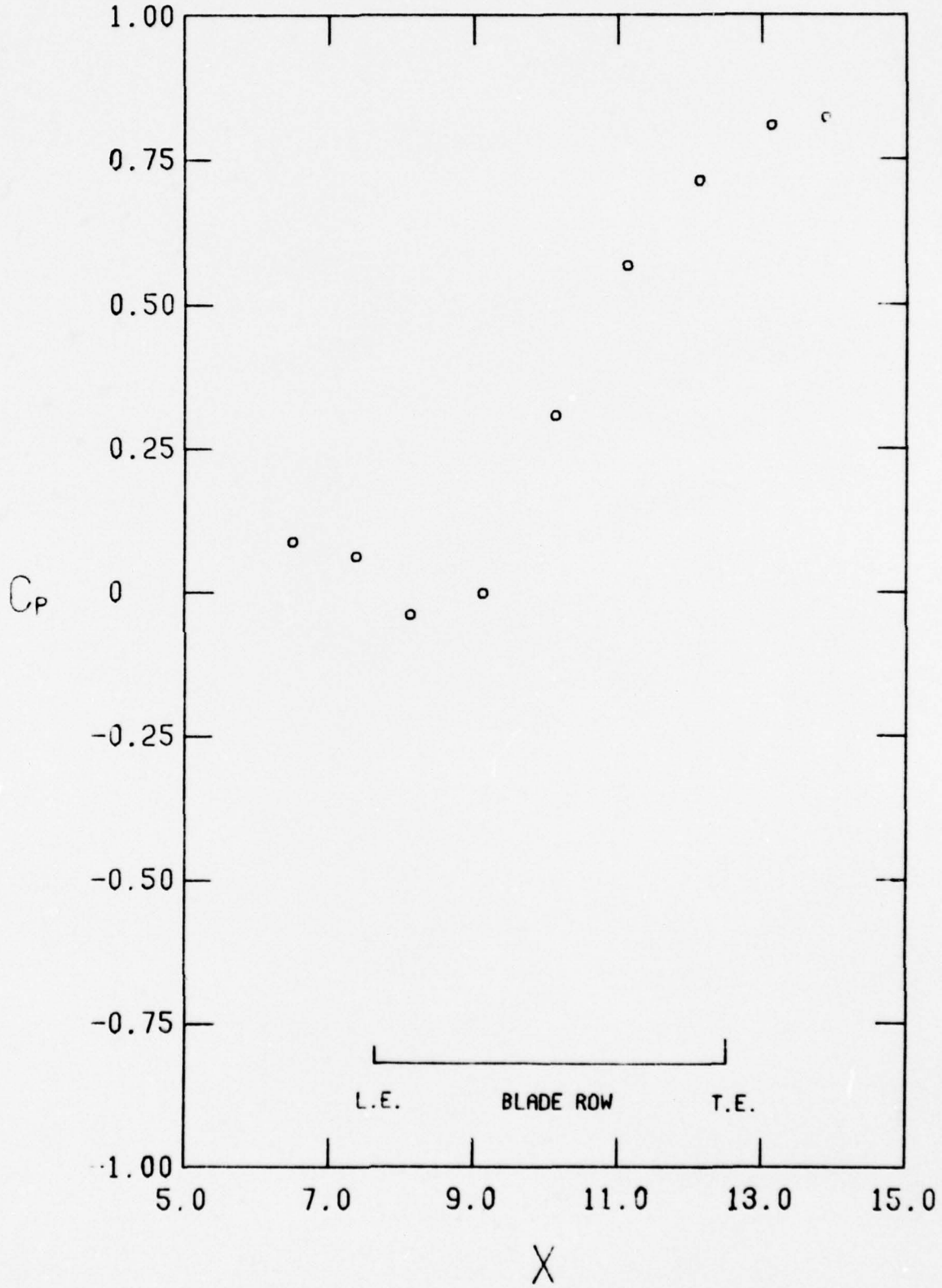

FIGURE 19. CONTINUED
E. $C_X/U = 0.845$

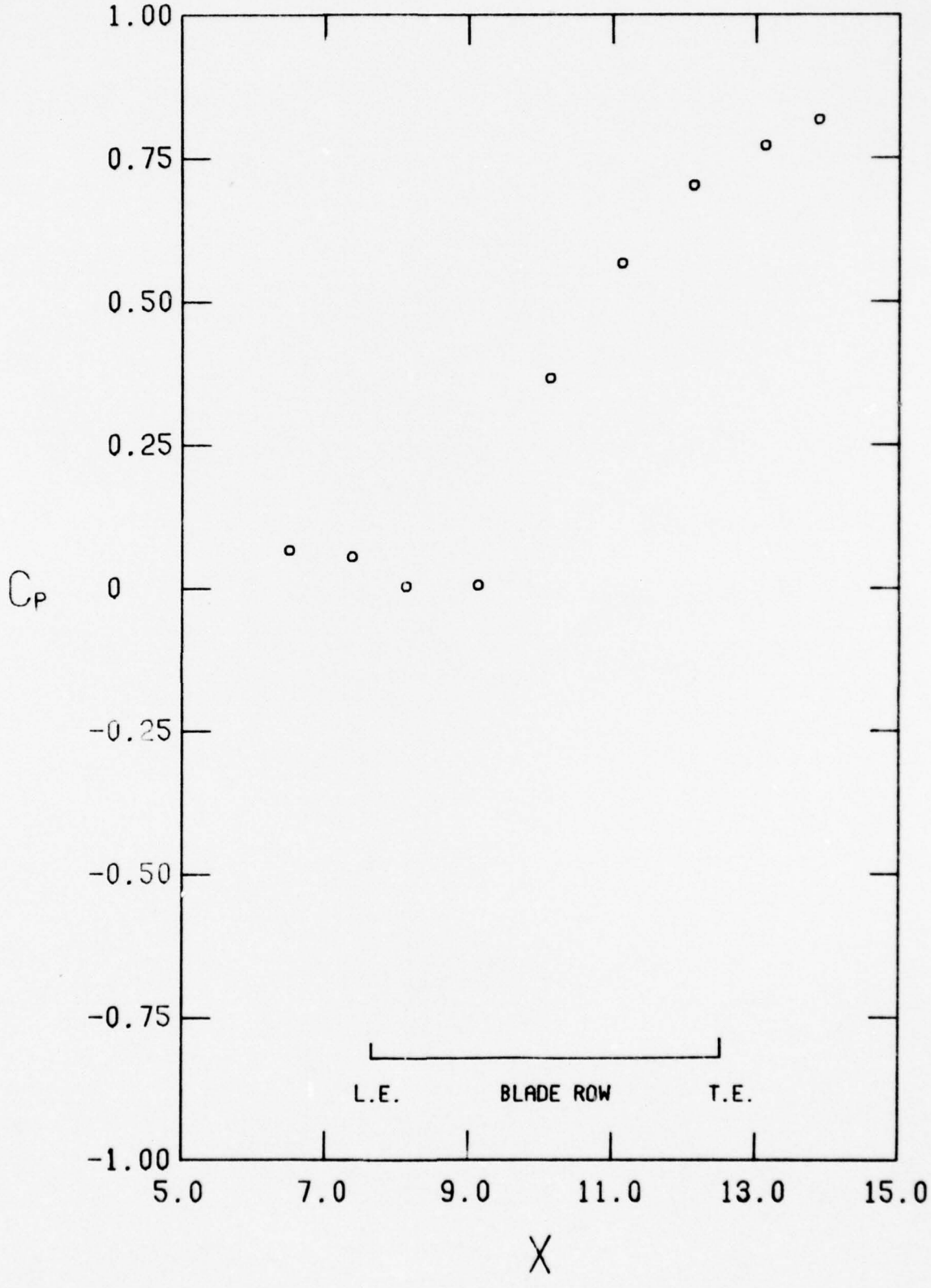

FIGURE 19. CONTINUED
F. $C_X/U = 0.747$

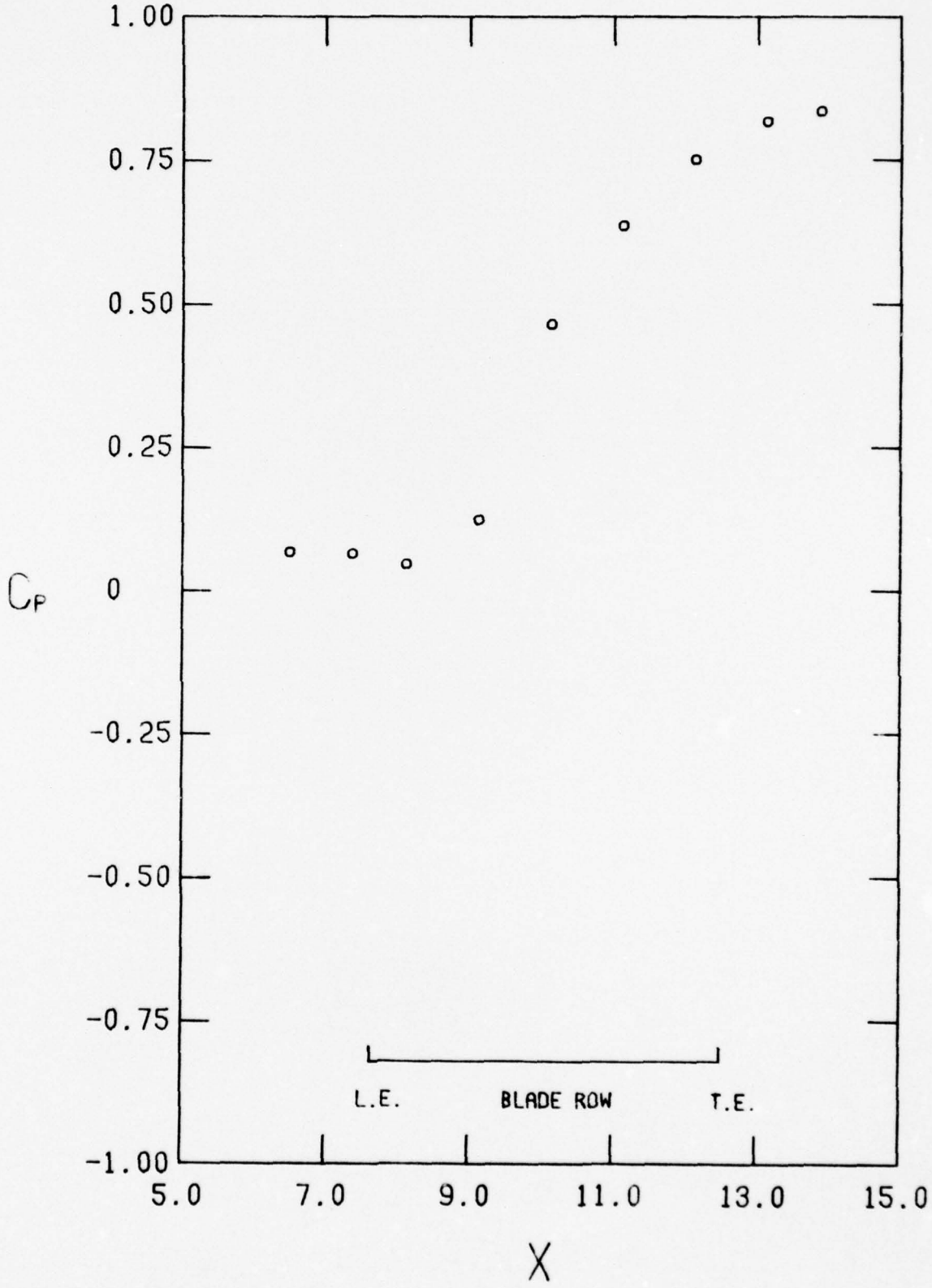

FIGURE 19. CONTINUED
G. $C_X/U = 0.661$

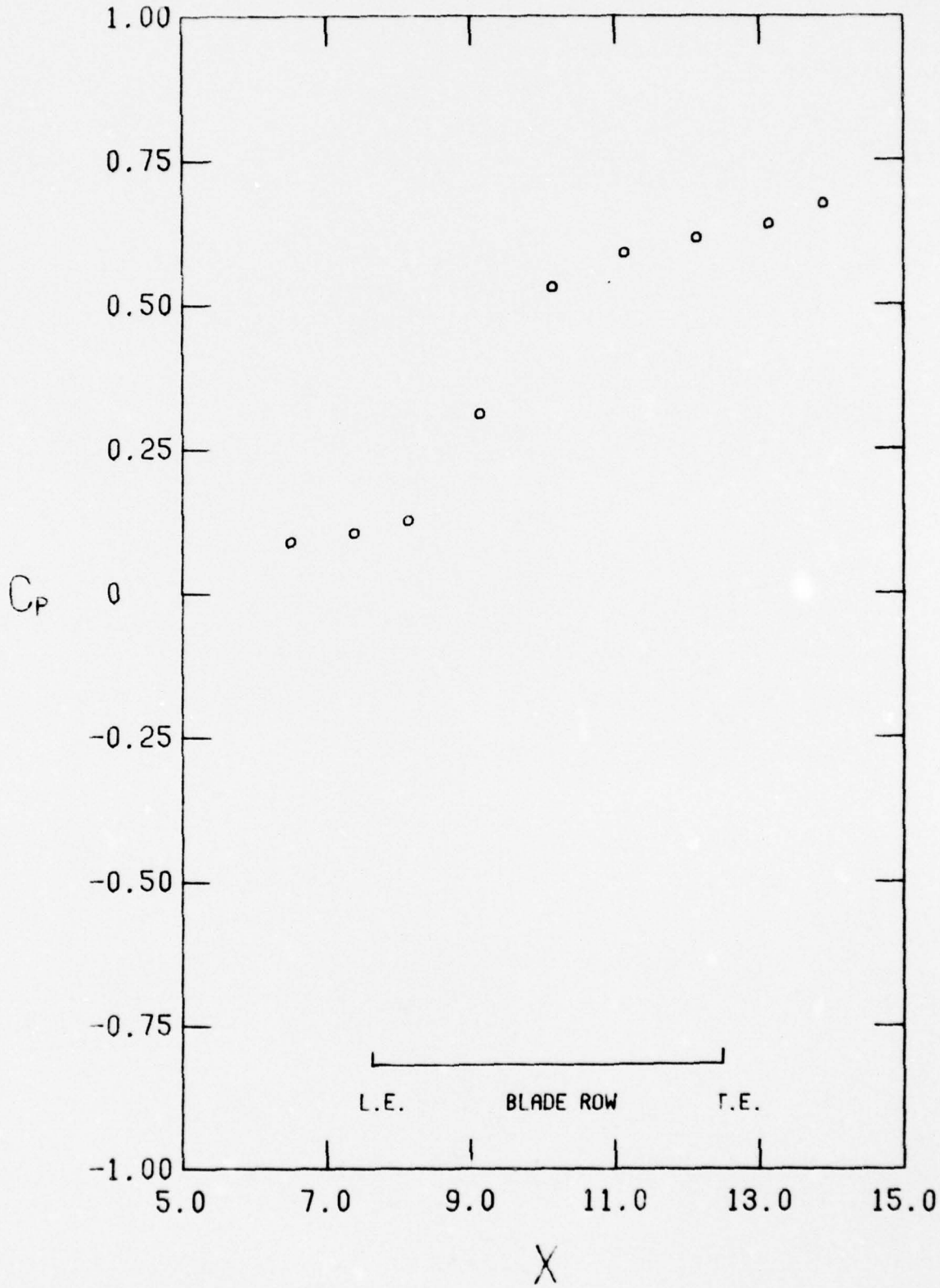

FIGURE 19. CONTINUED
H. $C_X/U = 0.554$

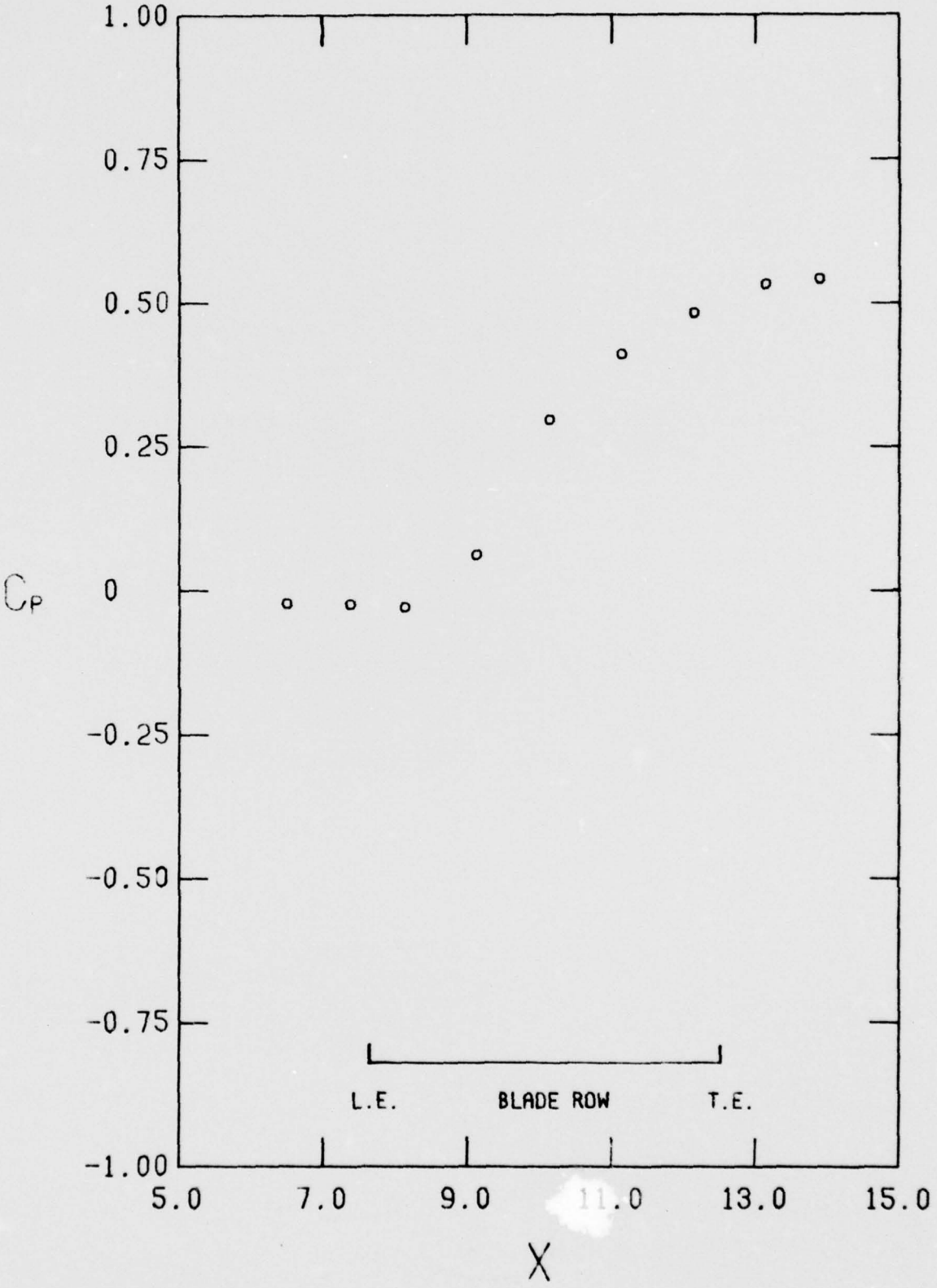

FIGURE 19. CONTINUED
1. $C_X/U = 0.547$

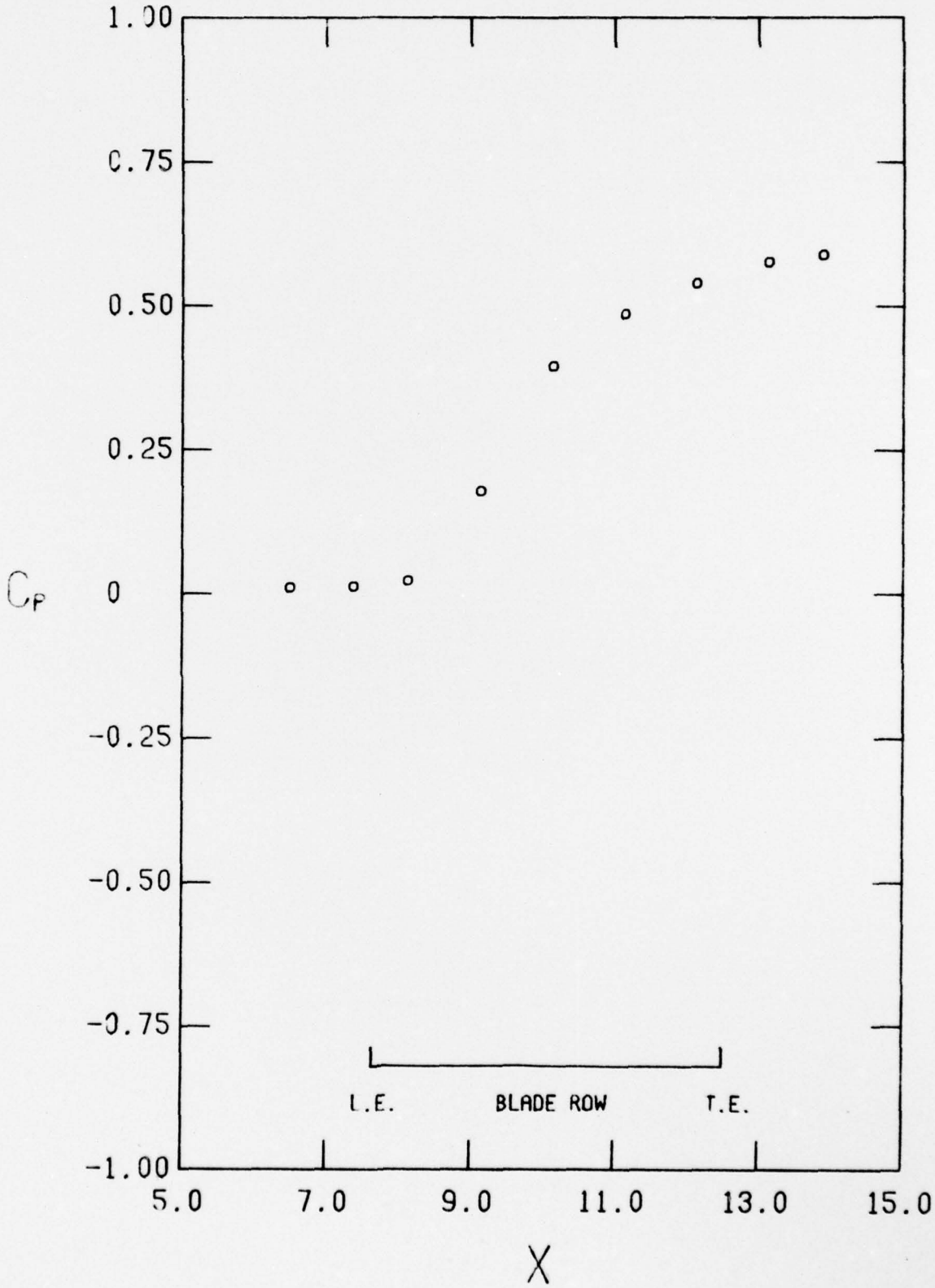

FIGURE 19. CONTINUED
J. $C_X/U = 0.534$

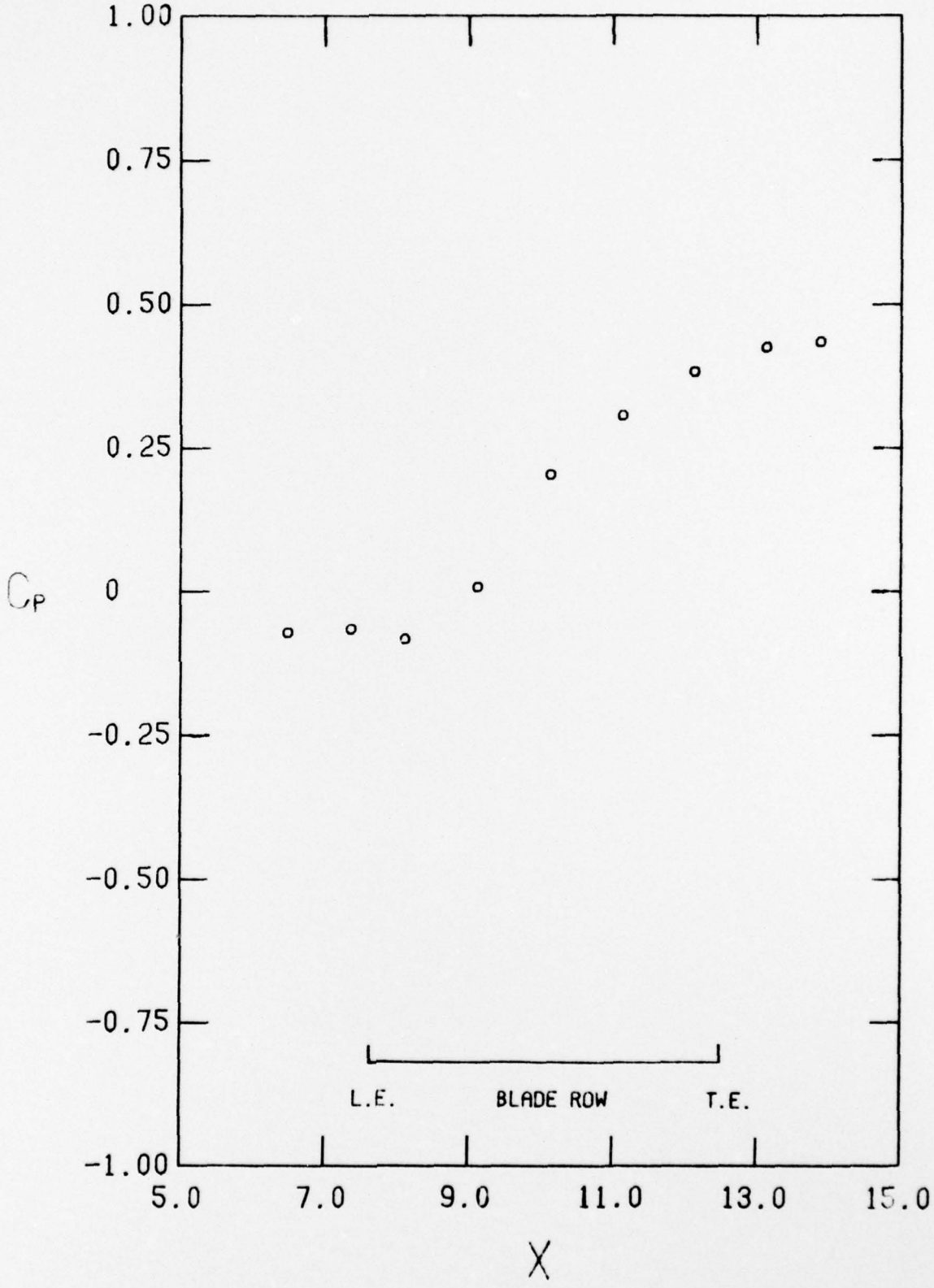

FIGURE 19. CONTINUED
K. $C_X/U = 0.496$

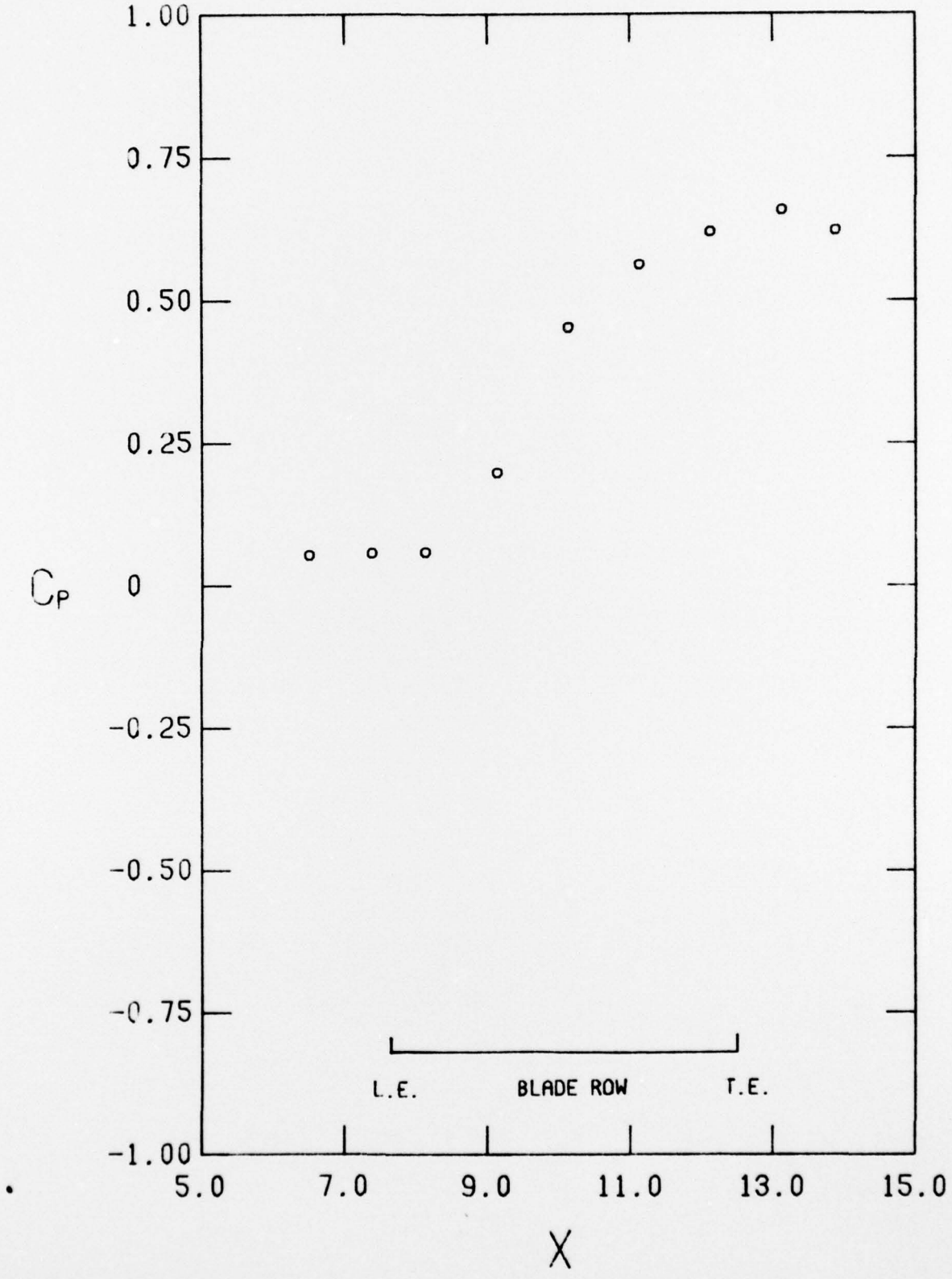

FIGURE 19. CONCLUDED
L. $C_X/U = 0.597$

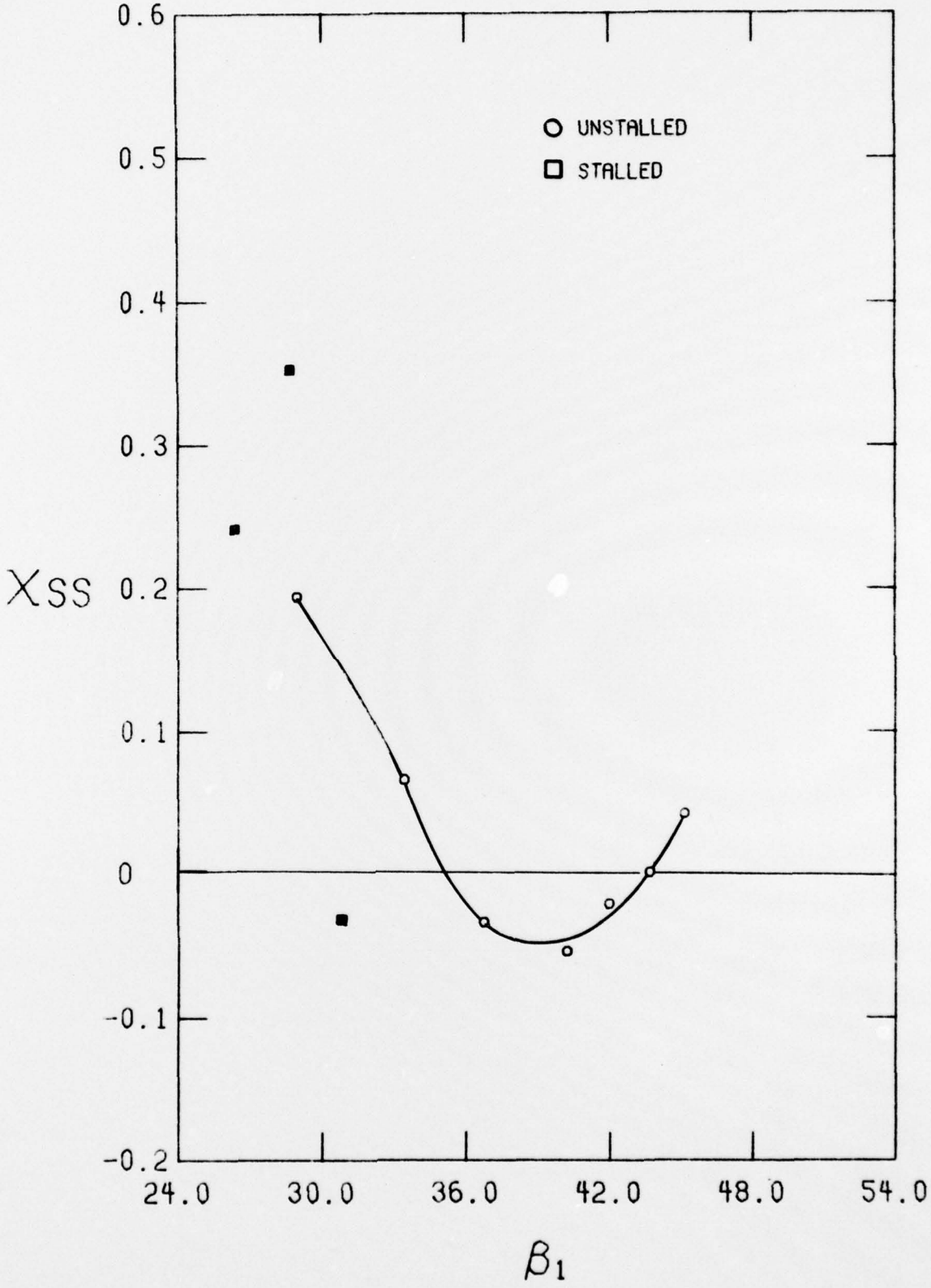

FIGURE 20. DISTORTED FLOW LOSS COEFFICIENT AS A FUNCTION OF INLET ANGLE

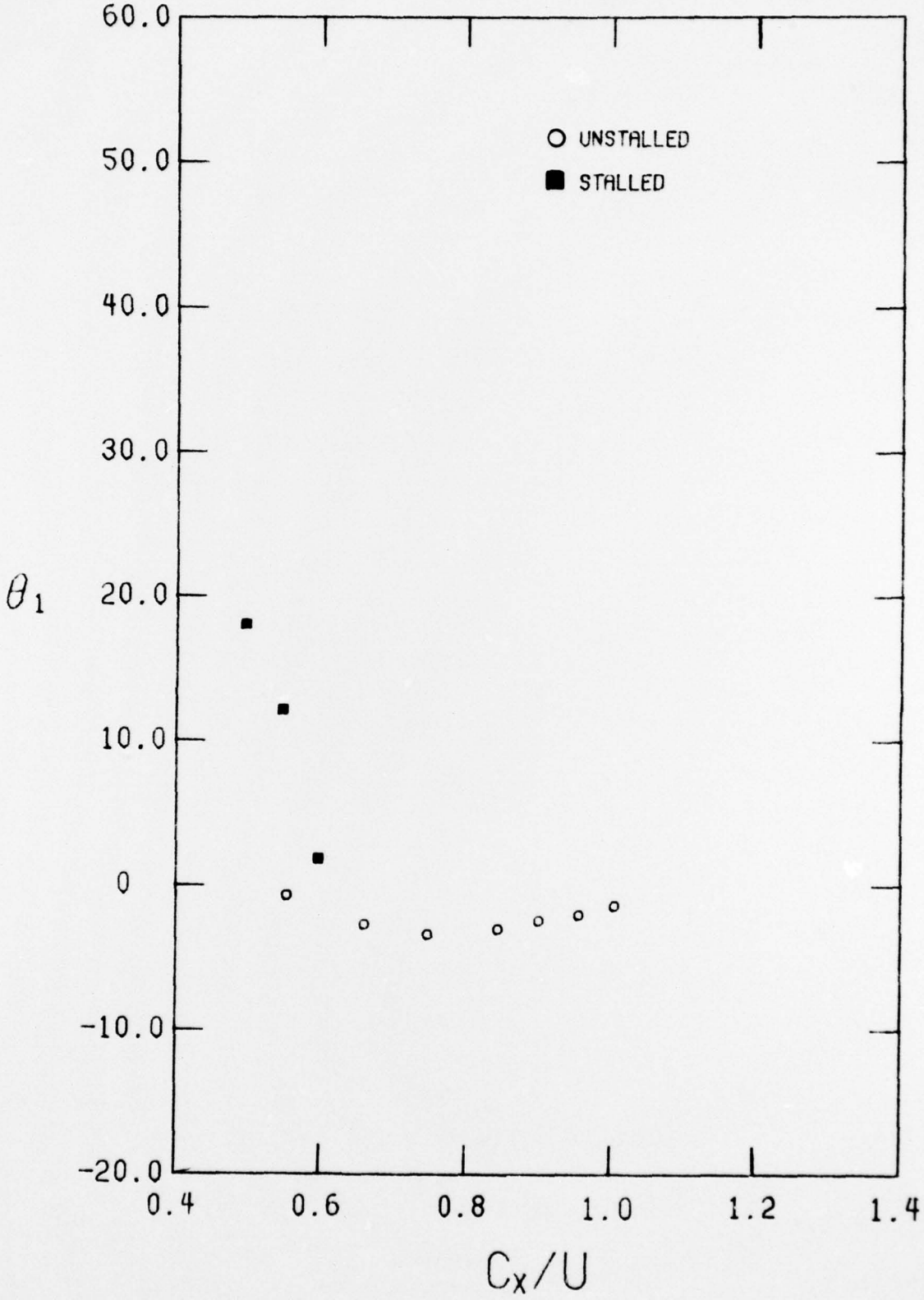

FIGURE 21. DISTORTED FLOW STATIONARY REFERENCE FRAME FLOW ANGLES

A. ROTOR ENTRANCE ANGLE

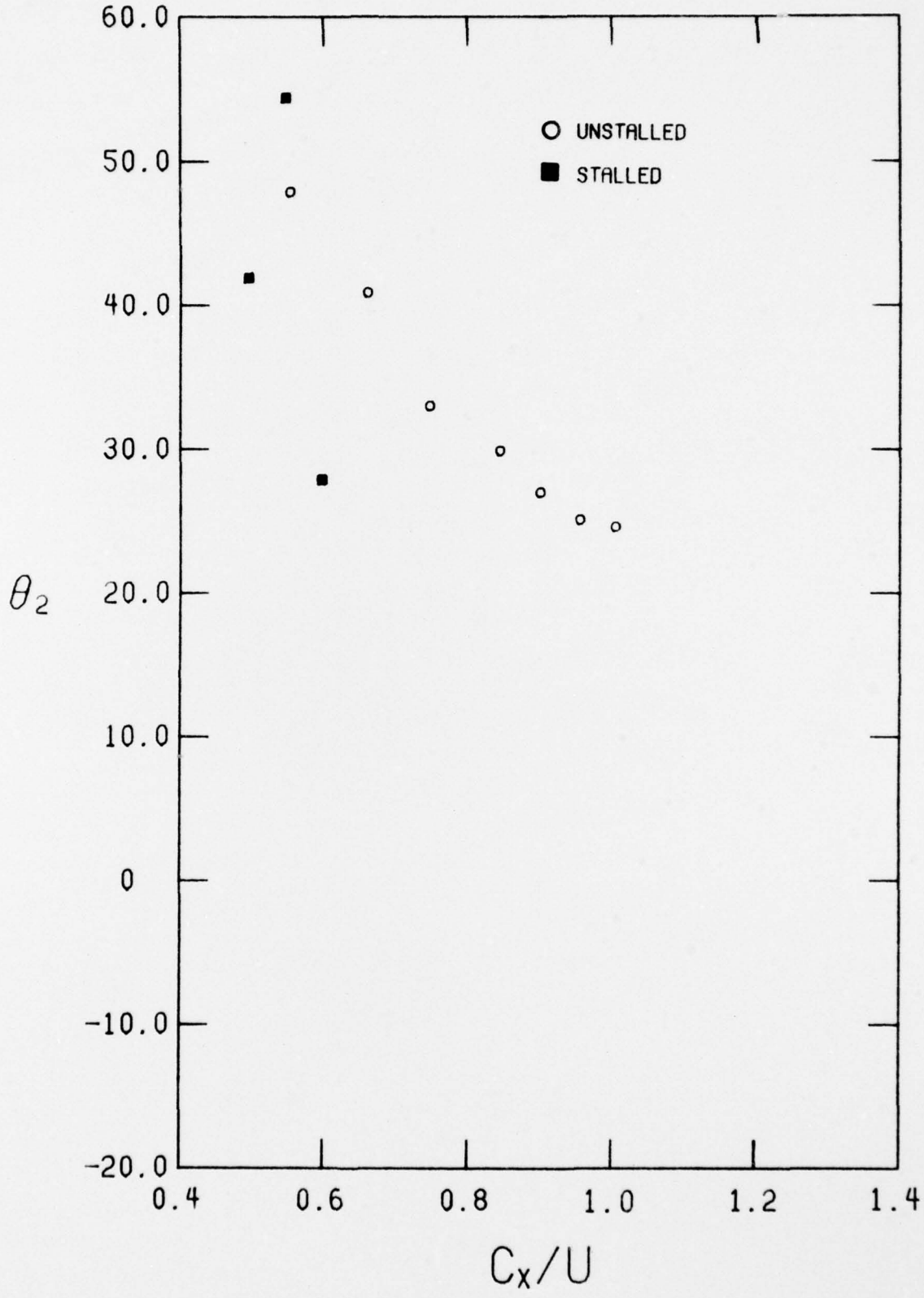

FIGURE 21. CONCLUDED
B. ROTOR EXIT ANGLE

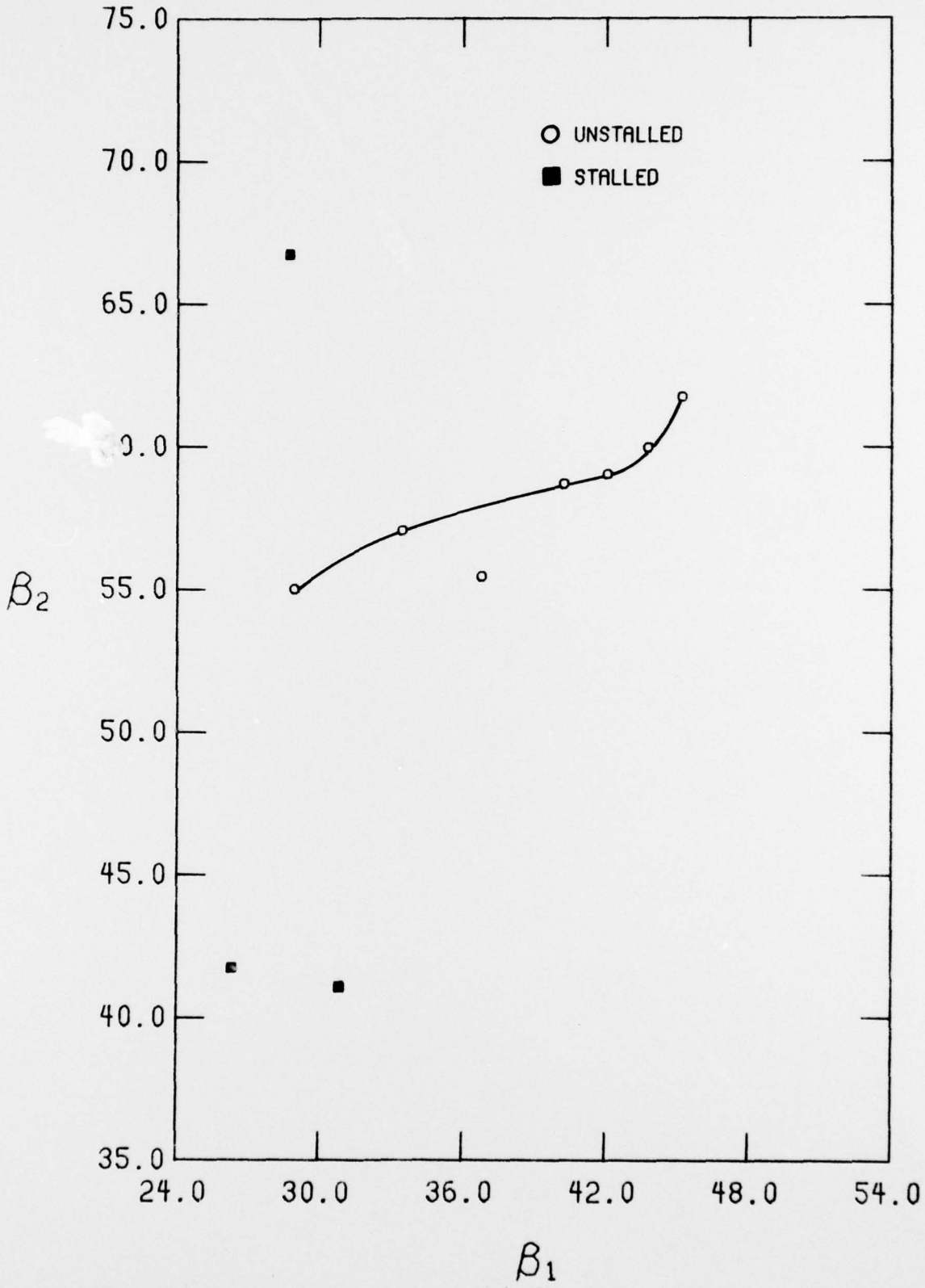

FIGURE 22. DISTORTED FLOW EXIT ANGLE AS A FUNCTION OF INLET ANGLE

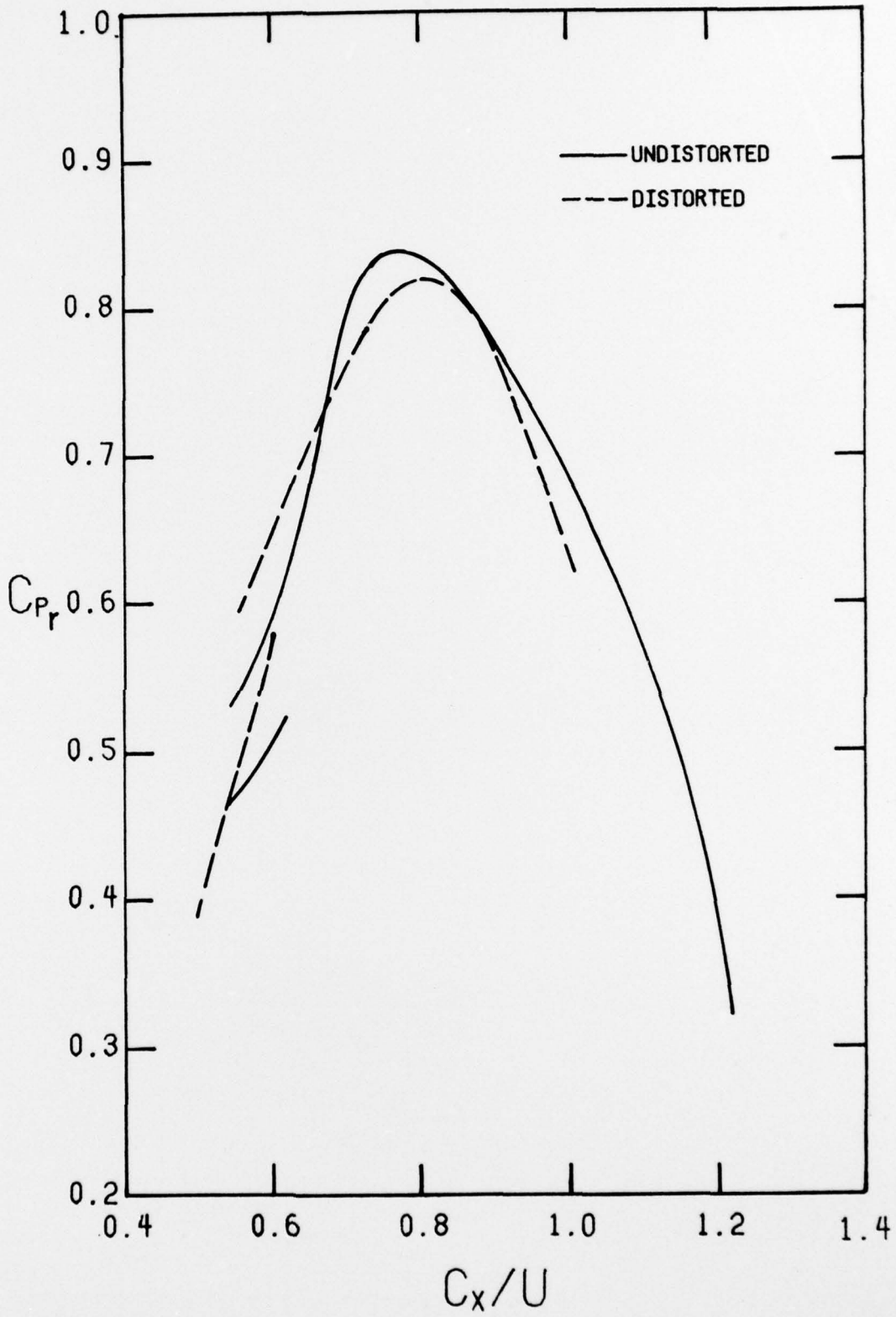

FIGURE 23. ROTOR PRESSURE RISE FOR UNDISTORTED AND DISTORTED FLOWS

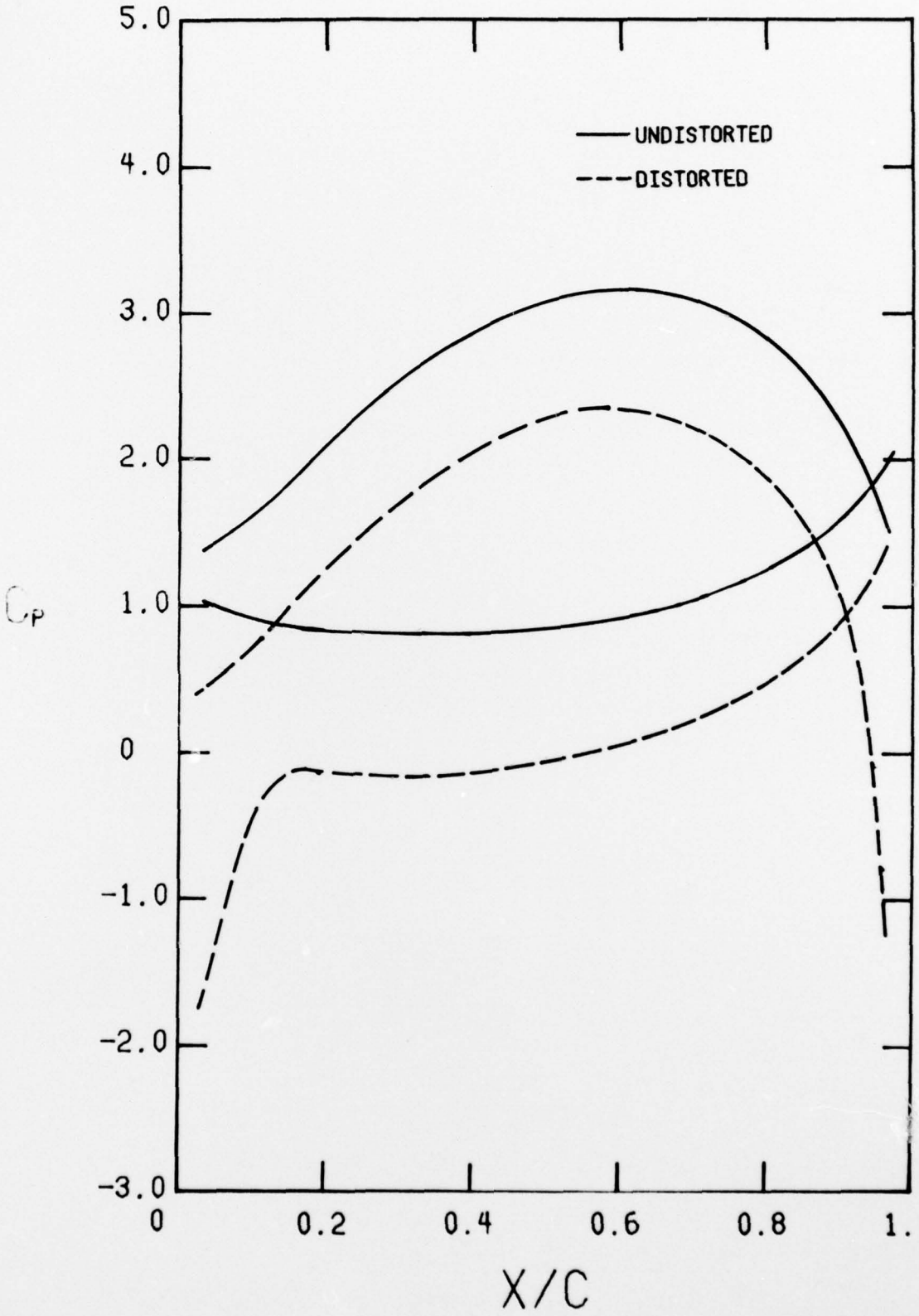

FIGURE 24. BLADE PRESSURE DISTRIBUTIONS FOR UNDISTORTED AND DISTORTED FLOWS
$C_X/U = 1.01$

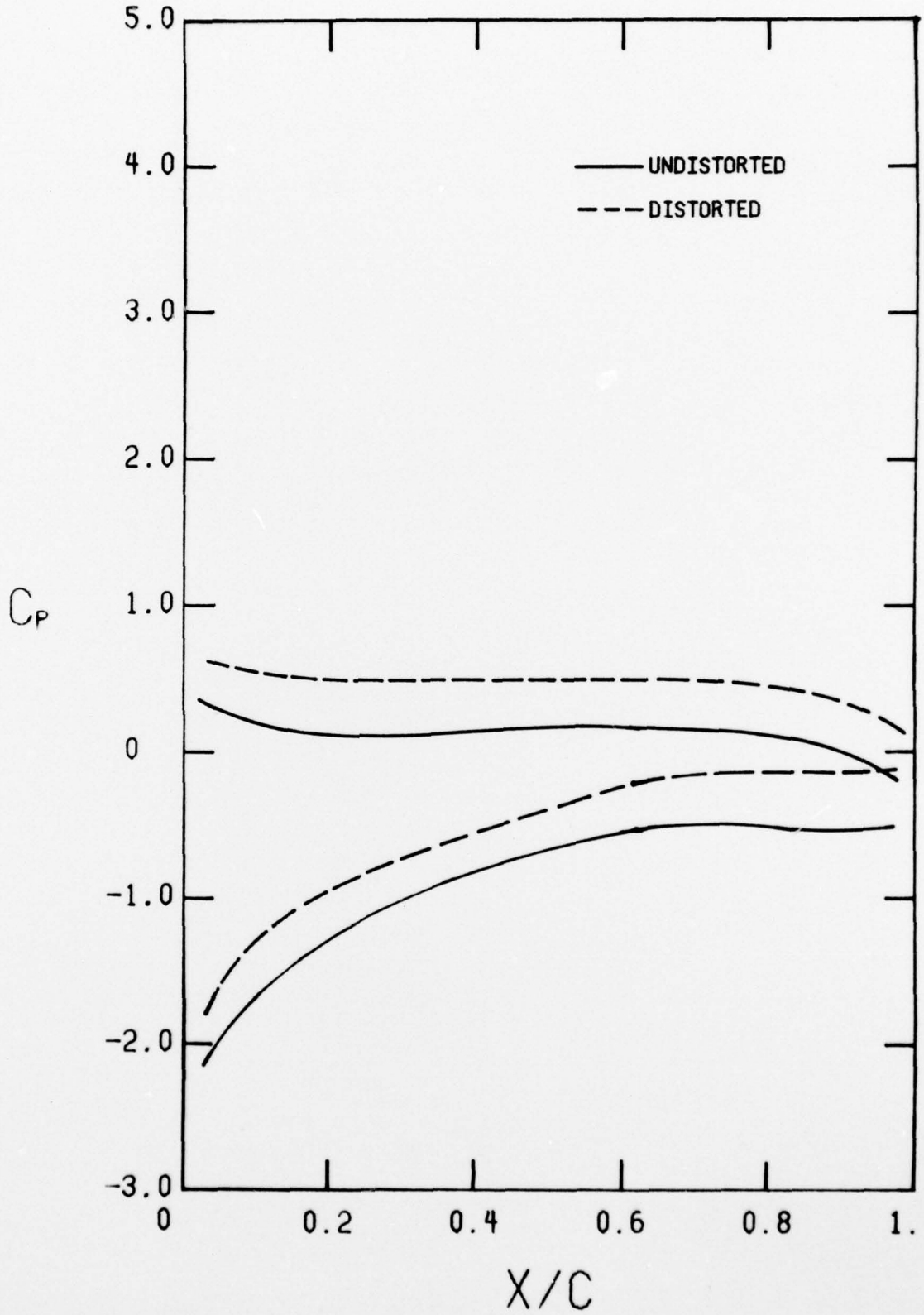

FIGURE 25. BLADE PRESSURE FOR UNDISTORTED AND DISTORTED FLOWS
$C_X/U = 0.55$

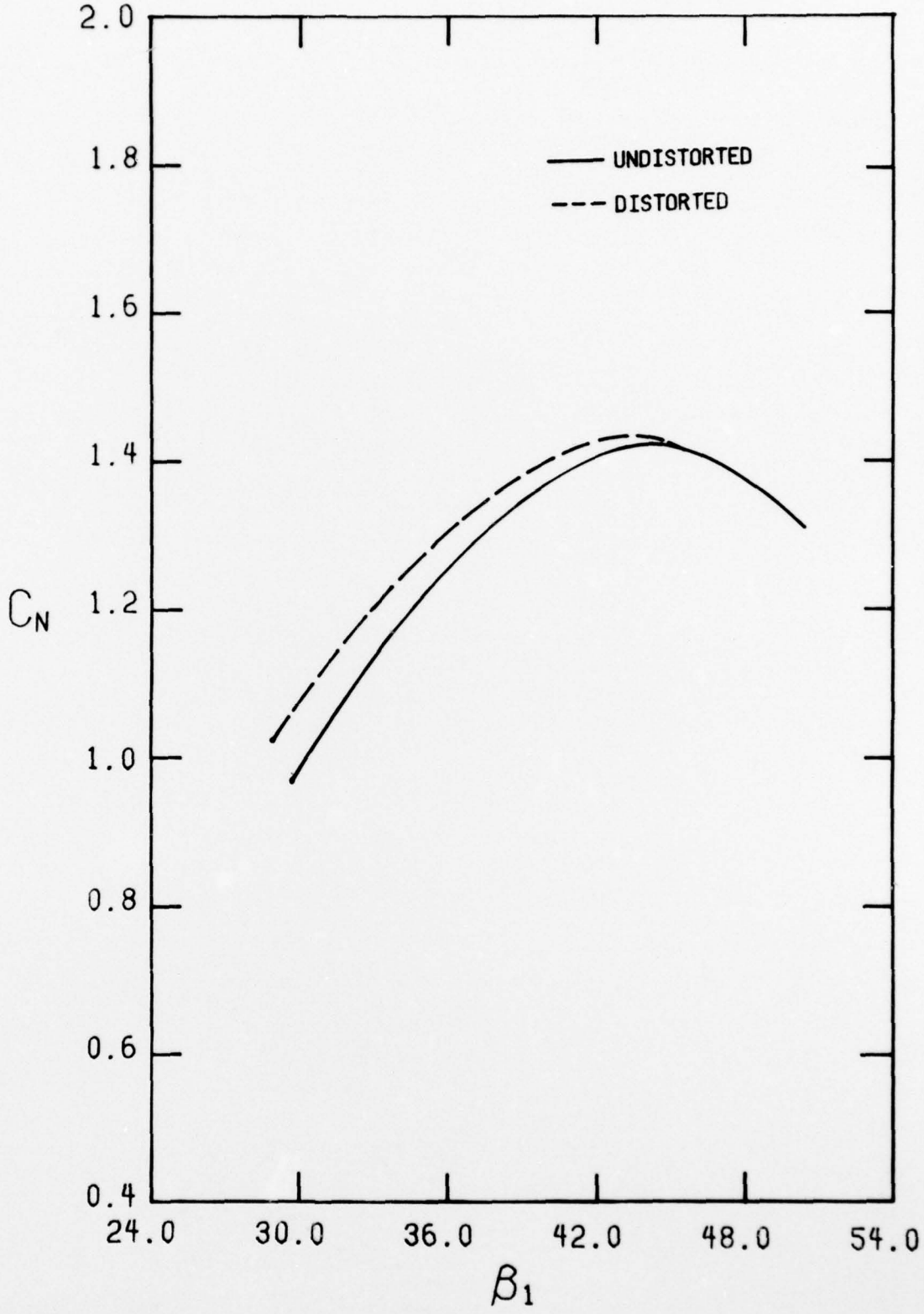

FIGURE 26. NORMAL FORCE COEFFICIENT FOR UNDISTORTED AND DISTORTED FLOWS

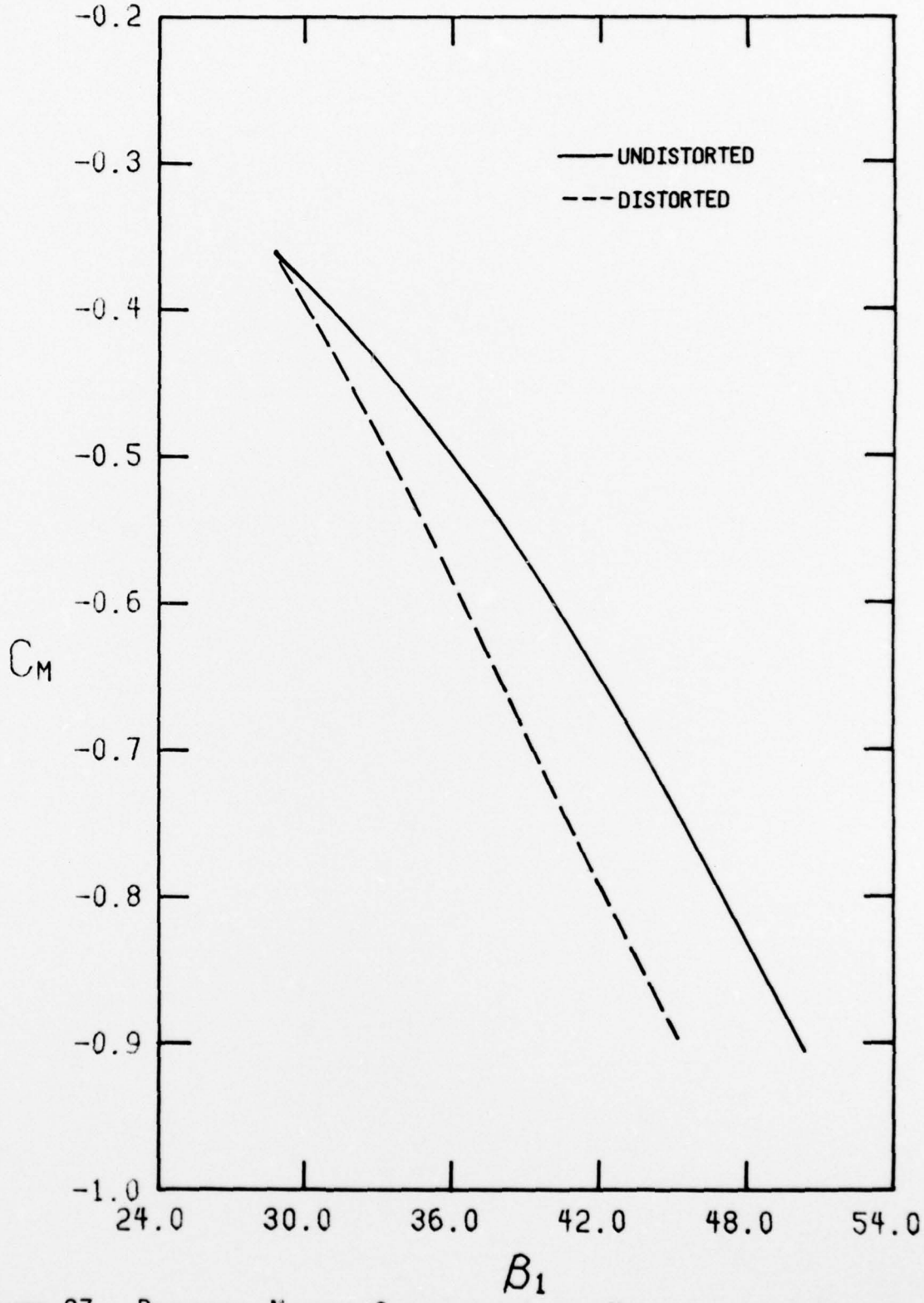

FIGURE 27. PITCHING MOMENT COEFFICIENT FOR UNDISTORTED AND DISTORTED FLOWS

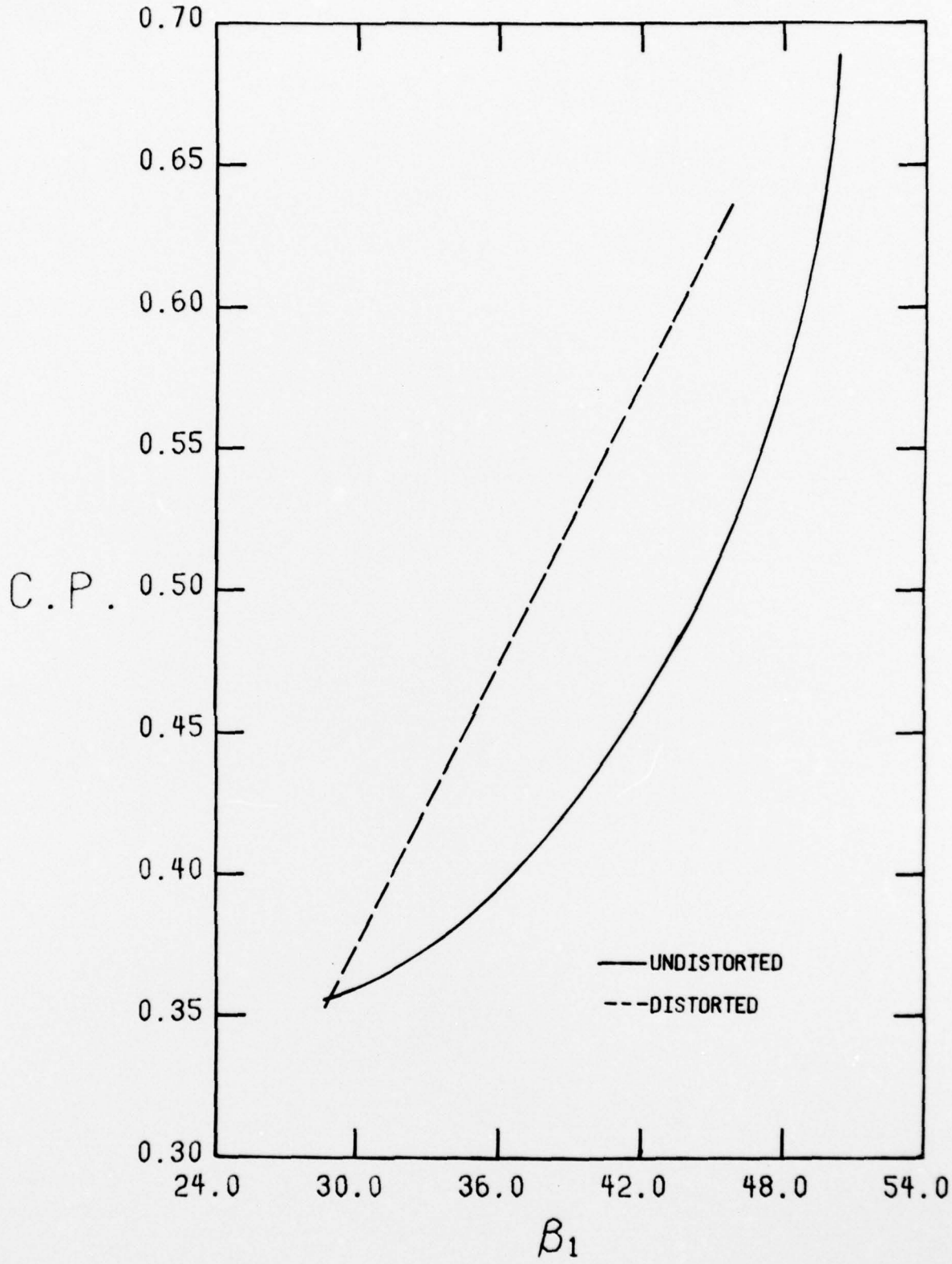

FIGURE 28. CENTER OF PRESSURE VARIATION FOR UNDISTORTED AND DISTORTED FLOWS

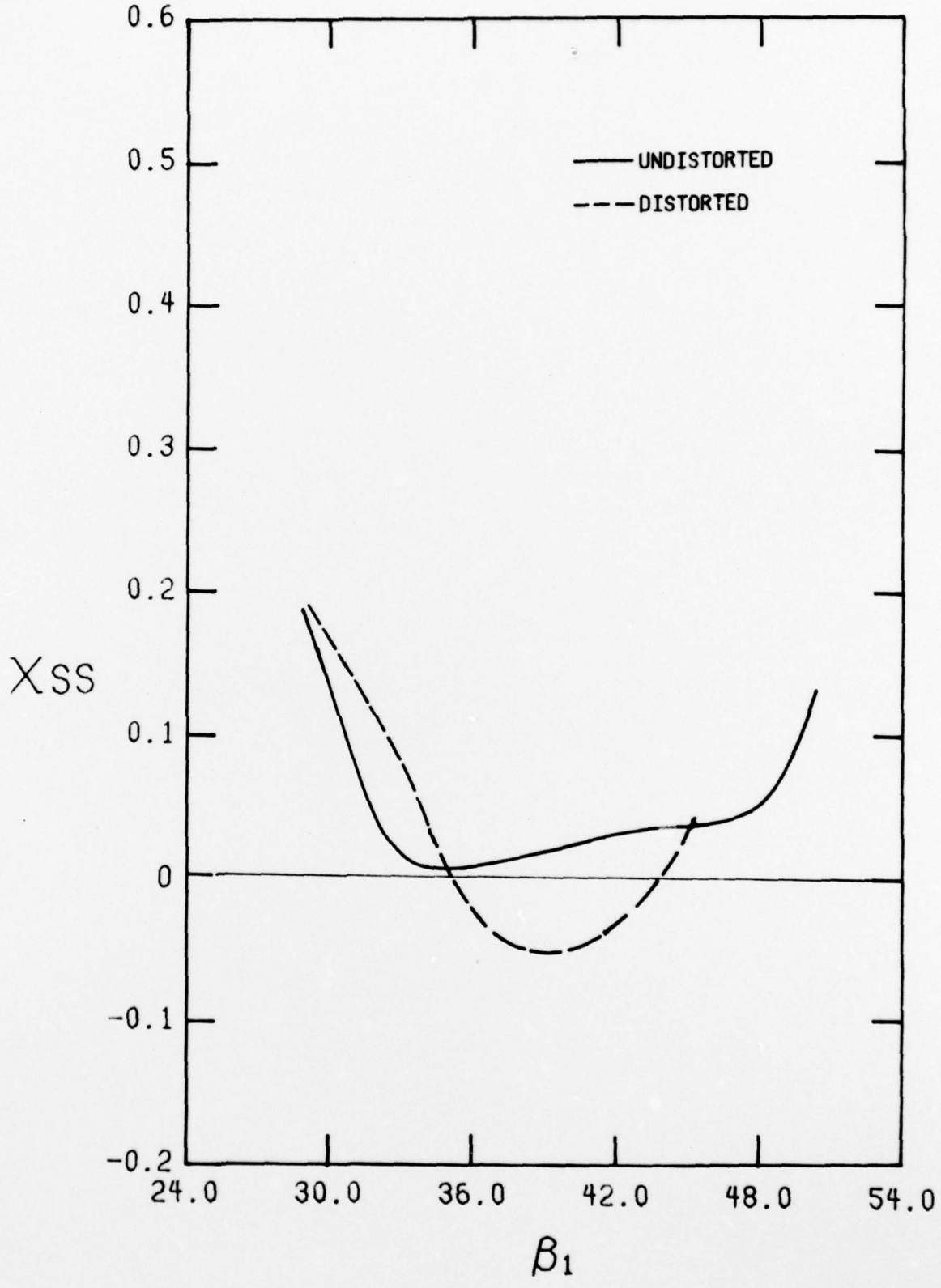

FIGURE 29. TOTAL PRESSURE LOSS CHARACTERISTIC FOR UNDISTORTED AND DISTORTED FLOWS

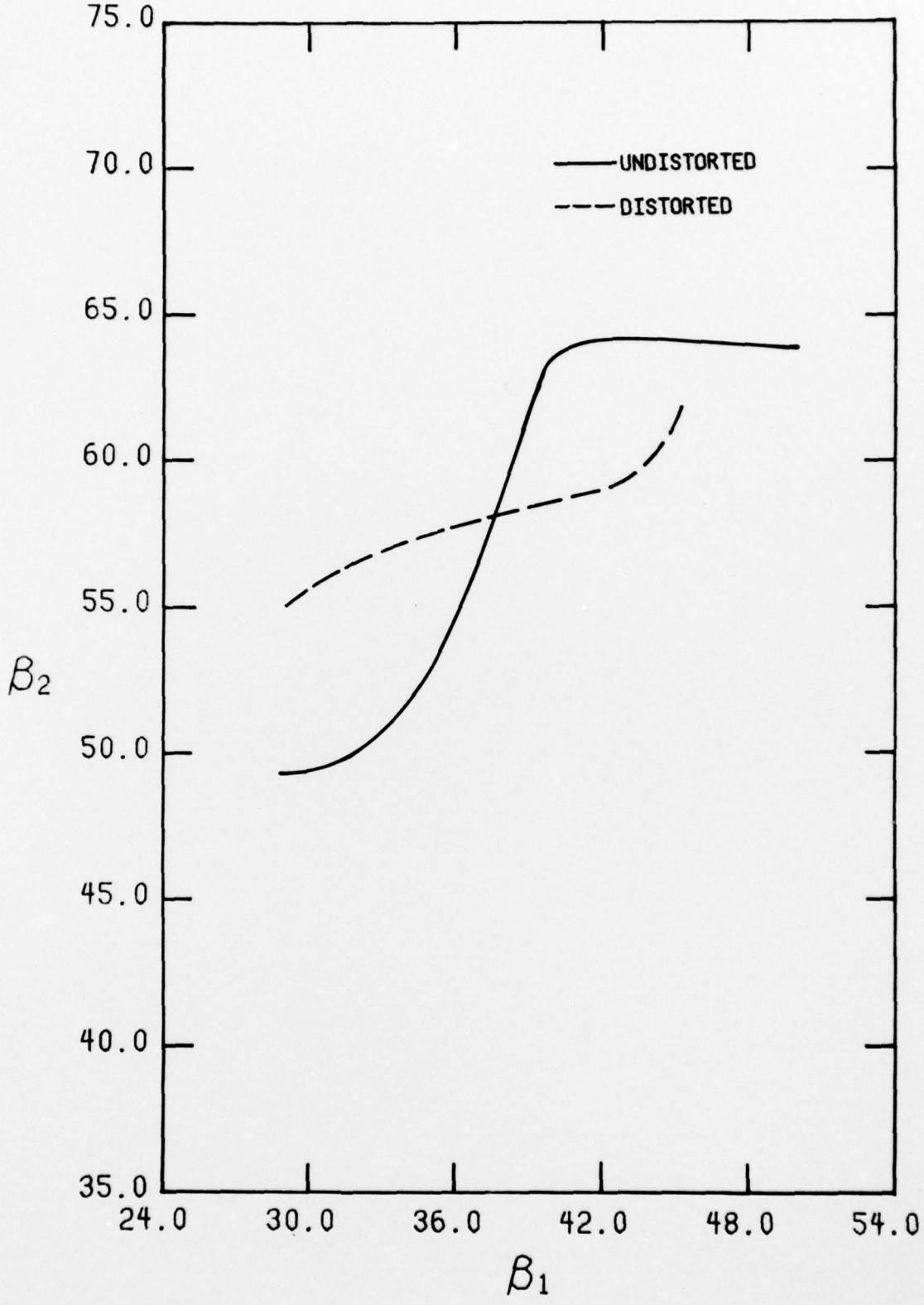

FIGURE 30. VARIATION OF EXIT FLOW ANGLE FOR UNDISTORTED AND DISTORTED FLOWS